EVOLUTION OF STATE AND SHAPE OF VISCOPLASTIC FORMATIONS

Zur Erlangung des akademischen Grades eines

DOKTOR-INGENIEURS

von der Fakultät für

Bauingenieur-, Geo- und Umweltwissenschaften
am Karlsruher Institut für Technologie (KIT)

genehmigte

DISSERTATION

von

Dipl.-Ing. Sascha Rübel

aus Karlsruhe

Tag der mündlichen Prüfung:	1. Juni 2012
Hauptreferent:	em. o.Prof. Dr.-Ing. Dr.h.c. G. Gudehus
Korreferent:	apl.Prof.Ing.habil. Dr.rer.nat. G. Borm

Karlsruhe 2012

Abstract

Gradual closure (a kind of creep) of wellbores in viscoplastic formations is a considerable challenge for the access of new hydrocarbon or geothermal reservoirs. Any leakage of the seal (cap rock) overlying a CO_2 storage reservoir has to be avoided for human safety and protection of the environment. Estimations of expected deformation rates of viscoplastic formations, due to artificially induced changes of the natural stress field, are key issues related to underground storage of CO_2 and the viability of boreholes. The objective of this thesis is to close the gap between the comprehension of the evolutions of state and shape of viscoplastic formations and practical requirements, and to better describe subcritical evolutions of viscoplastic formations.

Nearly pore-free solids composed of soft solid particles are called keroids (i.e. wax-like). Laboratory tests have been carried out with paraffin, hydrogel and various geomaterials. The observed properties agree essentially with the assumptions made for keroid materials. Keroids reveal markedly nonlinear viscous effects such as argotropy, creep and relaxation. Viscoplastic deformations are possible at low shortening rates up to a maximum value (i.e. critical shortening rate) which characterizes an upper bound of the ductile regime. Micropores can occur in the ductile regime in a minute fraction which increases spontaneously at the verge of ductility. With a critical shortening rate, which marks the transition from viscoplastic to clastic behavior, more micropores are induced than vanish in the same time. Shear localization has been observed with continued deformation with sufficiently high (i.e. critical) shortening rates. Much higher deformation rates result in axial splitting.

The material behavior observed in the tests for subcritical (stable) states is described with a physically based constitutive approach. Viscous effects in solids can be physically explained with thermally activated changes of pre-existing dislocations. The employed constitutive equation is based on this kind of rate process theory and provides a description of argotropic behavior, creep and relaxation. The chosen viscoplastic constitutive relation for keroids satisfies the requirements of objectivity. The range of validity is limited by upper bounds of deformation rates due to shear localization and cracking, which have been determined with laboratory tests. Numerical back-calculations of own laboratory tests with the chosen constitutive equation show a good agreement with the results of the laboratory tests within the range of validity.

Various numerical simulations of boundary value problems have been carried out with the employed constitutive relation. A numerical simulation of an infinite slope leads asymptotically to stationary creep. The results are in good agreement with available analytical solutions.

Borehole convergence model tests have been carried out with a novel testing device. The results of the tests reveal the influence of deviatoric stress on the evolution of deformation of a borehole. Simulations of the laboratory tests have been carried out with an axisymmetric model. The results of the numerical simulations are in good agreement with the laboratory tests. The numerical model could thus be validated with the laboratory tests. The influence of a casings and linings on convergence has been studied with a plane strain model of a horizontal cross-section.

Cap rocks above a salt pillow have been modeled with axial symmetry. Based on exemplary data, evolutions of deformation rates due to a CO_2 injection have been simulated with estimated parameters and simplified boundary conditions. The results show that deformation rates in a clay smear can be kept low with moderate pressure changes. Stopping an injection at a constant reservoir pressure leads to rapidly decreasing deformation rates of a clay smear. Self-healing of the clay smear due to thermally activated stress redistribution could be achieved with a reduction of the reservoir pressure. Thus, the system becomes safer. Simulations with the employed numerical model may serve as a physically based approach for assessing CO_2 injections.

Preface

Gradual closure (a kind of creep) of boreholes in viscoplastic formations is still a challenge for the access of hydrocarbon reservoirs and geothermal energy. The evolution of state of a viscoplastic natural seal is eminent for a safe storage of CO_2. It was a challenge and honor for me to contribute to the scientific improvement in these topics.

The presented PhD thesis was developed during my tenure as a scientific associate at the Institute of Soil Mechanics and Rock Mechanics at the Karlsruhe Institute of Technology (KIT), former University of Karlsruhe (TH). My research work during this time was supported by the German Federal Ministry of Education and Research (BMBF) within the research program ”GEOTECHNOLOGIEN”, joint project ”COSMOS”, subproject 3 ”Cap rock integrity” (No. BMBF 03G0630C) and within the integrated European project ”CO2SINK In-situ R&D Laboratory for Capture and Storage of CO_2” (No. SES6-CT-2004-502599, EU FP6) and by the German Federal Ministry for the Environment, Nature Conservation and Nuclear Safety (BMU) within the project ”Reduzierung der geologisch bedingten bohrtechnischen Risiken - Bohrlochstabilität in tertiären Tonsteinfolgen im Oberrheingraben als Hindernis für die Erschließung geothermischer Reservoire” (No. 0327599). This is greatfully acknowledged.

It was a challenge to finish this thesis simultaneously with my profession as a geotechnical engineer at Bilfinger Berger in Wiesbaden in addition to my family and my profession.

I express my special gratitude to my doctoral supervisor and teacher Prof. G. Gudehus for the valuable scientific discussions and constructive impulses. His energy to inspire others scientifically accompanied my entire work. His intense backing motivated me continuously to proceed and finish successfully my thesis.

I like to thank Prof. G. Borm for being the second examiner and for bridging among different geo-communities. With his engagement it was possible to carry out parts of my scientific investigations within the BMBF-project COSMOS. By means of his support, core sample material was available from the deep boreholes at Ketzin from the EU-project CO2SINK. I like to thank the further members of my examination board, Dr. D. Eckhardt, Prof. F. Schilling and Prof. K. Schweizerhof, for scientific consulting and support. Furthermore, I thank Prof. K. Schweizerhof for taking the chairmanship of this board.

I like to thank all my former colleagues at the IBF for the cooperative teamwork. I like to thank especially Karl Balthasar and Daniel Kuketz, without their hands-on support it would have been difficult to realize the laboratory tests with the achieved precision. Many friendships with colleagues have grown from scientific contacts during the times at the IBF and last until today.

I like to thank my student assistants and my master thesis students, in particular Jeannine Eisenmann and Hendrik Suttkus, for the reliable help with the performances and evaluations of laboratory tests.
I like to thank my colleagues at Bilfinger Berger for their consideration and encouragement to complete my thesis simultaneously to professional and family needs.

I like to thank in particular my wife Katja. She supported my intention during all ups and downs related with this thesis. She gave me always new power in difficult situations. With her skills to organize our family she kept my back free, whenever it was necessary, so I was able to focus on my work. With her great character she cared for a lucky family even in times with high pressure of work.
My daughters Laila, Janina and Enya were an important balance for me. With their carelessness and joie-de-vivre they helped me to see a lot of things from different points of view. They remembered me continuously that there are so many more issues which require my full concentration.

Last but not least I like to thank my parents Margot and Jürgen. They founded my scientific and technical interest and opened this gate for me. As well as my parents-in-law, they stood always behind me and helped us with the care for our three daughters in an irreplaceable manner.

Sascha Rübel

Taunusstein-Wingsbach, im Juni 2012

Vorwort

Verformungen von Bohrlöchern in viskoplastischen Formationen sind nach wie vor ein Hindernis für die Erschließung von Kohlenwasserstoffen und geothermischer Energie. Für die Sicherheit von CO_2-Speichern hinsichtlich ihrer Dichtheit hat die Entwicklung des Zustandes von viskoplastischem Material eine wesentliche Bedeutung. Es war für mich eine Herausforderung und Auszeichnung zum wissenschaftlichen Fortschritt auf diesen Gebieten beitragen zu können.
Die vorliegende Arbeit entstand zum Teil während meiner Zeit als wissenschaftlicher Angestellter am Institut für Bodenmechanik und Felsmechanik des Karlsruher Instituts für Technologie (KIT), ehem. Universität Karlsruhe (TH). Meine Forschungstätigkeit wurde während dieser Zeit durch das Bundesministerium für Bildung und Forschung (BMBF) im Rahmen des Forschungsprogrammes "GEOTECHNOLOGIEN", Verbundprojekt "COSMOS", Teilprojekt 3 "Cap rock integrity" (Förderkennzeichen
BMBF 03G0630C) und im Rahmen des integrierten EU-Projektes "CO2SINK In-situ R&D Laboratory for Capture and Storage of CO2" (No. SES6-CT-2004-502599, EU FP6) und durch das Bundesministerium für Umwelt, Naturschutz und Reaktorsicherheit im Rahmen des Projektes "Reduzierung der geologisch bedingten bohrtechnischen Risiken - Bohrlochstabilität in tertiären Tonsteinfolgen im Oberrheingraben als Hindernis für die Erschließung geothermischer Reservoire" (Förderkennzeichen 0327599) gefördert. Dafür sei hier ausdrücklich gedankt.
Die anschließende Fertigstellung dieser Arbeit während meiner Zeit als Projektingenieur bei Bilfinger Berger in Wiesbaden neben Familie und Beruf war eine große Herausforderung.

Besonderer Dank gilt meinem Doktorvater und Lehrer Prof. G. Gudehus für die wertvollen wissenschaftlichen Diskussionen und konstruktive Anregungen. Seine Fähigkeit wissenschaftlich zu begeistern hat mich während der gesamten Arbeit begleitet. Sein starker Rückhalt hat mich immer wieder motiviert die Arbeit voran und zu einem gelungenen Abschluss zu bringen.
Bei Prof. G. Borm bedanke ich mich für die Übernahme des Korreferats und für die Brückenschläge zwischen verschiedenen Geo-Communities. Durch sein Engagement war es möglich einen Teil meiner wissenschaftlichen Untersuchungen im Rahmen des BMBF-Verbundprojektes COSMOS durchzuführen. Seiner Unterstützung ist auch die Bereitstellung von Kernprobenmaterial aus den Tiefbohrungen in Ketzin aus dem EU-Projekt CO2SINK zu verdanken.
Den weiteren Mitgliedern meiner Promotionskommission, Dr. D. Eckhardt, Prof. F. Schilling und Prof. K. Schweizerhof, danke ich für ihre wissenschaftliche Beratung und

Unterstützung. Darüber hinaus danke ich Prof. K. Schweizerhof für die Übernahme des Vorsitzes der Kommission.

Bei allen Mitarbeiterinnen und Mitarbeitern des IBF bedanke ich mich für die gute Zusammenarbeit. Insbesondere Karl Balthasar und dem leider verstorbenen Daniel Kuketz danke ich für die tatkräftige Unterstützung, ohne welche die Versuche mit der hier erreichten Präzision schwer durchzuführen gewesen wären. Aus den fachlichen Kontakten dieser Zeit sind mit einigen Kollegen gute Freundschaften entstanden, die bis heute bestehen.
Meinen wissenschaftlichen Hilfskräften und Diplomanden, insbesondere Jeannine Eisenmann und Hendrik Suttkus, danke ich für die zuverlässige Unterstützung bei der Durchführung und Auswertung von Versuchen.
Meinen Kollegen bei Bilfinger Berger danke ich für ihre Rücksichtnahme und die Motivierung meine Arbeit trotz Beruf und Familie zum Abschluss zu bringen.

Ich danke in besonderem Maß meiner Frau Katja. Mit ihrer Geduld, ihrem Verständnis und ihrer Rücksichtnahme hat sie mein Vorhaben während allen Höhen und Tiefen im Verlauf dieser Arbeit begleitet und unterstützt. Sie hat mir in schwierigen Situationen immer wieder neue Kraft gegeben. Durch ihr Organisationstalent hat sie mir in unserem Familienalltag immer wenn es nötig war den Rücken freigehalten, so dass ich mich auf meine Arbeit konzentrieren konnte. Mit ihrem großartigen Charakter hat sie dafür gesorgt, dass ich trotz hoher Arbeitsbelastung eine glückliche Familie hatte.
Meine Töchter Laila, Janina und Enya sorgten stets für einen wichtigen Ausgleich. Sie halfen mir mit ihrer Sorglosigkeit und Lebensfreude vieles aus einem anderen Blickwinkel zu betrachten. Dabei haben sie mich regelmäßig daran erinnert, dass es noch weitere Aufgaben gibt, die meine volle Aufmerksamkeit erfordern.

Schließlich, aber nicht zuletzt danke ich meinen Eltern Margot und Jürgen. Sie haben durch ihr Vorbild den Grundstein für mein wissenschaftliches und technisches Interesse gelegt und mir diesen Weg geöffnet. Wie auch meine Schwiegereltern standen sie immer hinter mir und haben uns mit der Unterstützung bei der Betreuung unserer drei Töchter unersetzliche Hilfe geleistet.

Sascha Rübel

Taunusstein-Wingsbach, im Juni 2012

To my family

Katja, Laila, Janina and Enya

Contents

Chapter 1

Introduction

New hydrocarbon reservoirs are discovered in deep formations, but their access with boreholes requires high efforts and costs. Gradual caving of wellbores is a considerable challenge for the access to new reservoirs. Problems observed with drilling indicate that sensitive formations consist of rock which shows a markedly viscoplastic behavior. It is common practice to drill such sensitive formations with the operating experience of drilling companies from hydrocarbon industry. Most of these challenging well sections are drilled in formations with clay minerals. Thus, it appears that the behavior of claystone in actual drilling practice is not sufficiently understood [18].
In particular, the gradual closure of wellbores (a kind of creep) is one of the brake blocks for research and for an exploitation of geothermal energy. The access to geothermal reservoirs requires also deep boreholes in crucial formations, e.g. claystones and siltstones, which exhibit viscoplastic behavior for typical in-situ stresses and temperatures. A deeper comprehension would therefore ease the access to geothermal reservoirs with capable risk.

The development of strategies for sustainable and safe technologies for an efficient reduction of emissions of greenhouse gas to the atmosphere is one of the major challenges for the future of mankind. Geological CO_2 storage in saline aquifers is one of the promising technologies for such a reduction, at least for an intermediate time period until other technologies will be available on a commercial scale. Sufficiently high deformation rates due to changes of pore pressure in a reservoir can lead to reactivations of shear bands in clay smears in a cap rock, which imply potential leakage paths. Thus, the evaluation of expected deformation rates during and after an injection is a key issue for a safe underground storage of CO_2.

There is thus a need of estimations of deformation rates of viscoplastic formations due to technically induced changes of stress fields. Nonlinear viscoplastic behavior of solids such as argotropy, creep and relaxation has been observed with a variety of materials. In order to quantify nonlinearly viscous effects, a variety of tests and constitutive approaches have been made.

Norton [2] performed tensile creep tests at constant loads and temperatures with bars of steel. From the results of his tests, which indicated a non-linear relation between stresses and rates of deformations, Norton suggested a one-dimensional relationship which, however, is not unit-invariant and not directly applicable to two- or three-dimensional problems.

Prandtl [1] explained the nonlinearly viscous behavior with thermal activation. When analyzing tensile tests with rods of cast iron, Prandtl found that deformations due to the applied stresses include a non-reversible part of which the magnitude reveals a significant time-dependence. He proposed an empirical nonlinear relationship between changes of stretching velocities and changes of stresses. Prandtl explained time-dependent deformations by means of thermal oscillations in a solid body, and noticed that the probability of dislocations of solid particles increases with an increasing temperature. He derived an exponential relationship between the rate of displacements and an activation energy, which is a precursor of the rate process theory [5].

Based on condensed matter physics, Persson [8] proposed a theory for the viscoplastic deformation of glassy solids. This theory can also be applied to polymers as e.g. paraffin, plastics or rubber. Persson derived Prandl's equation with an approach which regards dislocation units as so-called nano-sized stress-blocks. Persson's approach specifies the dislocation unit for solids and provides realistic activation energies and bounds for a validity-range of deformation rates.

Leinenkugel [3] investigated the shearing resistance of clayey soils and explained his results with a kind of rate process theory. Leinenkugel found Prandtls approach to be in good agreement with his experimental results. With this approach it is possible to estimate velocities and resulting forces for a variety of geotechnical applications, such as the velocity distribution of creeping slopes or the lateral flow pressure against piles. Subsequent advances in soil mechanics lead to physically based and practically applicable approaches, which enable realistic estimations of deformations and deformation rates for soils [13].

The objective of this thesis is to bridge the gap between the comprehension of the evolutions of state and shape of viscoplastic formations and practical requirements, and to better describe *subcritical evolutions* of viscoplastic formations.

With numerical simulations of scenarios, which may be relevant for human and environmental safety, it should be evaluated whether a viscoplastic formation remains in a stable range.

Chapter 2 aims to analyze viscoplastic material behavior with suitable laboratory tests.

It deals with the investigation of the behavior of samples available in the laboratory which are composed of rather soft solid particles and a minute fraction of micropores. Starting from paraffin, such materials are called *keroids* (wax-like). Due to extensive deformations, the material in a clay smear is remolded. Thus, its behavior can be investigated with reconstituted samples. The stress-deformation behavior at variable deformation rates is studied with laboratory tests with controlled axial shortening velocity. Such tests are found to be suitable to study the material behavior within a wide range of deformation rates. Upper bounds of them are related with shear banding and cracking, such *critical phenomena* indicate the verge of stability.

Chapter 3 aims at choosing and testing a suitable constitutive relation to describe the observed viscoplastic material behavior in the stable range up to steady states. Some available results and constitutive approaches are presented. Numerical simulations of element tests and a complete formulation of boundary value problems require constitutive relations which satisfy requirements of objectivity. The chosen tensorial formulation of a viscoplastic constitutive relation, which is suitable to describe the nonlinear viscoplastic behavior in the ductile (i.e. stable) regime within a wide range of deformation rates, is presented in Chapter 3. It is compatible with the rate process theory, thus the influence of temperature on the viscoplastic behavior can be taken into account. Numerical simulations of laboratory tests were carried out with the chosen constitutive relation. The results of the laboratory tests are compared with those of numerical simulations. Limits of applicability of the constitutive relation with numerical calculations are outlined.

Chapter 4 aims to validate the chosen numerical model. One-dimensional boundary problems with viscoplastic formations are analyzed with respect to the evolution of velocity and stress. An analytical solution for the stationary field of velocity and stress of an infinite slope is presented. Results of numerical simulations of this problem are compared with an analytical solution. Numerical simulations are presented which show that an initially not radially symmetric stress field tends to a radially symmetric field if the shape of a converging circular borehole is kept radially symmetric. Stress and velocity fields are attained asymptotically by the chosen systems. If initial states of stress and velocity fields are assumed as such distinguished states which are attained asymptotically, then subsequent states can be independent of the previous evolution.

Chapter 5 aims to analyze the convergence of axisymmetric boreholes in viscous formations. The convergence of a vertical borehole is studied with laboratory tests with novel testing devices and with a suitable model material. Convergence tests show the evolution of the deformation of a borehole and exhibit the influence of far-field deviatoric stress on the convergence velocity. Results of numerical simulations of the laboratory tests are compared with the results of the laboratory tests in order to validate the numerical model.

The influence of the borehole bottom on convergence velocity is investigated with an axisymmetric model. The influence of casings or linings on convergence is studied with a plane strain model of a horizontal cross section. The results are described and explained.

Chapter 6 aims to develop a model which enables estimations of deformation rates in a viscoplastic formation in a subcritical state that seals a CO_2 reservoir. Based on exemplary data, evolutions of deformation rates due to CO_2 injection are calculated with an axisymmetric model. Thus it could be principally judged whether the viscoplastic material of a sealing formation remains in a subcritical (ductile) range during and after an injection.

A summary and an outlook are given in Chapter 7.

Chapter 2

Material behavior

2.1 Objective and overview

Viscoplastic material behavior can be observed with a variety of solids, even with those where one would not expect it from everyday experience. This chapter deals with the investigation of the viscoplastic material behavior of solids which are composed of rather soft solid particles and bound fluid with a fraction of micropores. Laboratory tests at constant temperature have been carried out with various materials. Tests with controlled axial shortening velocity have been found to be suitable to study the material behavior within a wide range of deformation rates.

Paraffin is a representative material for nearly pore-free solids with soft particles. Viscous effects, i.e. *argotropy* (rate-dependence, from Greek: argos = fast), *creep* and *relaxation*, were studied with paraffin. They resemble those of geomaterials like ice or rock salt with slow deformations. Thus, paraffin is a suitable material to demonstrate qualitatively the material behavior of a class of geomaterials which are named *keroids*, i.e. wax-like.

Hydrogel is a material of this class and is suitable for model tests. Some tests have been carried out with a hydrogel as this material is transparent and exhibits marked viscoplastic properties. The alkane particles are soft and viscoplastic deformation is mainly due to thermal activation at room temperature. Gas pores due to cavitation or shear localization are not induced except for high deformation rates, otherwise the material remains transparent. Steady states or fracture have not been reached with compression tests. Thus, the hydrogel that was used for the tests remained in a subcritical state (ductile regime) with the employed deformation rates at room temperature. The material properties and laboratory tests with hydrogel are described in detail in Chap.5.

Reconstituted samples are a suitable substitute for the material of clay smears in a cap rock since clay smears have been naturally remolded by extensive deformations. Further laboratory tests have been carried out with reconstituted samples of clay minerals, reconstituted clayey rock samples and drilled core samples of claystone. These materials are ductile within the tested subcritical range. Critical states with formation of pores, shear bands and brittle fracture were reached with laboratory tests with sufficiently high deformation rates.

2.2 Determination of elastic properties

The results of laboratory tests which are presented later in this chapter indicate that the mechanical properties of nearly pore-free solids with soft particles exhibit both elasticity and non-linear viscosity. A viscoplastic constitutive law, which defines a linear elastic and a (thermally activated) non-linear viscous stress-deformation relationship, will be presented in Chap. 3. The version which uses tensors can be applied to a numerical stress-displacement analysis for nearly pore-free solids which are in a subcritical (ductile) regime.

Slight knocks on a measuring cup with a hydrogel initiate audible vibrations without visible remaining deformation of the material. A groove that is scratched into the gel surface, in order to carry out a liquid limit test with a standard device, remains open even after a hundred bounces of the cup. Thus, it appears that elastic material properties dominate the material behavior of nearly pore-free solids with high deformation rates and small amplitudes [6].

Linearity is assumed for the elastic part of the constitutive law. Assuming isotropy requires the determination of two elasticity constants (E and ν). Prandtl [1] noticed that the reversible part (elastic, time-independent) and the non-reversible part (viscoplastic, time-dependent) of the constitutive law cannot be separated in experiments. Thus, it is not possible to determine exactly the elasticity constants with laboratory tests. However, viscous effects become negligible with sufficiently high deformation rates. Thus, laboratory tests with high deformation rates and very small deformations enable an estimation of elasticity constants. Therefore, the material constants E and ν (Chap. 3) have been determined by measurement of propagation of ultrasonic waves. Youngs moduli that are determined with this method can be approximately more than one factor of ten higher than moduli that are determined with rock samples in an uniaxial compression test with slower deformation rates and larger deformations. Viscoplastic stress-relaxations evolve faster with higher Youngs moduli.

Longitudinal P-waves (compression waves) and transversal S-waves (shear waves) are induced with separate transmitters at the upper circular surface of a cylindrical sample (Fig. 2.1). A corresponding receiver, which is attached to the opposite (lower) circular surface, records the arrival of the transmitted sine-shape signals. Transmitter and receiver are connected to an oscilloscope (Fig. 2.1). Thus, it is possible to measure the times required for transmitting the signals of P-waves (t_L) and of S-waves (t_T). The distance l between transmitter and receiver is known as the height of the cylindrical sample. Thus, the wave propagation velocity can be calculated as $c_L = l/t_L$ for P-waves and as $c_S = l/t_S$ for S-waves. With the density ρ of the sample the shear modulus G is given by

$$G = c_T^2 \rho, \tag{2.1}$$

and the Poisson's ratio ν is given for $(c_L/c_T)^2 > 2$ by

$$\nu = \frac{1}{2} \cdot \frac{2 - (c_L/c_T)^2}{1 - (c_L/c_T)^2}. \tag{2.2}$$

The Young's modulus E can be calculated from these two constants by

$$E = 2G(1 + \nu). \tag{2.3}$$

Elastic material constants have been determined with high deformation rates and very small deformations and for a variety of wax-like materials, representative results will be presented in Chap. 3.

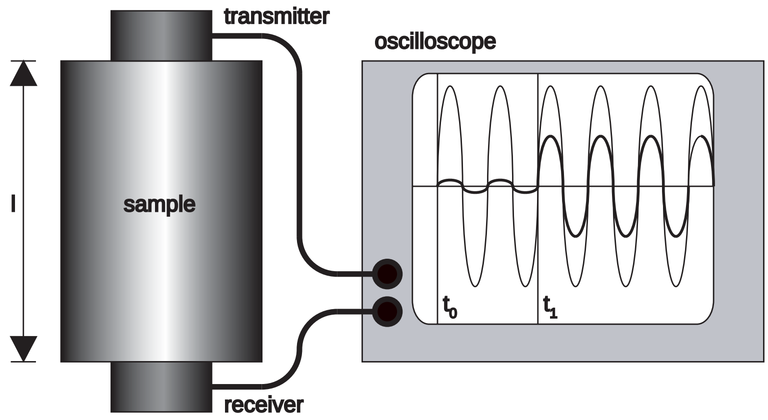

Figure 2.1: Testing device for measuring the velocity of wave propagation

2.3 Tests with paraffin

2.3.1 Material

Viscoplastic material properties were first studied with *paraffin*. The name is derived from the Latin *parum affinis* which means lacking reactivity. Generally, the term paraffin is used as a synonym for alkanes which are saturated hydrocarbons with the stoichiometric formula C_nH_{2n+2}. The range of alkane spans from CH_4 (i.e. methane, a gas at room temperature) to the heaviest molecule $C_{40}H_{82}$. Some members of the alkane series such as octane (C_8H_{18}) are liquid at room temperature. The molecules from $C_{20}H_{42}$ to $C_{40}H_{82}$ are solid at room temperature and are also termed paraffin wax. Thus, the term paraffin is generally used for liquid paraffin (i.e. an oil) as well as for solid paraffin (i.e. paraffin wax). In the sequel the term paraffin is used as an abbreviation instead of the term paraffin wax.

At room temperature, paraffin is a wax-like solid which is commonly known from candles. In contrast to natural (organic) beeswax, paraffin is an artificial wax which is produced in the hydrocarbon industry. Paraffin is an odorless, tasteless and non-toxic substance and is, if not artificially colored, opaque-white. The opaqueness of paraffin results from the lengths of its molecule chains which are in the same range as the wavelengths of visible light. The density of paraffin is approximately 0.9 g/cm^3. The melting point ranges from 47 to 64 °C. Paraffin exhibits elastic and (markedly nonlinearly) viscous properties which can be studied with laboratory tests at moderate stresses. Paraffin is isotropic due to its amorphous structure.

Samples which are required for laboratory testing can be prepared from solid paraffin blocks. However, in order to avoid pores and inhomogeneities in the material, it is recommended to melt the paraffin and to fill the warm fluid into a chill mould. The chill mould should have the final shape of the sample, e.g. a cylindrical shape for a shortening test. Nevertheless, the soft and ductile material enables a subsequent modification of a solidified sample, e.g. with a turning-lathe. Fig. 2.2 shows an opaque white cylindric paraffin sample for later use in a shortening test, with a ruler and a reference color bar. The suggested method enables the production of a sufficient number of samples with identical, almost arbitrary shapes and with identical properties. Spatial fluctuations of the material properties are small. Therefore, reproducible laboratory tests can be carried out.

The absence of pores indicates independence of the behavior on the mean pressure which implies purely deviatoric viscoplastic behavior. Thus, barotropy and pyknotropy can be neglected. A hydrogel, which is described in detail in Chap. 5, exhibits likewise a

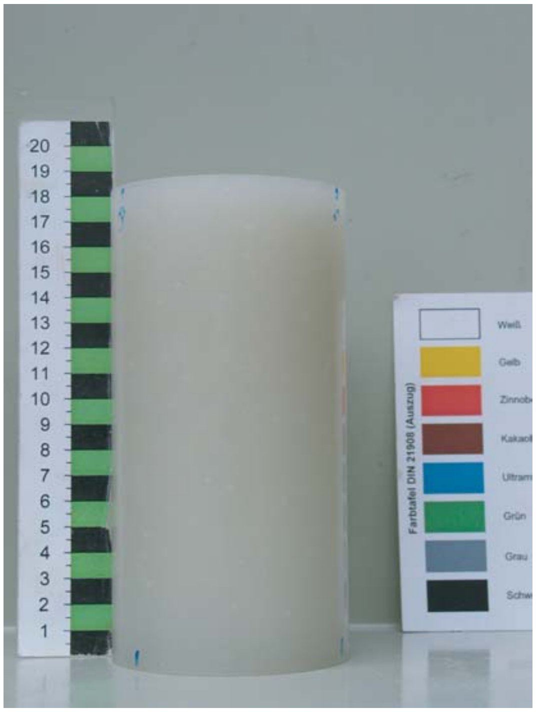

Figure 2.2: Cylindrical paraffin sample with ruler (cm) and reference color bar

thermally activated viscoplastic behavior. Due to its soft particles, thermal activation predominates also the viscoplastic behavior of paraffin at room temperature and with sufficiently low deformation rates. Sufficiently high deformation rates cause cavitation, i.e. the formation of pores. This can already be observed as a local turbidity (milkyness) of the sample. The material becomes barotropic with the formation of pores, and so it is no longer in the subcritical (viscoplastic) regime because shear localization evolves from the pores. An increase of the deformation rate induces shear bands and fractures, thereafter the material behavior becomes clastic (Fig. 2.9). These reproducible phenomena could also be observed with lower deformation rates at lower temperatures. The own laboratory tests were carried out at constant room temperature (approx. $T = 22$ °C).

2.3.2 Unconfined shortening test with controlled axial loading (creep test)

The evolution of viscoplastic deformations can be studied with cylindrical paraffin samples with unconfined shortening tests. The testing device enables the application of a constant axial force to the sample's upper surface by means of weights (Fig. 2.3), thus the axial loading of the sample is controlled (unconfined creep test). The evolution of the axial shortening of the sample is recorded. The average axial stress in a cross-section perpendicular to the sample axis can be assumed to be constant in case of a constant axial force, at least for small deformations. Changes of the average stress can also be approximated assuming cylindrical deformation of the sample at constant volume due to the absence of pores.

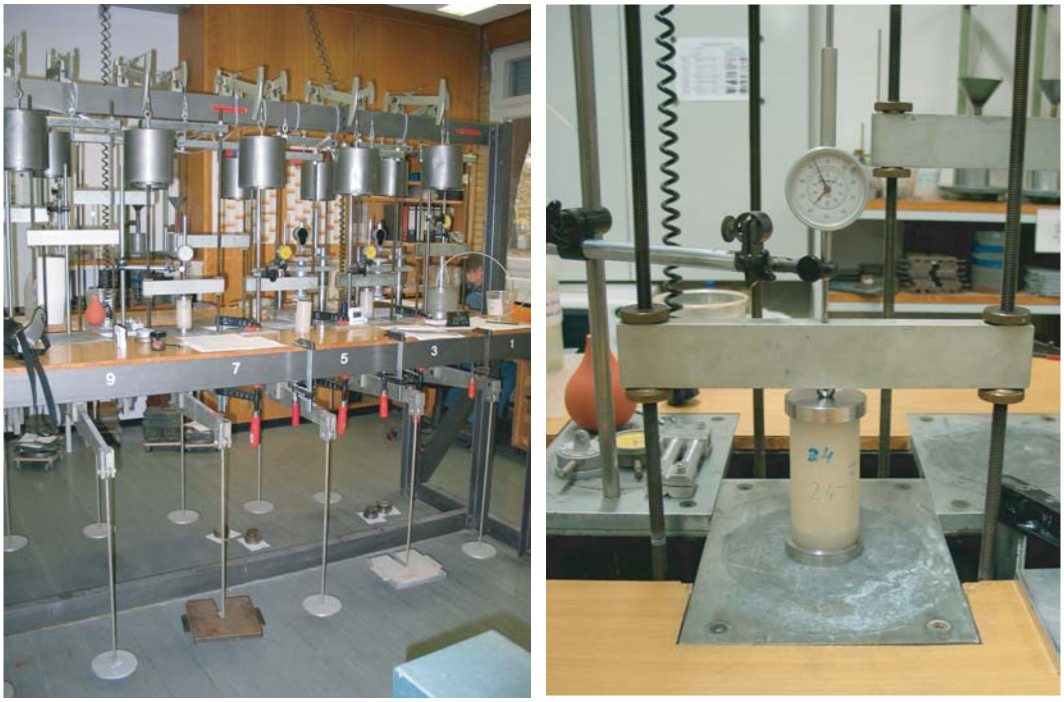

Figure 2.3: Creep test device

Fig. 2.4 shows the result of an unconfined creep test with paraffin. The test was carried out with four load stages (Tab. 2.1). At the onset of the test, a constant axial stress (stage 1) of σ_1 = 44 kPa was applied to the sample. An immediate elastic shortening of the sample can be observed, but the material exhibits also a markedly viscoplastic behavior as the axial shortening continues with time. It appears that after a transition time the constant axial stress leads to a constant rate of axial shortening, i.e. *stationary creep*. Stationarity implies that the material is in a stable state. New pores may be induced due to plastic deformation, but preexisting pores vanish at other locations within the same period of time. Thus, there is a zero net change of pores in the material with stationary creep.

An increase of axial stress to a higher value σ_2 = 88 kPa (stage 2) leads to an immediate elastic shortening of the sample and also to a disproportionally high increase of the deformation rate. It appears that after a transition time stationary creep is reached again with a higher constant creep rate if the axial stress is kept constant. The stationary creep rate of the first load stage can be nearly reached again with a reduction of the axial stress to its initial value $\sigma_3 = \sigma_1$ (stage 3). A subsequent decrease of the axial stress to a lower

than initial (stage 4: $\sigma_2 = 22$ kPa) leads to a disproportionally high decrease of the axial shortening rate. As for the other load stages, it appears that stationary creep is reached again after a transition time.
Tab. 2.1 shows the shortening rates for the four load stages which have been determined from Fig. 2.4 after stationary creep has been reached. The results of the test reveal that an increase or decrease of the axial stress by factor two results in an increase or respectively decrease of the stationary creep rate by approximately factor ten. Thus, the creep behavior of paraffin is markedly nonlinear. The power law which is suggested in Sec. 3.3 can be considered as a good approximation for the relationship between the axial stress and the axial shortening rate in an unconfined creep test.

Table 2.1: Load stages and corresponding time periods Δt with constant axial stresses σ, and resulting shortening rates $\dot{\epsilon}$ for stationary creep for an unconfined creep test with paraffin

stage	Δt [h]	σ [kPa]	$\dot{\epsilon}$ [1/min]
1	48	44	4E-6
2	3	88	3E-5
3	47	44	4E-6
4	126	22	3E-7

2.3.3 Unconfined shortening tests with controlled axial deformation velocity

The argotropic behavior of paraffin was studied with a number of unconfined shortening tests with cylindrical samples. Since the tests are well reproducible, characteristic results are outlined with few representative tests. Differences in the results of comparable tests (e.g. different maximum axial stresses at comparable shortening rates) are due to differences of the environmental testing conditions (temperature). The laboratory in which the tests have been carried out was not air-conditioned, and the material behavior appears to be sensitive to small temperature changes. For improved test results it is recommended to carry out tests at precisely constant temperature. This has been realized for the triaxial tests with geomaterials which are presented in subsequent sections.

The unconfined shortening tests with paraffin were carried out in a UTS testing device which enables a control of the axial displacement velocity (Fig. 2.5). A cylindrical sample is placed between the two load plates of the testing device. Friction at both contact

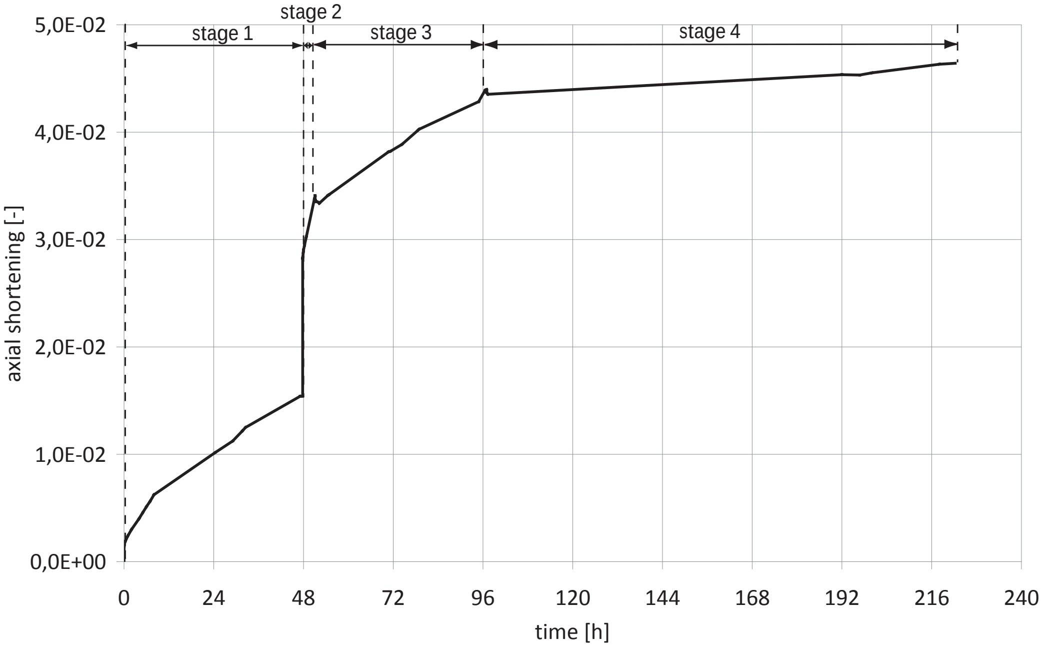

Figure 2.4: Unconfined creep test with paraffin

surfaces between the sample and the load plates was reduced with interlayers of thin teflon sheets. The relative axial motion between the two load plates is recorded with a displacement sensor.
With the chosen testing device, a constant axial deformation velocity can be controlled in the range of 0.001 - 500 mm/min. Nevertheless, since the sample is shortened axially, the axial shortening rate is increasing at a constant velocity. The relative increase of axial shortening rate at the same velocity is higher with shorter samples. However, this geometrical effect can be neglected for small shortenings relative to the sample height. Thus, the axial shortening rate has been assumed to be constant for evaluations.
The resulting axial force F which is applied to the sample is measured with a load cell. The average axial stress in a cross section of the sample can be calculated from the measured force F and the actual area A of the cross-section of the sample. The assumption of cylindrical deformation holds for $A = A_0 * l_0/l$, where A_0 and l_0 are the initial cross-section area and length of the sample and l is the measured actual length of the sample.

Fig. 2.6 shows a representative result of an unconfined shortening test with several stages of section-wise constant shortening velocity. Table 2.2 gives an overview about the shortening rates at constant velocity stages. The test starts with an axial shortening rate $\dot{\epsilon}$ = 2E-4 1/min (stage 1). The average axial stress increases with continued deformation. A limit state is asymptotically attained with smooth transition and characterized by a

Figure 2.5: UTS testing device with cylindrical paraffin sample

maximum axial stress response. A kind of plateau of the axial stress indicates a steady state [13].
A sudden decrease or increase of the shortening rate by one power of ten to $\dot{\epsilon}$ = 2E-5 1/min (stage 2) or $\dot{\epsilon}$ = 2E-3 1/min (stage 4) results in a decrease or respectively increase of the axial stress. A new steady state with a limit stress which corresponds to the actual shortening rate is reached after a transition time. A sudden change of the axial shortening rate back to the initial value leads again nearly to the initial limit stress (stages 3 and 5). A sudden increase of the initial shortening rates by two powers of ten leads to a disproportionally high increase of the limit stress, but still to a continued viscoplastic deformation of the sample (stage 6).

The test was terminated when an axial shortening of 16% was reached. Fig. 2.7 shows the paraffin sample before (a) and after (b) the test. The sample gets shorter and its diameter increases with continued deformation, but the cylindrical shape of the sample is almost preserved even after an axial shortening of 16%. Only a slight bulging of the cylindrical surface was observed at the end of the test. The bulging may be caused by some residual friction at the contact faces between the sample and the load plates.
The photos also reveal that the sample is still opaque at the end of the test. Visible pores or turbid areas are absent. The viscoplastic deformation is dominated by thermally activated displacements during this test. The numbers of newly generated and vanishing micropores are of the same magnitude within the same (sufficiently long) time period, but

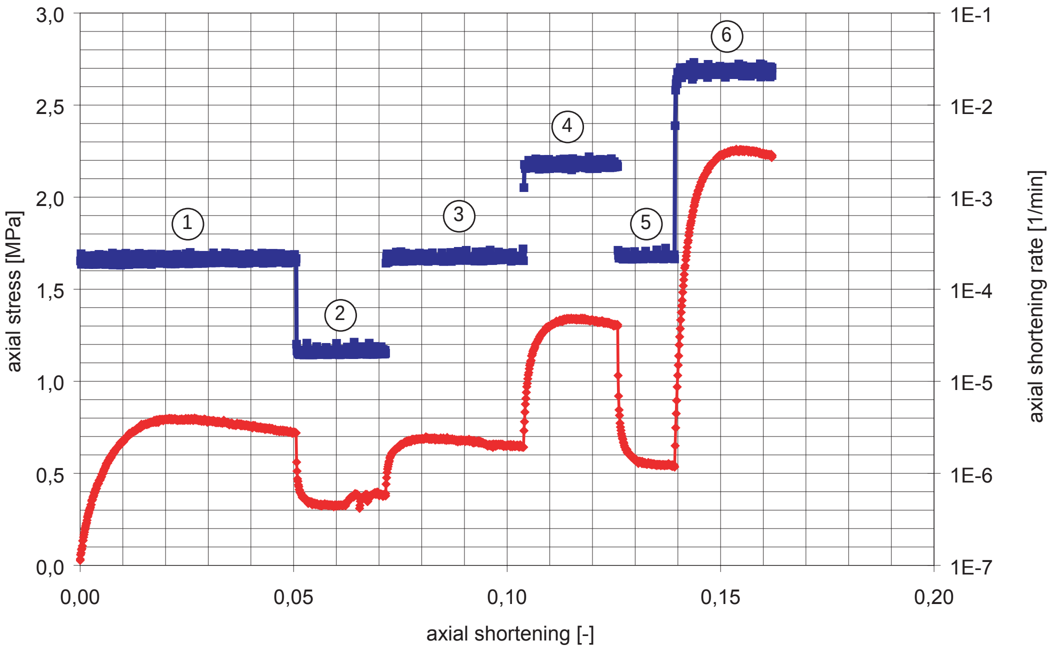

Figure 2.6: Viscoplastic behavior in an unconfined shortening test with paraffin, axial shortening rate (blue) and axial stress (red) vs. axial shortening

Table 2.2: Unconfined shortening test with paraffin, shortening rates at constant velocity stages

stage	$\dot{\epsilon}$ [1/min]
1	2E-4
2	2E-5
3	2E-4
4	2E-3
5	2E-4
6	2E-2

the numbers are not equal as they would be in a stationary state. A steady state with a material with pores (even micropores) is theoretically possible, but not attainable with axially symmetric samples. The evolution of axial stress vs. axial shortening (Fig. 2.6) indicates that after the maximum axial stress has been reached this is slightly decreasing at a constant shortening velocity (stages 1, 3, 5). A slight increase of the shortening rate due to continued shortening at constant velocity implies a slight increase of axial stress. It appears that the number of micropores increases with the chosen shortening rate $\dot{\epsilon}$ = 2E-4 1/min, i.e. more pores are generated than are vanishing within the same time

period. This leads to a decrease of the average axial stress in the sample, commonly called *softening*. An increase of the shortening rate enhances this effect (stages 4, 6).
A lower shortening rate (e.g. $\dot{\epsilon}$ = 2E-5 1/min at stage 2) reveals a slight increase of the average axial stress in the sample after a minimum of stress was reached. The number of vanishing micropores is then evidently higher than the number of newly generated micropores with this shortening rate. Thus, with sufficiently low shortening rates the material enables a kind of *self-healing* (commonly called hardening).
The number of micropores is not critical during this test as the micropores do not tend to join each other. They do not grow up to macropores, and locally limited turbidity is not visible. In other words, the material is ductile within the chosen range of shortening rates.

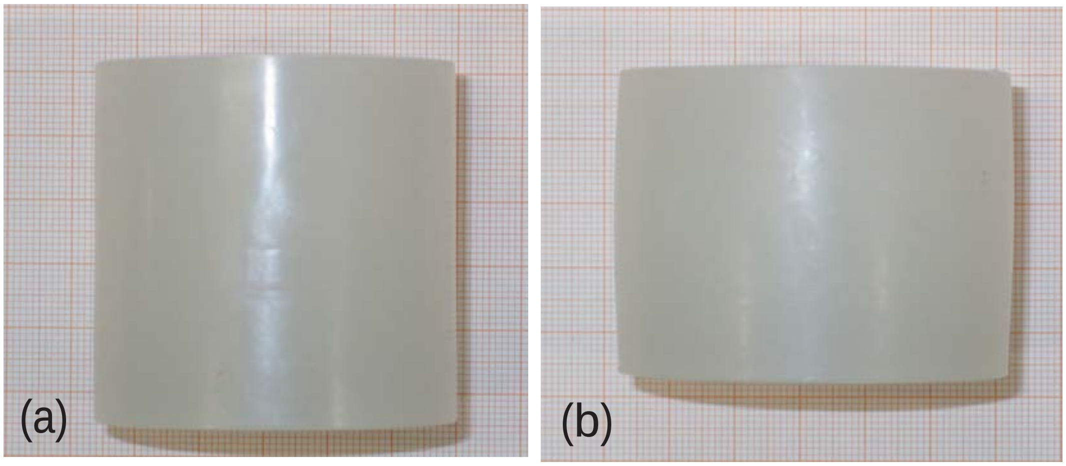

Figure 2.7: Unconfined shortening test with paraffin, sample before (a) and after (b) the test

Sufficiently high shortening rates lead to a fast generation of micropores which combine with each other. This enables micropores to grow up to *macropores* and *flat pores*. Fig. 2.8 shows the result of an unconfined shortening test with higher shortening rates. The test has been carried out with seven stages of constant shortening velocities which are shown in Table 2.3. Maximum axial stresses are reached again with temporarily constant shortening rates. The material remains stable, and thus in the ductile regime with the sub-critical shortening rates of the stages 1 to 5. The sample has been deformed viscoplastically up to an axial shortening of 10.5% during these stages. The test results indicate again a slight softening for a shortening rate $\dot{\epsilon}$ = 3E-4 1/min.
An increase of the shortening rate to $\dot{\epsilon}$ = 2E-2 1/min (stage 6) leads to an increase of the axial stress up to a marked *peak*, which is followed by a sudden decrease of the average axial stress with continued deformation. The stress increase up to the peak is accompanied by the onset of *shear localization* with a visibly increasing turbidity of the material. A

short time before the peak is reached, continued deformation leads to the evolution of multiple *helical shear bands.* Fig. 2.9 shows a sample with helical shear bands after a one-stage unconfined shortening test with a correspondingly high shortening rate.

In this context, the *strength* may be defined as the maximum average axial stress which is attainable at a constant shortening rate. The peak of the average stress indicates a *critical point* at the verge of the ductile regime. At this critical point any small additional deformation (i.e. a small disturbance of the actual state) causes a significant change of the stress state and a localization. Before reaching this critical point, the number of pores in the material is subcritical and the deformation of the sample is viscoplastic. The material behavior becomes *clastic* (from Greek: klaso = to break) when surpassing this critical point, and the strength is significantly reduced. The number of pores increases dramatically, and the pores grow locally up to flat pores with preferred orientations (i.e. polarization). Shear bands develop along these orientations. Shear localization leads finally to a loss of integrity of the sample.

The test results (Fig. 2.8) reveal that a subsequent strong reduction of the shortening rate by two powers of ten (stage 7), down to the initial shortening rate, matters hardly for the responding average axial stress in the sample. Within this shortening time self-healing is no more sufficient to cause a marked stress increase. Even a drastic reduction of the deformation rate, or no further deformation, would not lead to a stabilization of the actual state without confining pressure.

A power law model as discussed in Chap. 3 is a good approximation of the viscoplastic stress-deformation behavior of the material up to a critical point. With the onset of clastic behavior, this model is no more valid. In other words, for any state at and beyond a critical point the assumption of ductility is no longer valid. Thus, numerical simulations with this model are misleading for the clastic regime.

Table 2.3: Unconfined shortening test with paraffin, shortening rates at constant velocity stages

stage	$\dot{\epsilon}$ [1/min]
1	3E-4
2	3E-5
3	3E-4
4	3E-3
5	3E-4
6	3E-2
7	3E-4

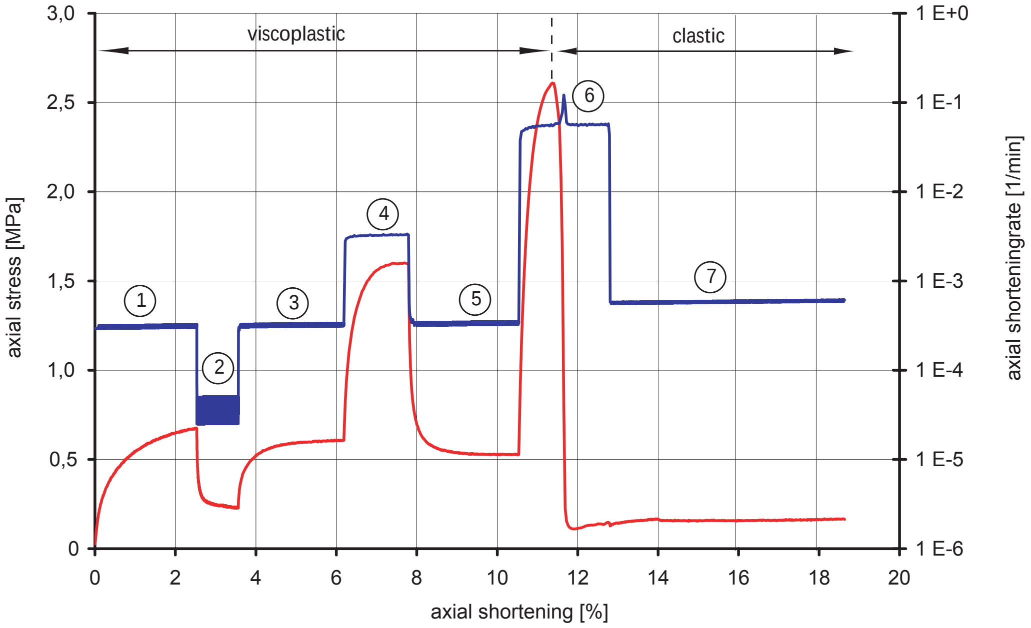

Figure 2.8: Viscoplastic and clastic behavior in an unconfined shortening test with paraffin, axial shortening rate (blue) and axial stress (red) vs. axial shortening

2.3.4 Keroid behavior

Viscous effects (i.e. argotropy, creep and relaxation) were first studied with paraffin. They resemble those of geomaterials like ice or rock salt with slow deformations. It is usually assumed that solids without pores can exhibit anelastic deformations without change of volume, and that the mean pressure does not influence the anelastic material behavior. Soft soils exhibit a similar behavior if they are fully saturated, as long as the pore fluid is incompressible and its filtration is excluded or can be neglected. Similar laboratory tests have been carried out with geomaterials. Their results, which are explained in subsequent sections, show that the viscoplastic behavior with sufficiently low deformation rates is similar to the behavior of paraffin in the subcritical state. Thus, one may say that these materials are *keroids* (waxlike, from Greek: keros = wax) in the subcritical regime. 'Keroid behavior' implies the following idealizing assumptions:

- isotropy of material properties,
- nonlinear viscosity,
- negligible volumetric viscosity,

Figure 2.9: Evolution of helical shear bands with an unconfined shortening test with paraffin, courtesy K. Balthasar

- dominant thermal activation and negligible seismic activation via pores,
- viscoplastic ductility for sufficiently low deformation rates.

Ductility and viscoplasticity come always together and hold for a suitable range of deformation rate, pressure and temperature. Micropores can occur in the ductile regime in a minute fraction which increases spontaneously at the verge of ductility.

These idealizations may be assumed, with suitable boundary conditions, for the following materials:

- paraffin (wax),
- hydrogels,
- ice,
- frozen saturated soil,
- saturated clay without drainage,

- claystone and mudstone,
- salinary rocks (e.g. rock salt),
- fissured rock with soft gauge fill,
- hard rock with high pressure, high temperature and/or extremely low deformation rates.

As energy is dissipated in any inelastic deformation, a sufficient heat conduction is required to avoid a substantial rise of temperature. Otherwise, fast deformation results in self-heating and weakening of the material. One can observe this by tearing a wire of ductile metal into pieces by rapid stretching. Heating can be felt near the point of rupture.

The evolution of macropores and shear localizations indicates the end of viscoplastic and the onset of clastic behavior. High deformation rates lead to brittle fracture and the loss of integrity of a sample. Fig. 2.10 shows a shear band pattern of a flat paraffin sample (disk) which was induced in an unconfined shortening test with a rather high axial shortening rate. The shear band pattern resembles fault patterns in tectonically deformed geological formations (e.g. uplifted cap rock overlaying a diapir). Fig. 2.11 shows a typical pattern of crossing conjugate normal faults across the anticlinal crest of a diapir. Paraffin may thus serve as a representative material for nearly pore-free geomaterials and other solids, which are composed of soft solid particles and bound fluid with a minute constituent of gas pores and a minute fraction of micropores. Paraffin is also suitable to study both viscoplastic and clastic behavior.

2.4 Tests with reconstituted bentonite samples

2.4.1 Material

Laboratory tests have also been carried out with artificially prepared samples of geomaterials in order to study their viscoplastic behavior. Natural samples of geomaterial are often inhomogeneous due to their genesis (e.g. layered sedimentary rocks). Furthermore, sampling of geomaterials (e.g. coring of rock) leads to disturbances of the initial state of the samples. High spatial variations of material properties are inherent to all natural samples. Systematic studies of material properties are difficult with natural samples since results of laboratory tests are hardly reproducible due to variations of material properties. A minimization of the variability of the material properties helps to avoid misinterpretations of the test results. Therefore, artificially prepared samples have been chosen. As

Figure 2.10: Shear band pattern of a flat paraffin sample after unconfined shortening with high axial shortening rate (courtesy K. Balthasar)

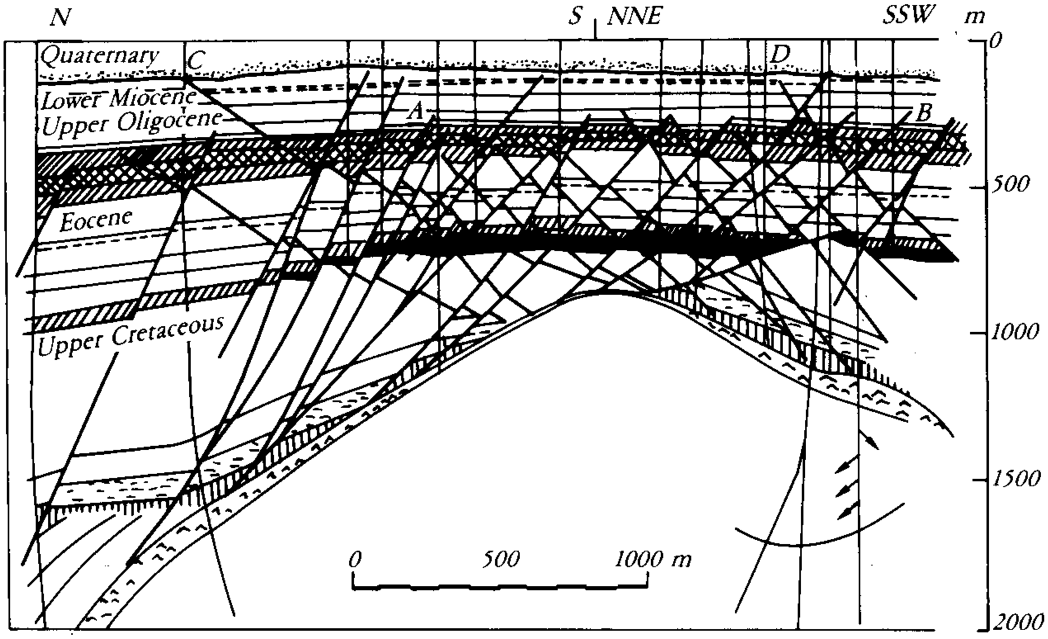

Figure 2.11: Fault patterns above Reitbrook salt dome (Northern Germany), from [12]

pointed out for paraffin samples, reconstituted samples of geomaterial enable also the production of a sufficient number of cylindrical samples with identical properties. Spacial fluctuations of the material properties are quite small. Disturbances due to sampling is excluded. Therefore, reproducible laboratory tests can be carried out with reconstituted samples. Due to extensive deformations, the material in a clay smear is remolded. Thus, its behavior can be investigated with reconstituted samples.

Reconstituted samples were prepared from *bentonite* powder. The term bentonite was first used to describe a plastic clay in upper cretaceous tuffs from a deposit in the vicinity of Fort Benton (Wyoming, USA). Bentonite can be defined as a clay which consists mainly of clay minerals of the *smectite* group. *Montmorillonite* is the most widespread form of smectite and represents the main clay mineral of bentonite. The term montmorillonite is derived from the town Montmorillion in southern France, a place where these clay minerals can be found. Bentonite originates often as a transformation product of volcanic rocks through hydrothermal solutions. The formation of smectitic clay minerals from volcanites is mainly based on the decomposition of minerals and volcanic glasses through hydration and hydrolysis. The structure of smectites consists of two tetrahedron layers and one octahedron layer in between. Due to an ion exchange process, whereby higher valency ions are replaced by lower charge ions, the silicate layers of montmorillonite have a weakly negative charge. This is compensated by the adsorption of counter-ions (e.g. calcium, magnesium or natrium ions) in the interlayers between the silicate layers. The mineral charge permits an expansion of the interlayer spaces to deposit the counter-ions with their hydrate charge (inner crystalline swelling). Natrium-montmorillonites can store large quantities of water in the interlayers and on the mineral surfaces, thus they have a large swelling potential.

Fig. 2.12 shows photographs of clay minerals of montmorillonite (a) and kaolinite (b) which have been taken by means of an ESEM (Environmental Scanning Electron Microscopy). Compared with kaolinite minerals, montmorillonites reveal a considerably finer granulometric structure. *Kaolinite* e.g. is often composed of silicate layers which have the structure of stapled books or coins (a2 and a3). In contrast, montmorillonite minerals are mostly smaller than one micrometer (b2). The silicate layers of montmorillonite are often flexible and pliable, which is clearly identifiable by means of ESEM (b3). Reconstituted samples of kaolinite have clay minerals that are orientated in planes which are perpendicular to the axial direction of the oedometric compression (a1). In contrast to that, reconstituted samples of montmorillonite exhibit an irregular orientation of the clay minerals (b1), thus there is no inherent anisotropy. The shape of the clay minerals resembles those of crumbled paper hankies. Bentonite has been chosen because of the homogeneity and isotropy of the samples reconstituted with this material.

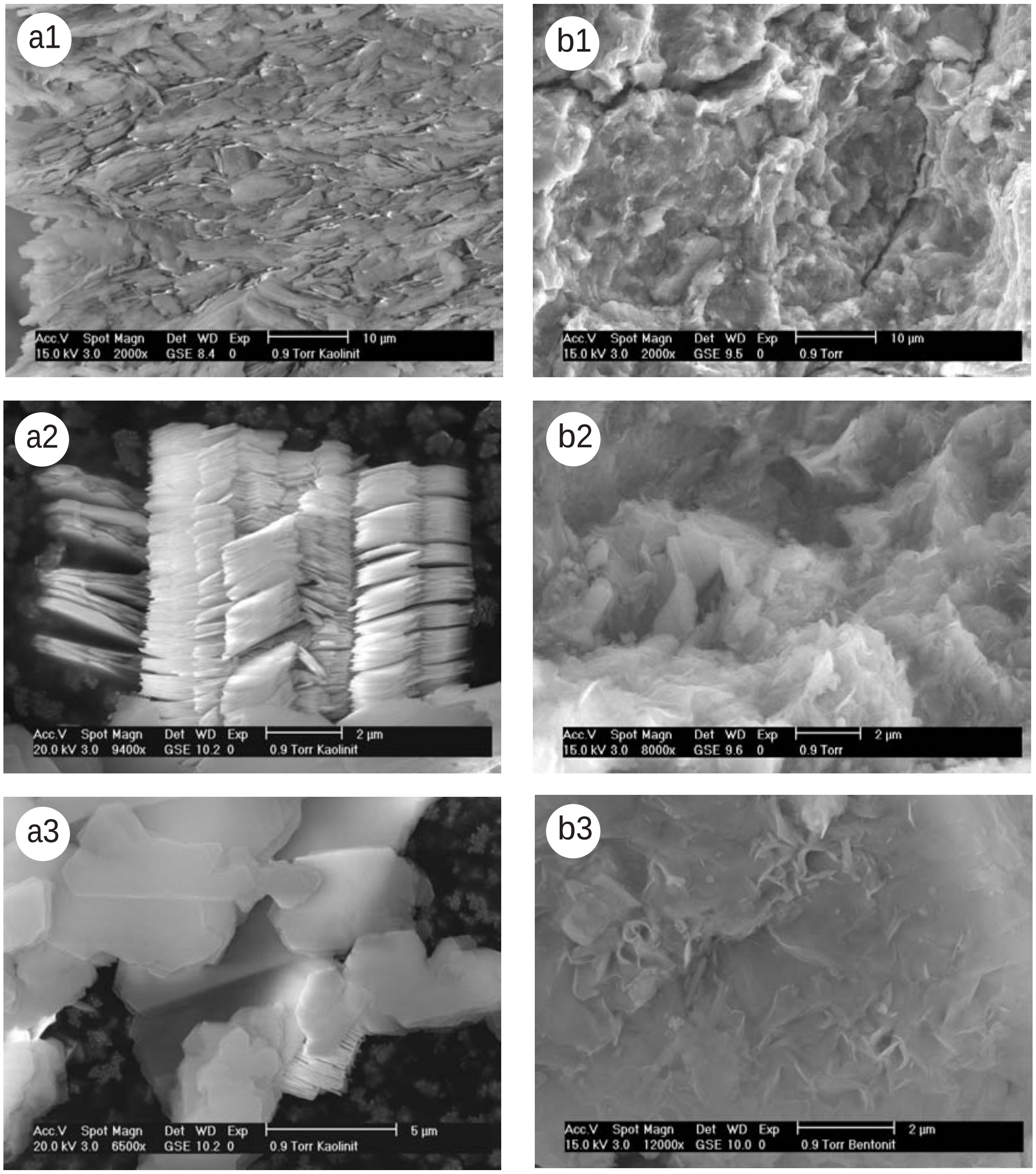

Figure 2.12: Different size and structure of clay minerals of kaolinite (a) and montmorillonite (b); photographs taken by means of ESEM with kind support at the Institute of Mineralogy and Geochemistry, Forschungszentrum Karlsruhe (now KIT)

The properties and potential applications of bentonite depend mainly on the swelling capacity of the smectitic clay minerals and on the the exchange of cations that are bound in the interlayer spaces. Theses properties may vary considerably from deposit to deposit due to differences in the structural set-up, the distribution of charges, the type of cations in the intermediate layers, the grain size and shape, etc. In order to optimize their properties for an intended application, bentonites are subjected to industrial treatments which range from classification, drying and grinding to activation with acids, alkalies and various organic substances. As an industrial product bentonite powder is available in large quantities with quality controlled properties. Thus, variations of the material properties are negligible for samples prepared from the same product of the same manufacturer. A natrium-bentonite from S+B Industrial Minerals (Mannheim, Germany) was used for the preparation of the artificial samples.

The initial natural water content of 10-12% of the bentonite was increased up to 17-19% in order to reach a saturation of the reconstituted samples of 90-95%. The bentonite powder was conditioned in a humid-controlled enviroment for this purpose. The high specific surface of motmorillonite (up to 800 g/m^2) enables a sufficient water absorption from the humid air. Fully saturated samples have been prepared from a suspension of clay minerals and water by very careful oedometric compression from a suspension.

For the reconstitution of bentonite samples a novel oedometric compression device has been developed by the author. A defined quantity of bentonite powder is filled into the cylinder of the device. The material gets compressed with a piston by means of an uniaxial testing device. The design with a suitable combination of materials and a very precise manufacturing of the parts of the device enables oedometric compression of the bentonite powder up to an axial stress of 150 MPa. Fig. 2.13 shows a schematic sketch of the compression device. The result is a perfectly cylindrical sample (Fig.2.14). Subsequent surface processing of the sample is not required. The reconstituted sample has a specific weight of approximately 2.2 g/cm^3.

The very high compression of the material and the subsequent small extension during unloading to atmosphere pressure leads to a suction (i.e. negative porewater pressure) in the sample. The suction amounts approximately 50 MPa and can be estimated by means of the equations of Kelvin and Laplace [13]. The suction in the sample remains in equilibrium with the atmosphere as long as drying and capillary entry are prevented.

2.4.2 Shortening tests with controlled axial deformation velocity

Unconfined shortening tests have been carried out with reconstituted bentonite samples by means of a UTS testing device. Cylindrical samples with an initial diameter of 70 mm have been used for the tests. Short samples with a height to diameter ratio of 1 have been chosen for the tests in order to achieve a rather homogeneous stress field in the sample. Bulging and chipping of the surface of the samples can be reduced with cylindrical deformations of short samples if the friction between the sample and the load plates of the testing device is minimized. The minimization has been realized with layers of thin teflon sheets between the sample and the load plates of the testing device.

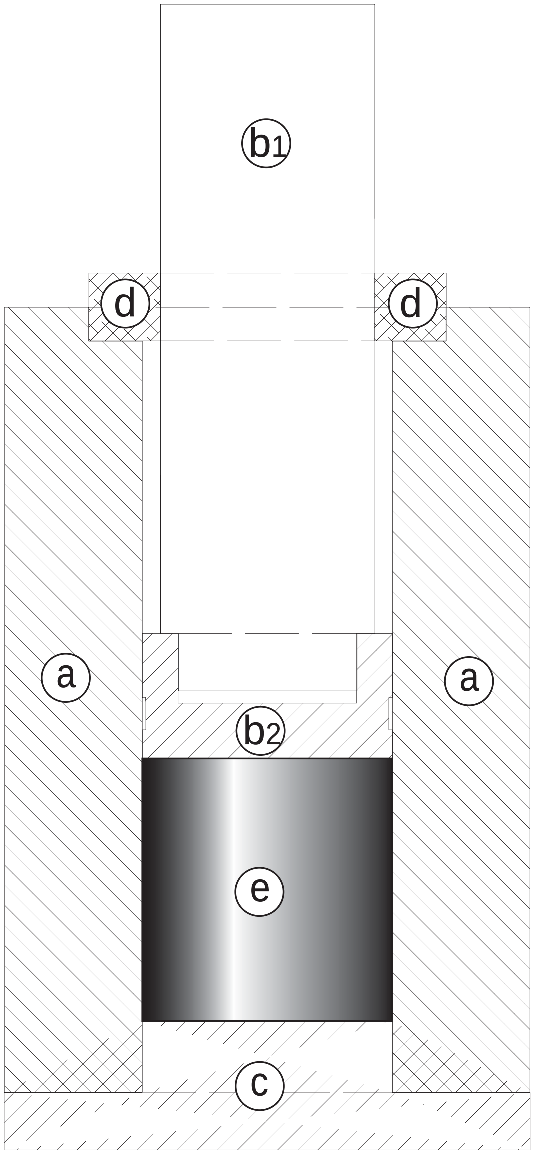

Figure 2.13: Oedometric compression device for producing reconstituted samples with cylinder (a), upper piston (b1), lower piston (b2), bottom plate (c), guide ring (d) and sample material (e)

Confined shortening tests have been carried out by means of a novel testing device with high precision rate control. The testing device enables a confined shortening with a maximum confining pressure of 12 MPa. Cylindrical samples with a maximum diameter of 90 mm and a maximum height of 180 mm can be tested. The maximum axial force which can be transmitted by the device is 100 kN. Thus, the testing range of axial stresses can be extended by using samples with smaller diameters. The testing device enables a high precision control of the axial deformation velocity of the sample within the wide range from 0.001 to 10 mm/min. The testing device can be controlled by a personal computer

Figure 2.14: Reconstituted bentonite sample after compression with 150 MPa

and enables individual changes of the boundary conditions (e.g. the axial shortening velocity) during a test.

Fig. 2.15 shows an evolution of the average axial stress in the sample with continued axial shortening during an unconfined shortening. The axial shortening velocity has been kept constant at v_{ax} = 0.1 mm/min during the test. This corresponds to an axial shortening rate of d_{ax} = 1.4E-3 1/min with an initial height h_0 = 70 mm of the sample. Fig. 2.15 shows an increase of the incremental stiffness of the sample up to an axial shortening of approximately 0.15%, which results from initially imperfect contacts between the sample and the load plates. Small deformations are required for uniform contact pressure. Continued shortening leads to an increase of the axial stress with decreasing incremental stiffness. The decrease of the stiffness appears to be small up to a shortening of 0.5%, but continued deformation leads to a disproportionally low increase of the average axial stress in the sample. A slight *crackling-noise* was heard at an axial shortening of 1.0%, the test was stopped immediately. Fig. 2.15 reveals that a critical state with the maximum axial

stress (commonly called unconfined compressive strength) was reached.
Fig. 2.16 shows a sample immediately after the test. Axial fractures can be observed at the cylindrical surface (Fig. 2.16(a)). Fig. 2.16(b) reveals that these axial fractures propagate in radial direction toward the axis of the sample up to a polygonal fracture which is surrounding the axis. The fracture layout at the upper surface of the sample is slightly asymmetric. A perfect plane-parallelity of the upper and lower surfaces of the sample is practically impossible so that fractures start and propagate asymmetrically from imperfections.

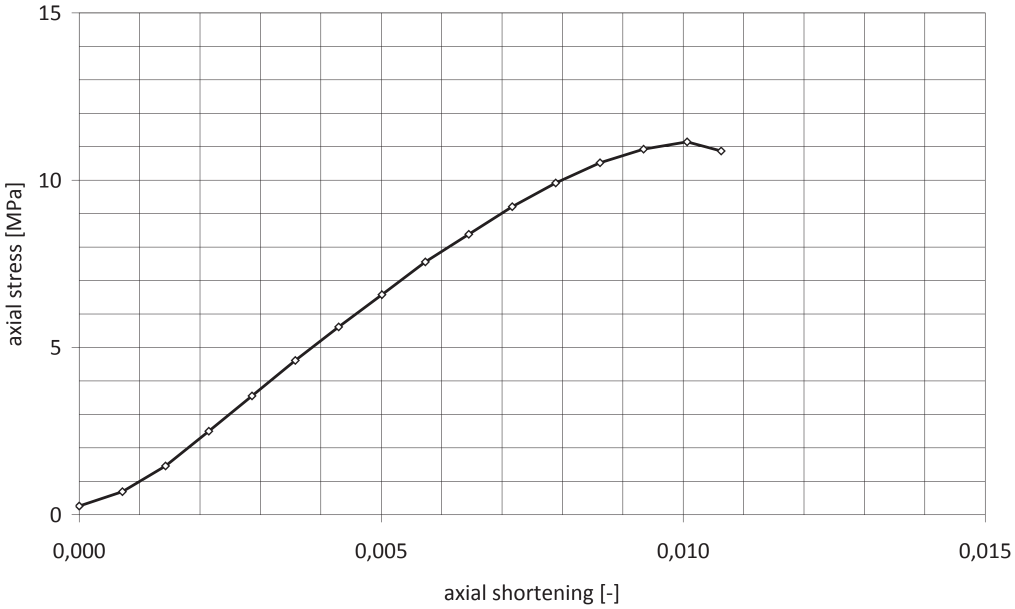

Figure 2.15: Unconfined shortening test with a reconstituted bentonite sample, evolution of axial stress vs. axial shortening at constant shortening rate d_{ax} = 1.4E-3 1/min

Axial shortening with a constant volume of the material leads to lengthening in radial and tangential directions of the sample (lateral spreading). This causes an increase of the radii of curvature of the water menisci between adjacent solid particles (i.e. phyllosilicate clay minerals). A critical point is reached if the water membrane is teared apart according to the equation of Laplace for the proportional relationship between capillary stress and curvature of the fluid membrane [16]. The maximum axial stress in the sample cross-section is reached at this critical point. *Cavitation* is induced at first at the cylindrical surface of the sample which is the location of the highest lengthening. Fractures start from this surface and propagate toward the interior. The cavitation, and thus the fracturing of the material, causes new surfaces with energy dissipation which can be heard as *acoustic emission* in a quiet environment (crackling-noise). Thus, an acoustic emission indicates

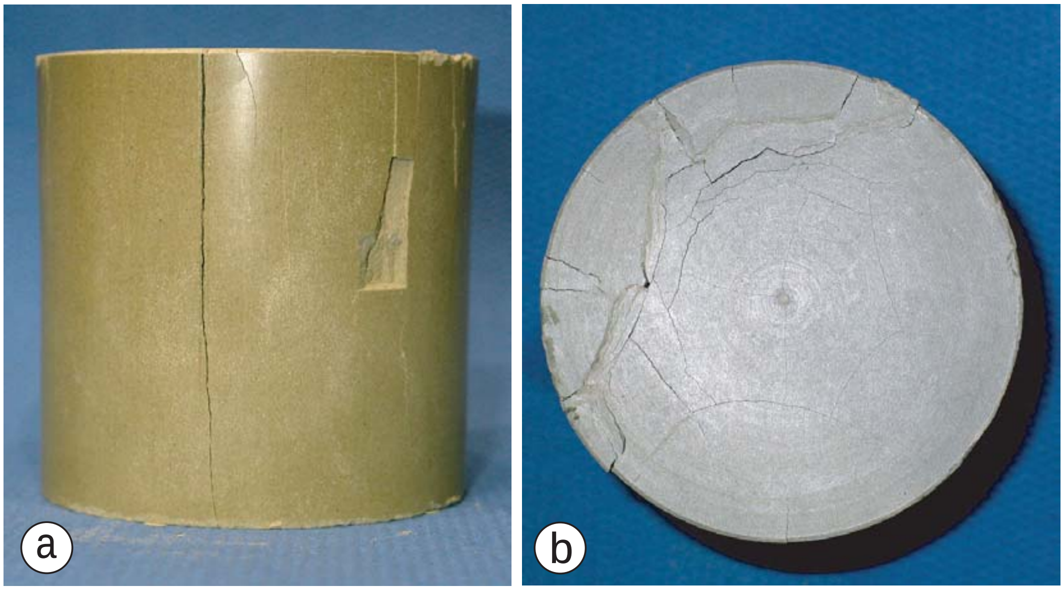

Figure 2.16: Axial splitting of a reconstituted bentonite sample, axial cracks at the cylindrical surface (a) and radial and polygonal cracks at the upper surface (b)

the onset of clastic behavior at a critical point.
In the subcritical state, the viscoplastic deformation of the bentonite is thermally activated due to its soft solid particles (i.e. clay minerals), and the material can be said to be *ductile*. For materials with hard solid particles, e.g. quartz grains of a sand, thermally activated displacements are of minor relevance. Redistributions of intergranular stresses and deformations of materials with hard solid particles are dominated by seismic activation [13]. A significant increase of seismic events can be also observed with materials with soft particles in the vicinity of a critical point (commonly spoken: short time before a critical point is reached). These seismic events are caused by the formation of flat pores, i.e. the generation of new surfaces. The material is still in a subcritical state, but the increase of seismic events indicates the proximity of a critical point. These seismic events can be recorded with sufficiently sensitive geophones. Overlaying environmental noise can be filtered. Seismic events can be heard in a quiet environment, so until present tunneling and mining staff uses to listen to the crackling of the surrounding rock as an important indicator for their own safety. The in-situ monitoring of seismic events is indispensable for maintaining rock in a subcritical state.

The range in which the material is viscoplastic (i.e. the ductile regime) can be extended with a confining pressure. Fig. 2.17 shows the evolution of the average axial stress in a reconstituted bentonite sample which has been prepared like the sample used for the unconfined shortening test described above. The confining pressure was kept constant at $\sigma_{rad} = 5$ MPa during the test. The axial shortening velocity was kept constant during the test at v_{ax} = 0.1 mm/min, this corresponds to a constant axial shortening rate of d_{ax} = 1.4E-3 1/min. Thus, the evolution of the stress of the confined shortening test can be compared with the result of the unconfined test with respect to the same shortening rate. The *Roscoe-invariant* of deviatoric stress $q = (\sigma_{ax} - \sigma_{rad})/2$ has been evaluated for confined compression tests. In the sequel the term *deviatoric stress* is used as an abbreviation instead of the term Roscoe-invariant of deviatoric stress for evaluations of laboratory tests and numerical simulations. With respect to constitutive equations (Chap. 3) the term deviatoric stress is also used for the tensor of deviatoric stress. Fig. 2.17 shows that the maximum stress q reached with the confined shortening test is in good accordance with the maximum stress reached with the unconfined shortening test with the same axial shortening rate (Fig. 2.15). Thus, it appears that the same shortening rate leads to the same maximum stress q that can be applied to a sample. However, with the unconfined sample the maximum stress has been reached at an axial shortening of 1% with a subsequent significant decrease (peak). With the same material, but confined, the maximum deviatoric stress is reached smoothly at an axial shortening of 14% at a kind of plateau. Continued shortening leads only to a slight decrease of the deviatoric stress. Thus, the material is still viscoplastic in the vicinity of a critical point. Fig. 2.18 shows a photo of the unloaded sample after the test. It reveals an almost cylindrical deformation of the sample. Only a small bulging of the surface has occured. The sample is free of shear localization even after an axial shortening of 16%. Thus, the material is viscoplastic within a large deformation range if the sample is sufficiently confined, and if it is deformed with sufficiently low deformation rates.

Fig. 2.19 shows a representative result of a confined shortening test with several stages of constant shortening velocities. The confining pressure has been kept constant at σ_{rad} = 10 MPa during the test. Table 2.4 gives an overview about the shortening rates at constant velocity stages. The test starts with an axial shortening rate of $\dot{\epsilon}$ = 1.4E-3 1/min (stage 1). The average deviatoric stress q in the sample increases disproportionally low with continued shortening due to the viscosity of the material. Sudden changes of the axial shortening rate have been carried out before a state limit was reached in order to investigate the argotropic behavior of the material. Nevertheless, a sudden increase or decrease of the actual shortening rate by one power of ten results in an increase or respectively a decrease of the average deviatoric stress after a transition (stages 2 and 4). It appears that sudden changes of the axial shortening rate back to the initial value (stages 3 and 5) lead approximately to the corresponding deviatoric stress that would have evolved if the shortening rate would have been kept constant.
A sudden decrease of the initial shortening rate by two powers of ten (stage 6) leads to a disproportionally low decrease of the deviatoric stress. It appears that the corresponding

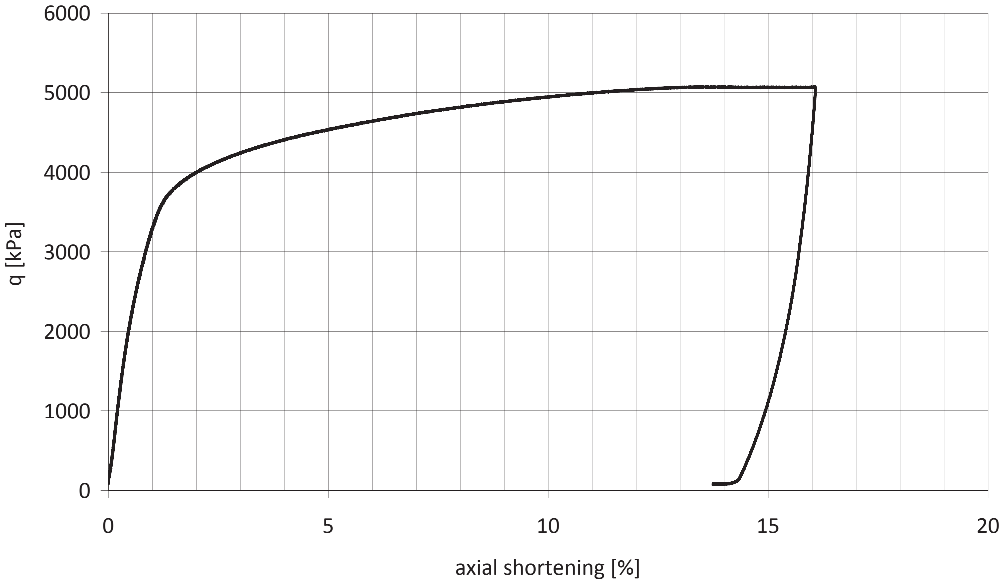

Figure 2.17: Viscoplastic behavior with a confined shortening test ($\sigma_{rad} = 5$ MPa) with a reconstituted bentonite sample, evolution of deviatoric stress q vs. axial shortening at constant shortening rate $d_{ax} = 1.4\text{E-}3$ 1/min

deviatoric stress that would have evolved with this shortening rate as constant from the beginning of the test is reached asymptotically from below. This indicates that the generation of micropores due to a previously higher shortening rate is reversible with sufficiently lower shortening rates if a critical point has not yet been reached. Thus, a decrease of the shortening rate provides the chance of a kind of self-healing of the material. The subsequent increase of the axial shortening velocity back to the initial one (stage 7) leads to an asymptotic approximation of the corresponding deviatoric stress from above. This indicates that new micropores are generated again due to the higher deformation rate. An additional increase of the initial shortening rate by two powers of ten (stage 8) leads to a disproportionally high decrease of the deviatoric stress, but still to a continued viscoplastic deformation of the sample. The test has been stopped at an axial shortening of 15%. This evolution of the deviatoric stress at alternating deformation rates reveals impressively the argotropic behaviour of geomaterials with soft particles.

Figure 2.18: Deformed reconstituted bentonite sample after a confined shortening test up to an axial shortening of 16%

Table 2.4: Confined shortening test with a reconstituted bentonite sample, shortening rates at constant velocity stages

stage	$\dot{\epsilon}$ [1/min]
1	1.4E-3
2	1.4E-2
3	1.4E-3
4	1.4E-4
5	1.4E-3
6	1.4E-5
7	1.4E-3
8	1.4E-1

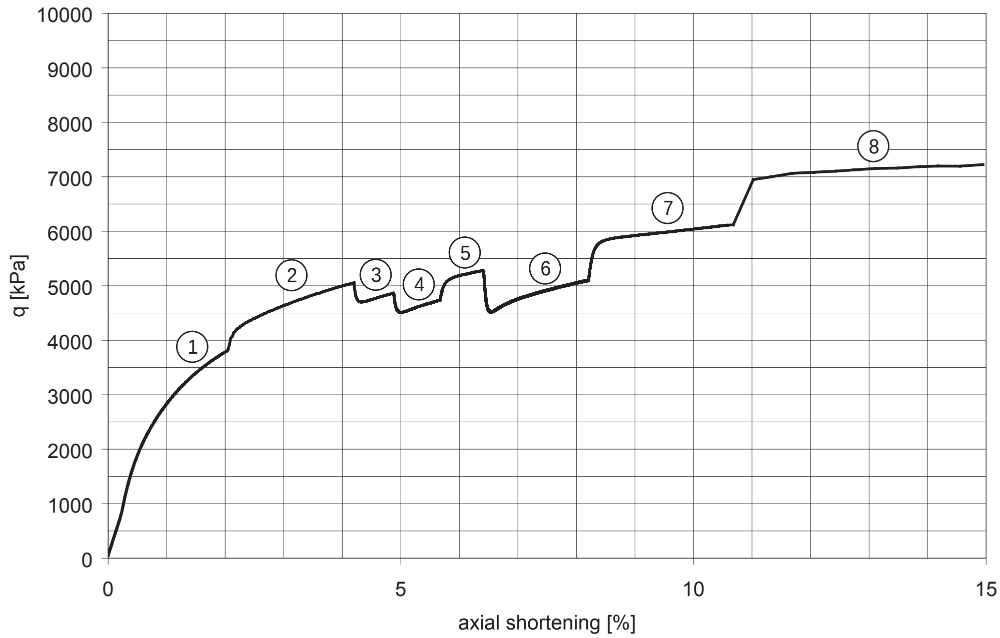

Figure 2.19: Argotropic behavior of a reconstituted bentonite sample with a confined shortening test ($\sigma_{rad} = 10$ MPa), evolution of deviatoric stress q vs. axial shortening at stages of constant shortening velocity according to Tab. 2.4

2.5 Tests with other reconstituted clay samples

2.5.1 Material

A claystone of the Keuper formation (Trias) from a pit at Zaisersweiher (near Karlsruhe, Germany) has been chosen in order to investigate the argotropic behavior of a reconstituted sample with natural minerals. The claystone has been cut from the ground surface by means of a hollow cylinder. A big hammer was required to drive the cylinder into the ground. The grain size distribution of the material revealed that the material contains approximately 25% of clay, 55% of silt and 30% of sand. The natural water content has been determined to be in the range of 15 - 16%. The average total content of carbonate minerals has been determined in the laboratory as 8.3%, from which 6.9% are calcite and 1.4% dolomite. According to results of an a X-ray diffractometer (XRD) analysis, which has been provided by the owner of the clay pit, the principal contents of phyllosilicate minerals are corrensite and illite. The fraction of quartz minerals is approximately 15%. Some solid particels of this material are harder than the clay minerals. Thus, the material provides predominantly viscoplastic (thermally activated), but also hypoplastic (seismically activated) deformations [13]. Purely seismic activation occurs with hard solid particles, then the redistribution of the local intergranular stresses is seismically induced. Thermally activated processes are negligable with hard solid particles. The particles can vary in size, e.g. quartz grains of a sand or fractured blocks of a rock mass.

2.5.2 Shortening tests with controlled axial deformation velocity

A confined shortening test was carried out in order to investigate the argotropic behavior of a reconstituted clayey sample. For this purpose, the sampled material had been milled in a mortar. Then the material was reconstituted with a maximum axial pressure of 20 MPa by means of the oedometric reconstitution device described above. The reconstituted sample had an initial height $h_0 = 67$ mm and an initial diameter $d_0 = 70$ mm, thus a height to diameter ratio of approximately one. The initial density of the reconstituted sample was $\rho_0 = 2.3$ g/cm^3.

Fig. 2.20 shows the result of the confined shortening test with several stages of constant shortening velocities according to Table 2.5. The confining pressure was kept constant at $\sigma_{rad} = 5$ MPa during the test.

The test starts with an axial shortening rate of $\dot{\epsilon} = 1.5\text{E-}4$ 1/min (stage 1). As observed with samples of paraffin or bentonite, the average deviatoric stress q in the sample increases disproportionally low with continued shortening due to a viscoplastic deformation of the material. The stress plateau at approx. $q = 3900$ kPa, which is reached with a smooth transition, indicates the proximity of a critical state. Subsequent sudden changes of the shortening rate by one tenth reveal the argotropy of the material (stages 2 to 6). Switching back of the shortening rate to the initial value leads to the corresponding deviatoric stress which could also be reached with a constant shortening rate. However, continued shortening leads to a slightly decreasing stress response even with reduced shortening rates after a critical point has been reached (stage 6). Self-healing of the material would require lower deformation rates. An increase of the confining pressure would enhance the self-healing.

The test has been stopped after an axial shortening of 7.3%. Fig. 2.21 shows the reconstituted clayey sample before (a) and after (b) the confined shortening test. The sample remained almost cylindrical. However, a critical state with shear localization was reached during this test and Fig. 2.21(b) reveals that the generation of new pores is aligned in helical shear bands.

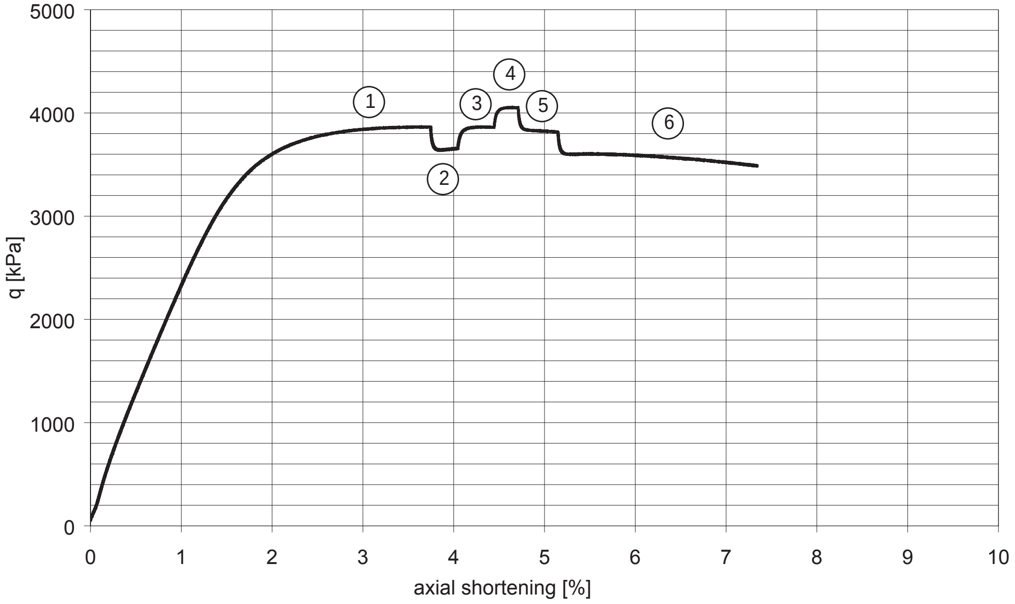

Figure 2.20: Argotropic behavior of a reconstituted clayey sample with a confined shortening test ($\sigma_{rad} = 10$ MPa), evolution of deviatoric stress q vs. axial shortening at stages of constant shortening velocity according to Tab. 2.5

Table 2.5: Confined shortening test with a reconstituted clayey sample, shortening rates at constant velocity stages

stage	$\dot{\epsilon}$ [1/min]
1	1.5E-4
2	1.5E-5
3	1.5E-4
4	1.5E-3
5	1.5E-4
6	1.5E-5

2.6 Tests with cored claystone samples

2.6.1 Material

The argotropic behavior of a natural claystone has been investigated with cored samples. The claystone samples were recovered from a depth of about 620 m from a Keuper formation which is part of the cap rock of an anticlinal structure at Ketzin (near Potsdam,

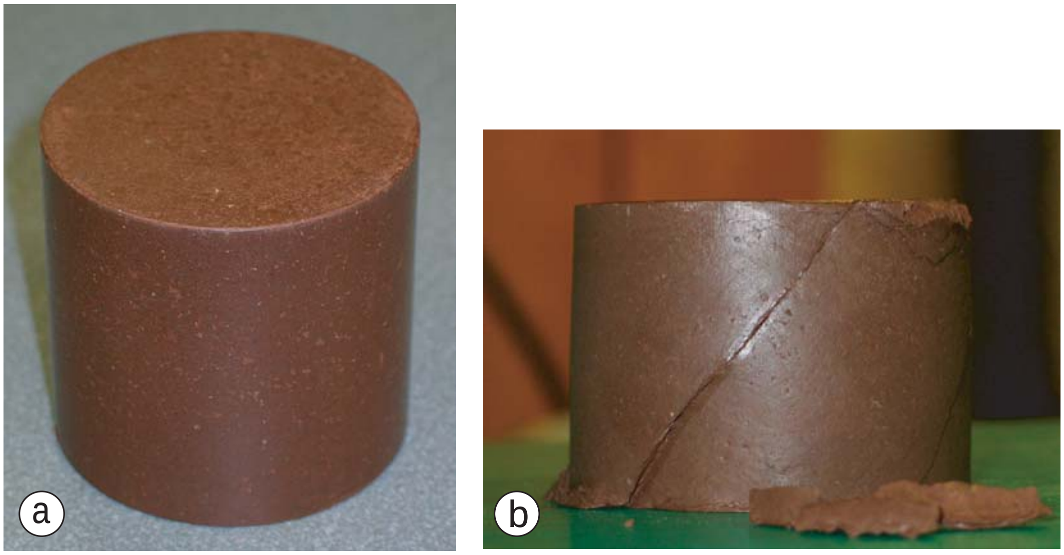

Figure 2.21: Reconstituted clayey sample before (a) and after (b) a confined shortening test with a helical shear band

Germany). The anticlinal uplift of the cap rock has been induced by diapirism.
Laboratory tests have been carried out with a representative sample in order to determine some characteristic values of the material. The natural water content was approximately 6.5%, and the specific weight of the solid particles was 28.4 kN/m^3. The specific weight of the sample at natural water content was 25.4 kN/m^3, and the specific weight of the dried material was 23.8 kN/m^3. Thus, the calculated void ratio of the sample was 0.19.
The mineral composition of the sample material has been determined by means of X-ray diffusion (XRD) at the Institute of Mineralogy and Geochemistry, University of Karlsruhe (now: KIT). The results of the XRD-analysis reveal a mineral content of 44% illite and 9% chlorite. The mass fraction of 53% of soft phyllosilicate minerals provides a considerable potential for thermally activated viscoplastic deformations. However, the quartz content has been determined to be 12%, and the mass fractions of dolomite and anhydrite are 32% in total. Thus, the mass fraction of 44% of hard solid particles provides also a potential for seismically activated deformations. Minor mass fractions of hematite (2%) and halite (1%) have been also determined with the XRD analysis.

The initial state of cored rock samples is disturbed due to drilling and stress relaxation. A short time isotropic compression at the onset of a confined shortening test does not provide physical and chemical conditions for a sufficient reversal of these disturbances. Furthermore, the macroscopic material composition of natural rock samples is often inhomogeneous due to its genesis. For example, the tested claystone had visible spherical inclusions of anhydrite (Fig. 2.23). As these inclusions do not vary significantly in space it appears that the material is homogeneous with respect to the size of the tested sample.

Nevertheless, the anhydrite inclusions provide inhomogeneities of the sample stiffness, and thus the stress is not uniformly distributed inside the sample. Thus, any externally uniform deformation of the sample induces a non-uniform stress field. This inhomogeneous stress field can lead to micropores, fractures and thus to clastic behavior. Therefore, results of shortening tests with cored rock samples are hardly reproducible. A statistically proven assessment of the material properties can often not be realized as this would require a too big number of tests. Thus, the following results of shortening tests can only show qualitatively some characteristics of the behavior of the tested material.

2.6.2 Shortening tests with controlled axial deformation velocity

Shortening tests with control of the axial deformation velocity have been carried out with cored claystone samples. Fig. 2.22 shows the evolution of the average axial stress vs. the axial shortening of a cored claystone sample with an unconfined shortening test. The initial height and diameter of the sample were 50 mm. The test was performed at a constant shortening velocity which corresponds to an initial axial shortening rate of 1.0E-4 1/min. The disproportionally high increase of the axial stress up to a shortening of 0.3% may indicate an imperfect plane-parallelity of the upper and lower surfaces. However, the material was disturbed due to drilling, transport and subsequent sample preparation. Thus, the closure of pores which were induced by the sampling would also lead to an initial incease of the incremental stiffness of the material. The subsequent increase of the axial stress is nearly linear up to a critical state. The maximum stress is reached with an axial shortening of 0.73%. The marked peak of the axial stress at a critical point is accompanied by a marked acoustic emission. The proximity of a critical state is not predictable only from the evolution of stress-shortening behaviour. The subsequent clastic behaviour leads to a significant decrease of the average axial stress in the sample. The test was stopped after a shortening of 0.85%. Fig. 2.23 shows the sample with strain gauges before (a) and after (b) the test. Fig. 2.23(b) reveals an axial splitting of the sample. It appears that the thermally activated viscosity of this material is of minor relevance for unconfined conditions.

A radial support of the sample by means of a confining pressure enhances the ductility of the material, which results in an extended range of viscoplastic behavior. Fig. 2.24 shows the evolution of the deviatoric stress q vs. axial shortening of a cored claystone sample with a confined shortening test. The initial height and diameter of the sample were 36 mm. The test was carried out with a confining pressure $\sigma_{rad} = 10$ MPa and with a constant shortening velocity. The shortening rate was 2.8E-5 1/min. The result of the

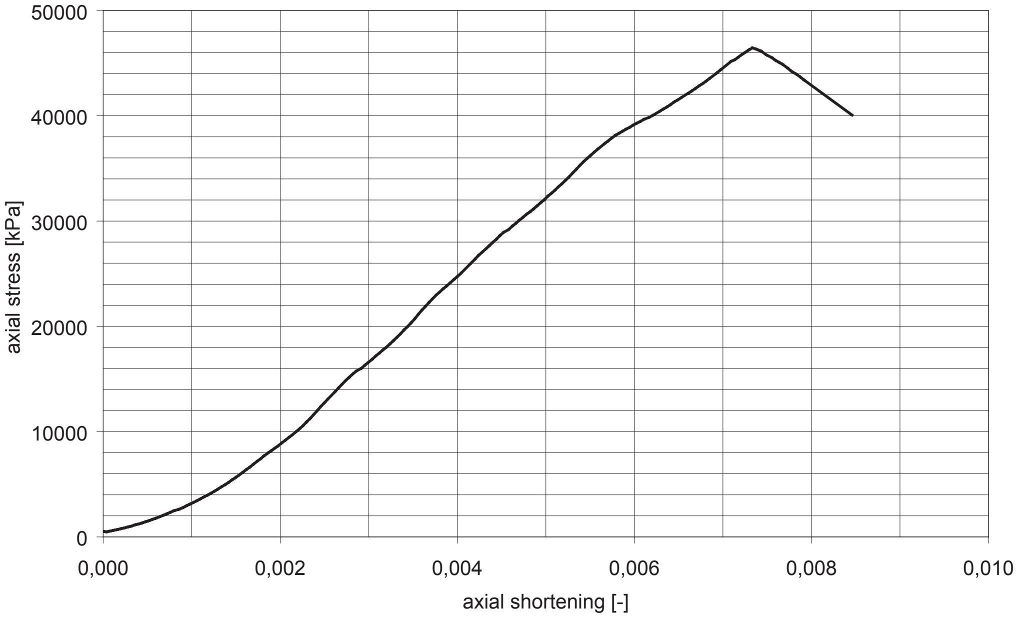

Figure 2.22: Unconfined shortening test with a cored claystone sample, evolution of axial stress vs. axial shortening at constant shortening rate d_{ax} = 1.4E-4 1/min

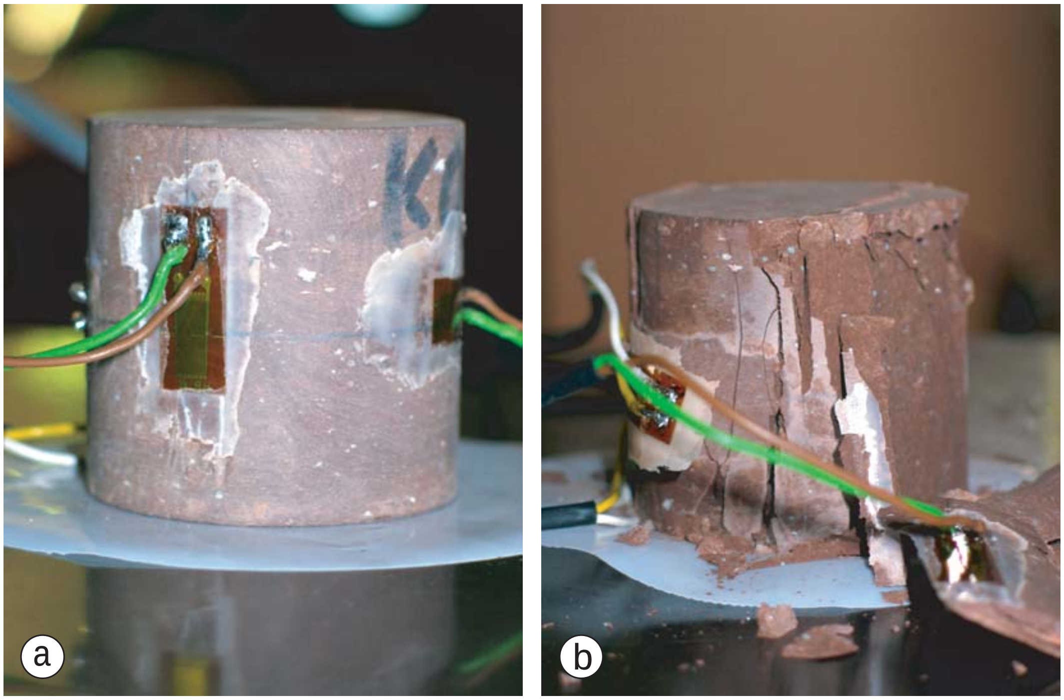

Figure 2.23: Cored claystone sample with strain gauges before (a) and after (b) an unconfined shortening test with axial splitting

test reveals a rather plastic behavior of the material with confined conditions. A critical state was reached with a smooth transition. The test was stopped at a maximum stress after a shortening of 1.9%.

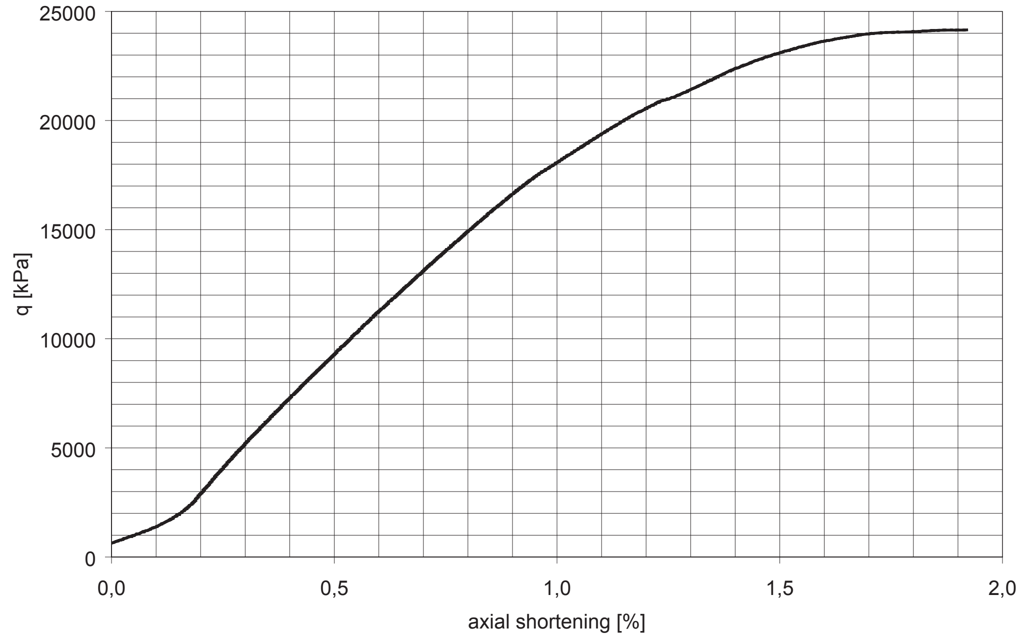

Figure 2.24: Behavior with an confined shortening test with a cored claystone sample, evolution of deviatoric stress q vs. axial shortening at constant shortening rate d_{ax} = 2.8E-5 1/min

The argotropic behavior of the cored claystone was investigated with confined shortening tests with temporarily constant shortening velocities. Fig. 2.25 shows the evolution of the deviatoric stress q vs. the axial shortening of a test with stages according to Tab. 2.6. The test was performed with a confining pressure $\sigma_{rad} = 10$ MPa. The initial height and diameter of the sample were 36 mm. The test started with a shortening rate of d_{ax} = 2.8E-5 1/min (stages 1 and 3), an increase of the shortening rate leads to an increase of the deviatoric stress (stage 4). A decrease of the shortening rate back to the initial value leads to a deviatoric stress which would also have evolved with continued constant shortening with the initial rate (stage 5). Stages with temporarily constant deviatoric stress have been included in this test (stages 2 and 6) in order to investigate the deviatoric creep behavior of the material. A maximum deviatoric stress was reached with smooth transition with the initial shortening rate (stage 7) at an axial shortening of 2.3%. Continued shortening of the sample leads to a marked decrease of the average deviatoric stress in the sample. The test was stopped at an axial shortening of 2.5%. Fig. 2.26 shows the deformed sample after the test. Shear localization has evolved rather erratically due to local inhomogenities.

The test result reveals the argotropy of the tested claystone. Furthermore, the increase of the deviatoric stress with the initial shortening rate after a creep stage (onset of stages 3 and 7) is significantly higher than before the creep stage (end of stages 1 and 5). Fig. 2.27 shows the evolution of the axial shortening vs. time during the creep stages 2 and 6 at constant deviatoric stress $q_2 = 9740$ kPa (a) and $q_6 = 18240$ kPa (b). The increase of the average stress with fixed increments is due to the force control of the testing device. The inclinations of the curves (dashed lines) indicate the shortening rates at various times and stresses ((1),(2), (3)). At the end of stage 2 (a) the creep rate is $\dot{\varepsilon}_1 = 2\text{E-}7$ 1/min (1). With a higher deviatoric stress (b), but after the same creep period, the creep rate is $\dot{\varepsilon}_2 = 5\text{E-}7$ 1/min (2). However, continued creep leads to a creep rate of $\dot{\varepsilon}_3 = 2\text{E-}7$ 1/min at the end of this creep stage (3). The creep rates at the end of both creep stages are $\dot{\varepsilon} = 2\text{E-}7$ 1/min, and thus two orders of magnitude lower than the shortening rates $d_{ax} = 2.8\text{E-}5$ 1/min of the previous and subsequent testing stages. Additional pores that were generated with the higher shortening rate d vanish in parts with low deformation rates during the creep stages. The increase of the deviatoric stress with the initial shortening rate after a creep stage indicates that a self-healing of the material was enabled with the low deformation rates during the creep stages.

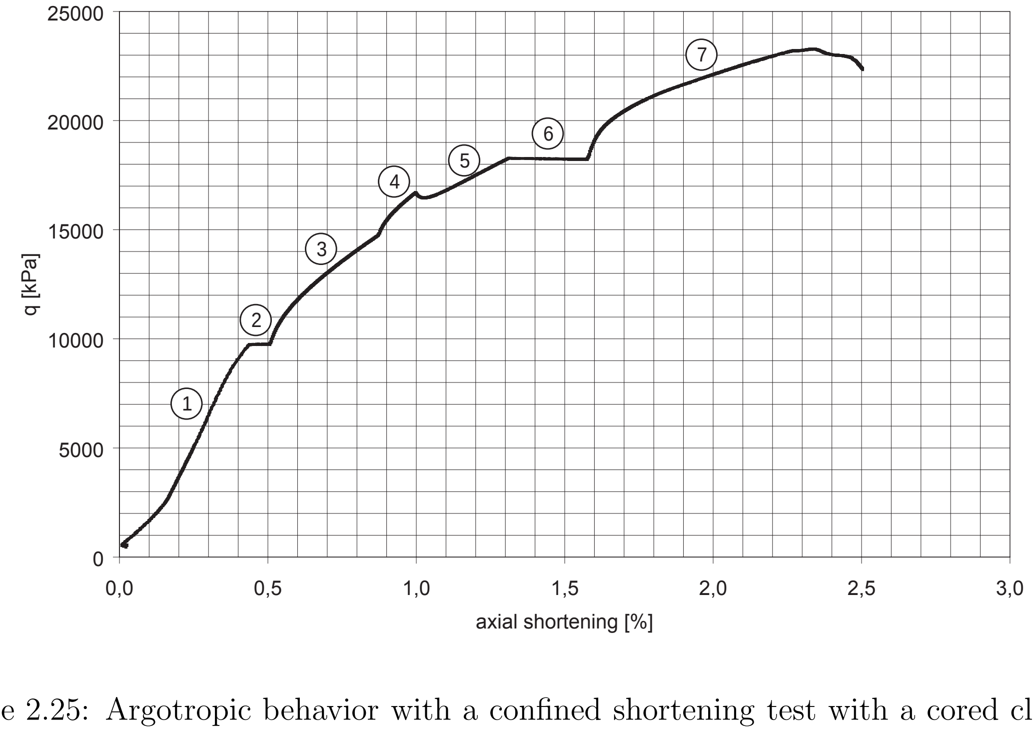

Figure 2.25: Argotropic behavior with a confined shortening test with a cored claystone sample, deviatoric stress q stress vs. axial shortening

Table 2.6: Confined shortening test with a cored claystone sample, shortening rates at constant velocity stages

stage	$\dot{\epsilon}$ [1/min]
1	2.8E-5
2	creep stage
3	2.8E-5
4	2.8E-4
5	2.8E-5
6	creep stage
7	2.8E-5

2.7 Conclusions

The material properties of selected samples that have been observed with laboratory tests are essentially in accordance with the assumptions that have been made for keroids:

- paraffin reveals a markedly nonlinear viscosity like rock salt or ice; rate-dependence, creep and relaxation are as defined for keroids; the range of validity is limited by upper bounds of deformation rates due to shear localization and cracking;
- reconstituted samples are a suitable substitute for naturally remolded material of clay smears, e.g. in a cap rock due to extensive deformations;
- reconstituted (artificially sintered) samples of a bentonite and of a natural clay with consolidation pressures of 20 - 150 MPa exhibit likewise rate-dependence and an upper bound of stretching rate by shear localization and fracture;
- these features are also observed with natural mudstone samples, but for lack of uniformity before and during the experiments the identification of material properties is less precise;
- critical points near stationary states are indicated by a peak in a stress-deformation plot; a peak is only critical with a sufficiently high magnitude of deformation rate

Small deformations appear to be completely reversible if they are applied rapidly, but even then there is some time-dependence. Continued slow deformation arises due to viscosity. Viscoplastic deformations in solids with soft particles are due to thermally

Figure 2.26: Cored claystone sample with irregular fractures after clastic behavior during a confined shortening test

activated changes of the positions of pre-existing dislocations in the material, which can be explained by the rate process theory as will be shown in the sequel chapter. Thus, one may say that *plasticity is a kind of nonlinear viscosity and thermally activated*.

One-dimensional considerations (average axial stress vs. axial shortening) suggest that the ability of a material to perform stationary viscoplastic deformations at constant stress can be defined as ductility. In the ductile regime new nano- or micropores are induced by shearing at some places while pre-existing pores vanish at other places. There is no net change in the number of micropores within a given time. So even though inducing new micropores the reversibility of this process provides a kind of self-healing. The re-

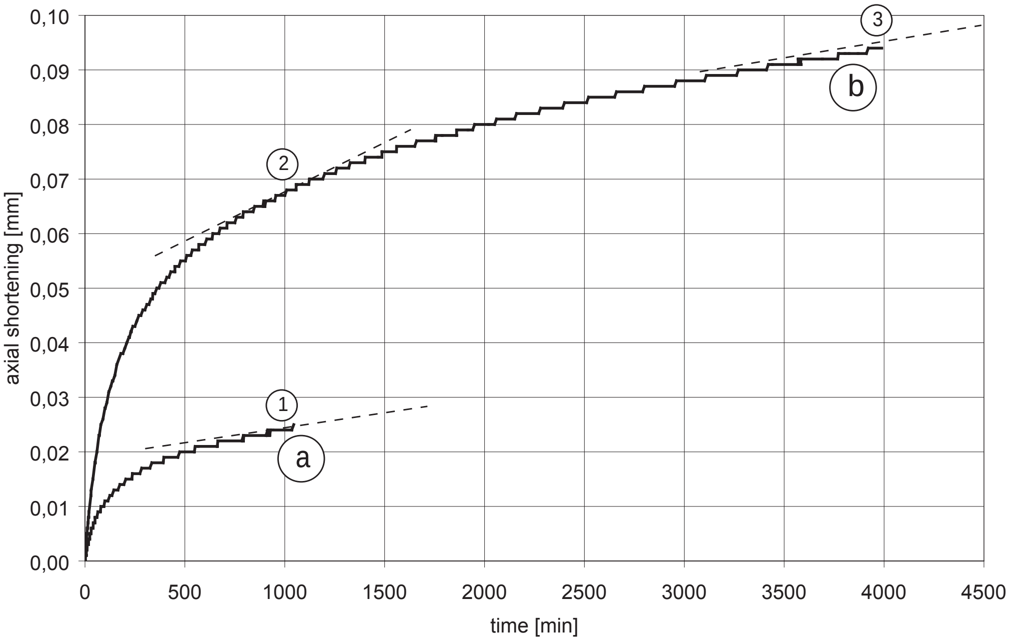

Figure 2.27: Creep stages with constant deviatoric stress $q = 9740$ kPa (a) and $q = 18240$ kPa (b) during a confined shortening test with a cored claystone sample; evolution of the axial shortening vs. time

lated viscoplastic deformations occur at temperatures below the melting point. As energy is locally dissipated in this process, a sufficient heat conduction is required to avoid a substantial rise of temperature. Otherwise, fast deformation results in self-heating and weakening of the material.

Viscoplastic deformation is possible at low shortening rates up to a maximum value (critical shortening rate) which characterizes the boundary of the ductile regime. At this shortening rate more micropores are produced than vanish in the same time. Thus, the micropores can evolve to macropores which can aggregate to flat pores (fractures). Continued shortening with the critical shortening rate (or even higher) results in a sudden decrease of average stress, then one can observe shear localization and fractures. The maximum stress at the critical shortening rate characterizes a critical point of the material with a transition from viscoplastic to clastic behavior.

A critical point is reached first at inhomogeneities of a sample (e.g. points of locally concentrated stress). Localization of the deformation to shear bands can start and evolve from these points.

Deformation rates much higher than with shear banding result in axial splitting. The elastic energy is consumed by creating new surfaces and by radiation of acoustic waves. Thus, axial splitting is accompanied by acoustic emission. This can be heard in a quiet environment. Thus, the in-situ monitoring of seismicity is indispensable for maintaining rock in a subcritical state.

These conclusions are limited to monotonous evolutions, cyclic deformations and ratcheting have not been considered in this thesis.

Chapter 3

Constitutive approaches

3.1 Motivation and overview

Glass can be considered as a very hard and brittle substance at room temperature. The material breaks if it gets deformed rapidly. However, if a rod of glass is stressed only by its own weight when laying it horizontally across two supports it will, within a few years at room temperature, show a distinct sag [2]. A cantilever beam of lead, tin or paraffin (e.g. a candle) shows a visible creep deformation at room temperature already within a few days. The creep behavior of these solids depends on the deviatoric stress and the temperature of the material. The creep rate can be increased or reduced by increasing or respectively reducing the stress and / or the temperature. It appears that at a higher temperature the same creep rate can be reached with a lower deviatoric stress, and that an increase of temperature leads to a higher creep rate at constant deviatoric stress.
Any reduction of the deformation rate to zero (e.g. by keeping the shape of a sample constant) leads to a decreasing evolution of deviatoric stress, i.e. relaxation. It appears that without internal dry friction the deviatoric stress relaxes asymptotically to zero. Relaxation can also be enhanced by increasing the temperature.
Shortening tests with stages of temporarily constant shortening velocities (Chap. 2) reveal an argotropic behavior of keroid (i.e. wax-like) materials. The argotropic behavior can be enhanced by increasing the temperature. However, as energy is dissipated with an inelastic deformation a sufficient heat conduction is required to avoid a substantial rise of temperature. Otherwise fast deformation results in self-heating and weakening of the material.

Nonlinear viscoplastic behavior of solids (i.e. argotropy, creep and relaxation) has been observed with a variety of materials. It has been investigated and described by several authors. In order to quantify the observed nonlinear viscous effects, a variety of tests and constitutive approaches have been made. Some of them are presented in the sequel.

A tensorial formulation of a viscoplastic constitutive relation, which is suitable to describe the nonlinear viscoplastic behavior of keroids in the ductile regime within a wide range of deformation rates, is explained. The presented constitutive relation is compatible with the rate process theory, thus the influence of temperature on the viscoplastic material behavior of keroids can be taken into account. Material parameters for a viscoplastic constitutive relation were determined with the results of the laboratory tests presented in Chap. 2 for subsequent use with numerical calculations.

Numerical simulations of laboratory tests were carried out with suitable boundary conditions by means of the finite-element-method (FEM). The results of the laboratory tests are compared with the results of numerical simulations of these tests. The limits of application of the constitutive relation with numerical calculations are outlined for further applications to boundary problems. The numerical model is applicable to processes without volume change up to a steady state, but not further.

3.2 Experimental findings and constitutive approaches

3.2.1 Creep of steel at high temperatures

Steel above red heat reveals time-dependent yielding characteristics which have little in common with those at room temperature. Steel reveals a marked nonlinear viscous behavior at high temperatures. Norton [2] performed tensile creep tests at constant loads and temperatures with bars of different qualities of nickel-chrome-silicon-steel. The tests were carried out with tensile stresses between 1.3 and 207 MPa, and the temperature ranged from 538 to 816 °C. Norton noticed that a constant creep rate, which was measured with a constant tensile stress at a constant temperature, could also be attained with a lower stress at a higher temperature or with a higher stress at a lower temperature. From the results of his tests, Norton suggested an empirical one-dimensional relationship which is known as *Norton's law*,

$$\dot{\epsilon} = m \cdot \sigma^n \tag{3.1}$$

with two material constants m and n. m, which he calls unit flow rate, is a reference deformation rate at a reference stress. Nortons test results show that the power n ranges from 3 to 17 with an average of 5 for the tested steel qualities. This range reveals that the relationship between stress and deformation rate is markedly nonlinear. Thus, the creep rate rises up disproportionally high with a small increase of the stress. The viscoplastic deformation of steel (in the literature often named *plastic flow*) can be attributed to slippage at the grain boundaries, deformation of the crystallites or both [15], [17]. Norton's law (3.1) is evidently not unit-invariant and not directly applicable to two- or three-dimensional problems.

It is difficult to measure precisely viscoplastic deformations of steel at high temperatures with low stresses. Thus, it is not known whether there exists a stress and temperature below which no viscous deformation occurs. It is possible, and probable with the arguments discussed later in this chapter, that steel creeps even at room temperature. As yet one can only state that at a certain stress, the rate of deformation is below a certain value. Thus, it appears that the frequently used term *limiting creep stress* is rather arbitrary. It is not sure that such a threshold value exists [2]. Norton's approach to quantify observations from testing of steel at high temperatures refutes such a threshold.

3.2.2 Tensile tests with cast iron

The nonlinear viscous behavior of cast iron was explained with thermal activation by Prandtl [1]. When analyzing results of tensile tests with rods of cast iron, Prandtl found that deformations due to the applied stresses include a non-reversible part, the magnitude of which reveals a significant time-dependence. He proposed an empirical relationship between changes of stretching velocities and changes of stresses, viz.

$$\Delta\sigma \sim \ln \dot{\epsilon}. \tag{3.2}$$

Prandtl explains time-dependent deformations by means of thermal oscillations in a solid body. He assumed that the amplitudes of these oscillations are not constant and that deviations from an average amplitude are randomly distributed. Thus, few oscillations may occur with amplitudes which suffice to translate a solid particle from a stable regime across an unstable position to an adjacent stable regime. Prandtl noticed that the probability of such translations increases with an increasing temperature of a solid. This is a precursor of the *rate process theory*, which is outlined in Sec. 3.2.4.

Prandtl suggested an exponential relationship between the rate of displacements and an activation energy. The original formulation of his one-dimensional constitutive approach for the change of resulting forces with a change of deformation velocities between two states of stationary creep reads

$$P_1 - P_2 = c \cdot \log \frac{v_1}{v_2} \tag{3.3}$$

with resulting forces P_i, the deformation velocities v_i, and a material constant c. (3.3) also can be written with stresses instead of resulting forces as

$$\sigma = \sigma_r \left[1 + c_1 \cdot \ln \frac{\dot{\epsilon}}{c_2} \right] \tag{3.4}$$

with an initial reference stress σ_r and the material constants c_1 and c_2. Both constants are proportional to $k_B T/E_a$ with the absolute temperature T, the activation energy E_a and Boltzmann's constant k_B. Equation (3.4) fails for $\dot{\epsilon} \rightarrow 0$ as $\sigma \rightarrow -\infty$ makes no sense.

3.2.3 Shearing resistance of clayey soils

Leinenkugel [3] investigated the shearing resistance of clayey soils and explained his results with the rate process theory. Undrained laboratory tests with saturated clay samples (Fig. 3.1) show that a sudden increase or decrease of the deformation rate $\dot{\epsilon}_\alpha$ to $\dot{\epsilon}$ induces an increase or decrease of the shearing resistance $\tau_\alpha = (\sigma_1 - \sigma_3)/2$ by the amount $\Delta\tau = \tau - \tau_\alpha$ [3]. Leinenkugel found Prandtls approach to be in good accordance with his results [4], which can be approximated by

$$\Delta\tau = I_{v\alpha} c_{u\alpha} \cdot \ln \frac{\dot{\epsilon}}{\dot{\epsilon}_\alpha}. \tag{3.5}$$

Therein the dimensionless material constant $I_{v\alpha}$ is called *viscosity index*. $I_{v\alpha}$ is independent of the effective mean pressure p' and the void ratio e, but $I_{v\alpha}$ is only valid for an assumed reference deformation rate $\dot{\epsilon}_\alpha$. With this approach it is possible to estimate velocities and resulting forces for a variety of geotechnical applications, such as the velocity distribution of creeping slopes or the lateral flow pressure against piles [4].

3.2.4 Rate process theory

Inelastic deformations of solids require rearrangements of matter. One approach to study this phenomena is the theory of absolute reaction rates [5] which is also called *rate process theory*. This theory provides a deeper understanding of material strength and functional forms for stress-deformation relationships of solids.

Depending on the structure of a solid, viscoplastic rearrangements can evolve with atoms,

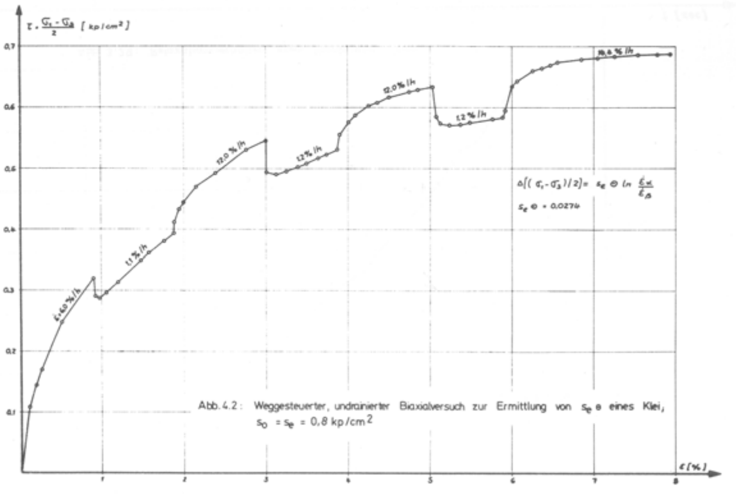

Figure 3.1: Deformation-controlled undrained biaxial test with clay with temporarily constant axial deformation rates, from [3]

molecules or groups of molecules which are so-called *dislocation units*. Dislocation units are restrained from relative movement past each other by *energy barriers* that separate adjacent equilibrium positions. A dislocation of a unit to an adjacent equilibrium position requires an *activation energy* E_a to pass the separating energy barrier (Fig. 3.2). In general, the energy potential of a unit at an adjacent equilibrium position can be the same (i.e. no drift), higher or lower (i.e. drift) than it was initially [7]. The magnitude of the activation energy depends on the material.

For a material at rest (i.e. without drift) and at constant temperature, the required activation energy to enable a dislocation unit to pass an energy barrier can be due to thermal energy (i.e. erratic oscillations with sometimes higher amplitude). The thermal energy is Boltzmann-distributed. The average thermal energy per dislocation unit is $k_B T$, and the average frequency ν_0 of thermal oscillations is

$$\nu_0 = \frac{k_B T}{\hbar} \tag{3.6}$$

with the absolute temperature T, Boltzmann's constant k_B=1.38E-23 J/K and Planck's constant $\hbar$=6.624E-34 Js.

The probability of a state with an energy E is proportional to $\exp(-E/k_B T)$ for a thermodynamic equilibrium. Thus, the probability p of a dislocation unit to get activated, i.e. the average fraction of flow units getting activated during one oscillation, is exponential, which expresses maximum disorder (entropy):

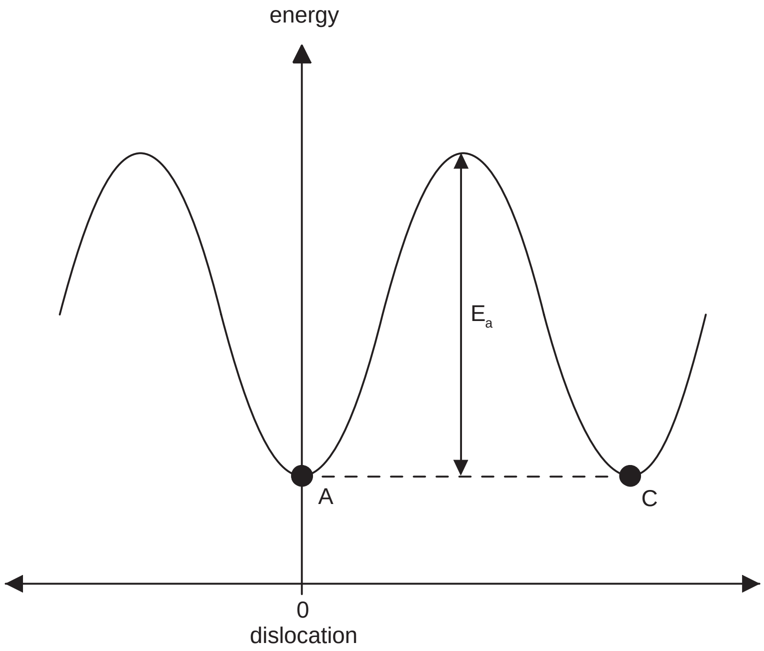

Figure 3.2: Thermal activation without drift with adjacent equilibrium positions A and C

$$p = a \exp \frac{-E_a}{k_B T} \tag{3.7}$$

with an activation energy E_a and a factor a. Thus, the activation frequency is

$$\nu = p\nu_0, \tag{3.8}$$

and with (3.6) and (3.7)

$$\nu = \frac{k_B T}{\hbar} \exp \frac{-E_a}{k_B T}. \tag{3.9}$$

At zero temperature there is no thermal oscillation of matter. At equilibrium there is no damping, i.e. no average thermal radiation. Without a drift (i.e. gradient of potential energy) the activation frequency depends only on the material constant E_a and the absolute temperature T. Energy barriers can then be passed in all directions with the same frequency ν. Except for critical points, the effect of thermal activation of a solid at equilibrium can be observed only at a sufficiently high temperature as a change of the state of aggregation (i.e. melting).

Equation (3.9) provides a relationship between the activation energy E_a and the average activation frequency ν for an absolute temperature T. The determination of E_a requires a proper definition of a dislocation unit. A nano-size approach for the determination of the activation energy is outlined in 3.2.5.

The potential energy of a dislocation-unit can have a gradient or a *drift*, e.g. due to a shear force (Fig.3.3). A shear force ΔF distorts the minima of the energy by an amount δ from the drift-free state. This distortion implies an elastic deformation of the material. For simplicity this representation holds for the spatial direction with maximum gradient or drift. The distance between subsequent equilibrium positions may be called λ. A shear force ΔF that acts on a dislocation-unit in one direction reduces the barrier height by an amount $\Delta F\lambda/2$ in the same direction, and increases the barrier height by the same amount in the opposite direction. The reduction of the potential energy may be understood as the work of the force ΔF when shifting a dislocation unit to lower equilibrium positions. In the case of a dislocation it is released as heat. Thus, a sufficient thermal conductivity of the material is required to prevent self-heating.
The reduction of the height of an energy barrier in the direction of the drift increases the number of passages downwards, and the average activation frequency ν in this direction increases to

$$\nu_{inc} = \frac{k_B T}{\hbar} \exp \frac{-E_a - \Delta F\lambda/2}{k_B T}. \tag{3.10}$$

In the opposite direction, the drift reduces the number of passages upwards, and the activation frequency ν in this direction decreases to

$$\nu_{red} = \frac{k_B T}{\hbar} \exp \frac{-E_a + \Delta F\lambda/2}{k_B T}. \tag{3.11}$$

Thus, the resulting net activation frequency in the direction of the drift is

$$\nu = \nu_{inc} - \nu_{red} = 2\frac{k_B T}{\hbar} \exp \frac{-E_a}{k_B T} \sinh\left(\frac{\Delta F\lambda}{2k_B T}\right). \tag{3.12}$$

At any time, some of the activated flow units pass energy barriers upwards while others fall back to their previous positions. Each dislocation unit which passes a barrier undergoes a displacement λ. The average frequency of passages ν is proportional to the rate of anelastic displacement $\dot{\epsilon}$, i.e. $\nu \sim \dot{\epsilon}$. Thus, for a number of n passages which are required for a unit displacement $L_0 = n \cdot \lambda$, with (3.12) the rate of anelastic displacement $\dot{\epsilon}$ is

$$\dot{\epsilon} = 2n\frac{k_B T}{\hbar} \exp \frac{-E_a}{k_B T} \sinh\left(\frac{\Delta F\lambda}{2k_B T}\right). \tag{3.13}$$

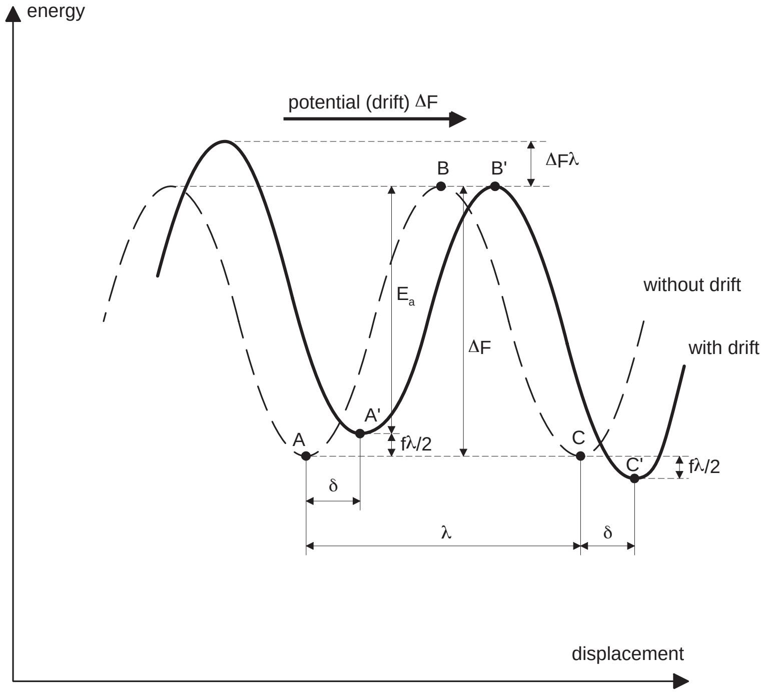

Figure 3.3: Activation energy with gradient of potential energy (drift), after [7]

Equation (3.13) describes the one-dimensional relationship between $\dot{\epsilon}$ and ΔF for so-called *Eyring fluids*.

For high drifts, i.e. $\Delta F > (2/\lambda) \cdot k_B T$, the upward passages can be neglected as $\sinh(x) \approx (1/2)e^x$ for any $x > 1$, and (3.13) can be replaced by

$$\dot{\epsilon} \approx n \frac{k_B T}{\hbar} \exp\left(-\frac{E_a - \Delta F \lambda}{k_B T}\right). \tag{3.14}$$

The one-dimensional relationship equation (3.14) is suitable for a variety of deformation processes of solids, except for so small shear (drift) that the exponential approximation of the hyperbolic sine is not justified [7].

For low drifts, i.e. $\Delta F < (2/\lambda) \cdot k_B T$ $\sinh(x) \approx x$ with $0 < x < 1$, and (3.13) can be replaced by

$$\dot{\epsilon} \approx \Delta F \frac{n\lambda}{\hbar} \exp\left(-\frac{E_a}{k_B T}\right). \tag{3.15}$$

Thus, the deformation rate is proportional to the drift for a low drift at constant temperature. Equation (3.15) describes the one-dimensional relationship between $\dot{\epsilon}$ and ΔF for so-called *Newtonian fluids* with linear viscosity.

Introducing an activation energy E_a^* which includes a drift

$$E_a^* = E_a - \frac{\Delta F \lambda}{2}, \tag{3.16}$$

and with the assumption $nk_BT/\hbar = \text{const.}$, (3.14) can be written for stationary conditions as

$$\dot{\epsilon} = A \exp \frac{-E_a^*}{k_B T}. \tag{3.17}$$

(3.17) is known as an equation proposed empirically by Arrhenius [10] in 1889 for the temperature-dependence of chemical reaction rates.

3.2.5 Persson's approach

Based on condensed matter physics, Persson [8] derived a theory for the viscoplastic deformation of glassy solids. This theory can also be applied to polymers as e.g. paraffin, plastics or rubber [9]. Persson [8] derived equation (3.4) with an approach which regards dislocation units as so-called nano-sized stress-blocks. Viscoplastic deformations are considered as slidings by dislocations which move short distances before they get pinned at crystal imperfections (e.g. other dislocations or material impurities).

It has been found experimentally that viscoplastic deformations, creep and relaxation of pore-free solids depend only on the deviatoric stress, but not on the mean pressure, and that the volume remains constant. The activation energy of nano-sized blocks with a length d_{nano} and a shear modulus G_{nano} can be estimated with the application of a critical shear stress to a block, viz. the cohesion c_{nano}. With $E_a \approx c_{nano} d_{nano}^3$ and with the density ρ of the oscillating mass, the activation frequency is $\nu_0 \approx (G_{nano}/\rho)^{0.5}/d_{nano}$. The derivation of the dependency of the deviatoric stress on the logarithm of the deformation rate does not require an internal variable, this can be found more detailed in [8]. Persson's approach specifies the dislocation unit for solids and provides realistic activation energies and bounds for a validity-range of deformation rates [8].

Solids cannot be free of stress due to boundary-stresses and temperature fields which they have been exposed to in earlier times, even at their natural genesis or artificial production. Persson assumes that yield processes involve only nano-sized stress-blocks with characteristic lengths of $\approx$ 10-100 $\mathring{A}$. Because the term *stress* is no more reasonable in a physical sense when decreasing the length scale to nano-size, i.e. molecular or even atomic dimensions, only a *mean value of stress* can be considered. This mean value of stress vanishes if

a solid body is not exposed to an (external) boundary stress, whereas the internal stress distribution of the solid body varies in space. Due to *fluctuating eigenstresses*, some dislocation units require a lower activation energy for slippage than others. Memory effects could be considered with a function of the distribution of inherent eigenstresses.
Relaxation reduces eigenstresses. Thermal oscillations of matter occur at any higher than zero temperature, so stress-relaxation is enabled. With increasing temperature, the activation frequency increases and stress relaxation runs faster. Thus, it is possible to enhance the reduction of internal stresses by increasing the temperature. The enhancement of stress-relaxation with heat is known for metals as relieving stress by annealing. The yield stress of metals (in terms of plasticity theory) can thus be modified by thermal treatment. However, with Persson's theory, it appears that even at a low (but non-zero) temperature the yield stress is not constant with respect to time.

3.2.6 Comparison of different approaches

With $c_2 = \dot{\epsilon_\alpha}$, $\sigma = \tau$, $\sigma_r = c_{u\alpha}$ and $c_1 = I_{v\alpha}$ equations (3.4) and (3.5) are identical, so Leinenkugel's approach corresponds with Prandtl's. Both equations can be derived by means of the rate process theory with the approximation of equation (3.14) for solids. Comparison with (3.5) yields $I_v \sim k_B T/E_a$, and the activation energy can be estimated with Persson's approach [8] in a range from $E_a \approx 0.5$ eV per stress-block for clay minerals to $E_a \approx 3$ eV for per stress-block quartz (1 eV $\approx 40\ k_B T$).
Leinenkugel's logarithmic equation (3.5) and Norton's power law (3.1) agree fairly well: with $x = \dot{\epsilon}/\dot{\epsilon}_r$

$$1 + I_v \cdot ln\,(x) \approx (x)^{I_v} \tag{3.18}$$

holds, with $\Delta\tau = \tau - c_{u\alpha}$ in (3.5), for $10^{-3} < x < 10^{-3}$ and $0.01 < I_v < 0.15$. For $\sigma/\sigma_r = 1$ the conversion of Leinenkugel's parameters to Norton's can be written with (3.18) as

$$n = \frac{1}{I_v}. \tag{3.19}$$

Thus, equation (3.5) can be approximated by a power law so that

$$\tau = c_{u\alpha} \left(\frac{\dot{\epsilon}}{\dot{\epsilon}_r} \right)^{1/n}. \tag{3.20}$$

The approximation by the power law in (3.18) gets more precise with smaller deviations of σ from σ_r, or likewise with a smaller deviation of deformation rate from the reference value. The approximation (3.18) gets also more precise with decreasing I_v. Equation (3.5) fails for a reduction of the deformation rate from the reference value by several orders of magnitude as the stress ratio σ/σ_r gets negative. Thus, keeping in mind the range of validity, Norton's power law may be considered as a fairly good one-dimensional constitutive approximation for nonlinear viscosity.

3.3 A constitutive relation for the viscoplastic behavior of keroids

3.3.1 Requirements and assumptions

Numerical simulations of element tests and a complete formulation of boundary value problems require constitutive relations. These have to suffice several criteria of objectivity. Deviatoric tensorial formulations are apt for arbitrary isochoric deformations and frame-indifference. Furthermore, constitutive relations have to be unit-invariant and independent of unknown initial variables.

Elastoplastic constitutive equations split up total strains into elastic and inelastic parts when a yield criterion is reached. Thus, they require the definition of a yield surface in the stress space. Usually, it is assumed that plastic yielding occurs without respect to time. With the results of laboratory tests, which have been outlined in Chap. 2, and with the experimental findings and constitutive approaches which have been outlined in Sec. 3.2 of this chapter, it appears that viscous deformations can be induced even with small deviatoric stresses. As outlined in Sec. 3.2, a power law according to Equation (3.20) is a suitable approximation for nonlinear viscosity.

The constitutive equations presented in the sequel include a tensorial formulation of a power law which provides viscous (i.e. inelastic) deformations from the very beginning. An explicit definition of a yield surface and a flow rule is dispensable, and limit states are reached with smooth transitions. Mathematical functions for switches between loading and unloading are not required. The inclusion of elasticity provides relaxation. Thus, in contrast to conventional elastoplastic constitutive models (e.g. so-called Mises, Tresca or Mohr-Coulomb models), the subsequent constitutive equations are capable to describe the relations between stresses and deformations of keroids as they provide argotropy, creep and relaxation. The assumptions for the material, which have been outlined in the previous chapter, are also adequate for this one.

Material constants which include the dimensions of stress and time provide unit-invariance. They can be principally calculated by means of the rate-process theory. The dimension of stress can be included with an activation energy per mol or unit volume, and the dimension of time can be included with a reference to an activation frequency. Persson [8] found that the relation between deviatoric stresses and deformation rates does not require internal variables. Thus, the fabric of a keroid is determined only by stress.

3.3.2 Deviatoric tensorial formulations

Frame-indifference requires the use of tensors in constitutive equations. The following tensors may be used for an objective formulation with respect to frame-indifference of a viscoplastic relationship between deformation rates and stresses of keroids.

The stress-state of a solid body may be defined by the symmetric tensor of Cauchy stress $\underline{T}$ [20]. Deformations can be defined with the tensor of deformation rates $\underline{D} \approx (\nabla \otimes \bar{v} + \nabla \otimes (\bar{v})^T)/2$, which is the symmetric part of the velocity gradient $\nabla \otimes \bar{v}$ whose components are the partial derivatives with respect to coordinates [20]. For reasons of objectivity, the Zeremba-Jaumann stress rate $\overset{\circ}{\underline{T}}$ is used, it is defined as

$$\overset{\circ}{\underline{T}} = \dot{\underline{T}} + \underline{T} \cdot \underline{W} - \underline{W} \cdot \underline{T}, \tag{3.21}$$

with the Cauchy stress rate $\dot{\underline{T}}$ and the spin tensor $\underline{W} \approx (\nabla \otimes \bar{v} - \nabla \otimes (\bar{v})^T)/2$.

The symmetric tensor of deformation rates $\underline{D}$ can be decomposed to an isotropic part $\underline{D}^{(K)}$ and to a deviatoric part $\underline{D}^*$. The tensorial decomposition can be written as

$$\underline{D} = \underline{D}^{(K)} + \underline{D}^*. \tag{3.22}$$

The isotropic component of deformation rates $\underline{D}^{(K)} = (\dot{\epsilon}_v \underline{1})/3$ describes the change of the volume of a body without change of its shape, and the *rate of volume change* is $\dot{\epsilon}_v = \operatorname{tr} \underline{D}$. The deviatoric component of deformation rates $\underline{D}^* = \underline{D} - (\dot{\epsilon}_v \underline{1})/3$ describes the change of the shape of a body without change of its volume.

For simplification, instead of the term 'deviatoric component of the tensor of deformation rates' the abbreviation 'deviatoric deformation rate' is used in the sequel.

$\|\underline{D}^*\| = \sqrt{D^*_{ij} D^*_{ij}}$ is the euklidic norm of the deviatoric deformation rate [20]. The relationship between the euklidic norm and the second deviatoric invariant J_2 is $\|\underline{D}^*\| = \sqrt{2J_2}$. Thus, the direction of deformation $\hat{D}^*$ may be defined by

$$\hat{D}^* = \frac{\underline{D}^*}{\|\underline{D}^*\|}. \tag{3.23}$$

Analogous to the tensor of deformation rates, the symmetric tensor of Cauchy-stresses $\underline{T}$ can be decomposed by

$$\underline{T} = \underline{T}^{(K)} + \underline{T}^{*}, \tag{3.24}$$

with an isotropic part $\underline{T}^{(K)} = p\underline{1}$ and with a deviatoric part $\underline{T}^{*} = \underline{T} - p\underline{1}$. $p = (\operatorname{tr}\underline{T})/3$ is usually called *mean pressure.*

It may be assumed for a viscoplastic constitutive relationship that the deformation rate $\underline{D}$ is composed of an elastic part $\underline{D}_{el}$ and of a viscous part $\underline{D}_{vi}$, so that

$$\underline{D} = \underline{D}_{el} + \underline{D}_{vi}. \tag{3.25}$$

Linear elasticity may be assumed for the reversible and time-independent part of the stress-deformation relationship for keroids. The relationship between stresses and deformations for linear elastic behavior of a homogeneous, isotropic solid body is known as *Hooke's law.* Hooke's law requires two independent constants G and ν which are called *shear modulus* and *Poisson's ratio.* A detailed description of Hooke's law and the derivation of G and ν from Lamé's constants can be found in [11]. The tensorial formulation of Hooke's law can be written with rates as

$$\overset{\circ}{\underline{T}} = 2G\underline{D_{el}} + 2G\frac{\nu}{1-2\nu}\left(\operatorname{tr}\underline{D_{el}}\right)\underline{1}. \tag{3.26}$$

The tensor of elastic deformation rates $\underline{D_{el}}$ can be split according to (3.22) and thus, equation (3.26) can be written with a deviatoric and an isotropic component as

$$\overset{\circ}{\underline{T}} = 2G\underline{D_{el}}^{*} + K\left(\operatorname{tr}\underline{D_{el}}\right)\underline{1}. \tag{3.27}$$

The constant K is called *bulk modulus*, and the relationship between K, G and ν is

$$K = \frac{2G\,(1+\nu)}{3\,(1-2\nu)}. \tag{3.28}$$

As outlined in section 3.2, a thermally activated, *non-linear viscosity* may be assumed for the non-reversible and time-dependent part of the stress-deformation relationship for keroids. A power law according to equation (3.20) has been found to be a suitable approximation for the relationship between stresses and deformations of a keroid body (see 3.2.6). Negligible volumetric viscosity has been assumed for keroid behavior (Sec. 2.3).

Thus, deviators of deformation rates and stresses suffice for a tensorial formulation of equation (3.20) which may be written as

$$\underline{T}^* = \left\| \underline{T_r}^* \right\| \hat{D_{vi}}^* \left(\frac{\left\| \underline{D_{vi}}^* \right\|}{\left\| \underline{D_r}^* \right\|} \right)^{1/n} . \tag{3.29}$$

$\underline{T_r}^*$ is a reference stress state at a reference deformation state $\underline{D_r}^*$. Frame-indifference and coaxiality between stresses and deformations require $\hat{D_{vi}}^*$ according to equation (3.23). The inversion of equation (3.29) can be written as

$$\underline{D_{vi}}^* = \left\| \underline{D_r}^* \right\| \hat{T}^* \left(\frac{\left\| \underline{T}^* \right\|}{\left\| \underline{T_r}^* \right\|} \right)^{n} , \tag{3.30}$$

with $\hat{T}^* = \underline{T}^* / \left\| \underline{T}^* \right\|$ which defines the directions of a viscous deformation. The term $(\left\| \underline{T}^* \right\| / \left\| \underline{T_r}^* \right\|)^n$ may be interpreted as the intensity of viscous deformation.
Linear viscosity is a special case of non-linear viscosity according to equation (3.30) for $n = 1$. Thus, the constitutive stress-deformation relation for a Newtonian fluid holds $\underline{D_{vi}}^* = \underline{T}^* / \eta$ with the so-called *dynamic viscosity* $\eta = \left\| \underline{T_r}^* \right\| / \left\| \underline{D_r}^* \right\|$.

According to equation (3.25) $\underline{D}_{el} = \underline{D} - \underline{D}_{vi}$, and equation (3.27) can be written as

$$\overset{\circ}{\underline{T}} = 2G \, (\underline{D}^* - \underline{D}^*_{vi}) + K \, (\mathrm{tr} \, \underline{D}) \, \underline{1}. \tag{3.31}$$

Thus, with (3.30) equation (3.31) holds

$$\overset{\circ}{\underline{T}} = 2G \left[\underline{D}^* - \left\| \underline{D_r}^* \right\| \hat{T}^* \left(\frac{\left\| \underline{T}^* \right\|}{\left\| \underline{T_r}^* \right\|} \right)^{n} \right] + K \, (\mathrm{tr} \, \underline{D}) \, \underline{1}. \tag{3.32}$$

Equation (3.32) is an argotropic constitutive relation between stress rates, stresses and deformation rates which can describe a non-linear viscoplastic behavior of keroids. Stationary creep can be reached for $\overset{\circ}{\underline{T}} = \underline{0}$ with stationary creep rates according to equation(3.30). Stress relaxation can be obtained for $\underline{D} = \underline{0}$. Then, with positive values of the norms of the tensors in equation (3.32), the components of the tensor of stress rates $\overset{\circ}{\underline{T}}$ have opposite signs of the corresponding deviatoric stress components of $\underline{T}^*$. Thus, the absolute values of the stress components decrease with respect to time, which means stress-relaxation.

3.3.3 One-dimensional considerations

One-dimensional stress-deformation relations can often be found in the literature, but they are insufficient for two- or three-dimensional boundary problems. Deviatoric tensorial formulations are needed for this purpose. One-dimensional relations may at best serve as an introduction. The following one-dimensional consideration of the viscoplastic constitutive relation (3.32) is only thought to illustrate it, and to give a simplified impression of the stress-deformation behavior of its single components. It also shows an analogy to commonly known rheological models. Graphical representations, e.g. stress-deformation diagrams, suffice for one-dimensional considerations, but they are useless for arbitrary deformations and can therefore even be misleading.

A simple rheological model for viscoplastic behavior may be a series connexion of a spring and a dash pot (Fig. 3.4). The spring represents elastic behavior, and the dash pot represents viscous behavior. In general, one of them or both can be linear or non-linear. A constant stress σ induces a rate of deformation $\dot{\epsilon}_{el}$ in the spring and $\dot{\epsilon}_{vi}$ in dash pot. Thus, the total deformation rate $\dot{\epsilon}$ for this series connexion holds

$$\dot{\epsilon} = \dot{\epsilon}_{el} + \dot{\epsilon}_{vi}. \tag{3.33}$$

Linear elasticity may be assumed for the spring. A one-dimensional stress-deformation relation for linear elasticity is known as Hooke's law with a constant of proportionality E, which is called Young's modulus. The derivative with respect to time of Hooke's law can be written as

$$\dot{\sigma} = E\dot{\epsilon}_{el}. \tag{3.34}$$

Non-linear viscosity may be assumed for the dash pot. A one-dimensional stress-deformation relation with a power law can be written as

$$\sigma = \sigma_r \left(\frac{\dot{\epsilon}_{vi}}{\dot{\epsilon}_r}\right)^{1/n}. \tag{3.35}$$

The required constants are $\dot{\epsilon}_r(\sigma_r)$, which is a reference deformation rate at a reference stress σ_r, and the exponent of viscosity n. Other than Norton's law (3.1), (3.35) is unit-invariant.

Linear viscosity may be assumed for so-called Newtonian fluids and is obtained with n=1, thus with a constant of proportionality $\eta = \sigma_r/\dot{\epsilon}_r$ which is called dynamic viscosity. For

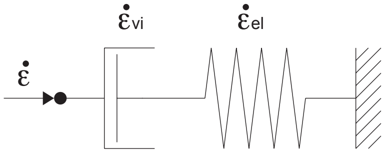

Figure 3.4: Rheological model for viscoplastic behavior

a linear elastic spring and linear viscous dash pot, the rheological model of Fig. 3.4 is known as a Maxwell body.

Equation (3.33) can be written with the elastic part of the deformation rate $\dot{\epsilon}_{el} = \dot{\sigma}/E$ of (3.34) as $\dot{\sigma} = E\left(\dot{\epsilon} - \dot{\epsilon}_{vi}\right)$, and with the viscous part of the deformation rate $\dot{\epsilon}_{vi} = \dot{\epsilon}_r \left(\sigma/\sigma_r\right)^n$ of (3.35) the constitutive relation between stress rate, stress and deformation rate holds

$$\dot{\sigma} = E\left[\dot{\epsilon} - \dot{\epsilon}_r \left(\frac{\sigma}{\sigma_r}\right)^n\right] . \tag{3.36}$$

Stationary creep is obtained for a constant stress σ (i.e. $\dot{\sigma}$=0), which means

$$\dot{\epsilon} = \dot{\epsilon}_r \left(\frac{\sigma}{\sigma_r}\right)^n . \tag{3.37}$$

Stress-relaxation is obtained for a constant deformation ϵ (i.e. $\dot{\epsilon} = 0$) as with (3.36) a negative stress rate $\dot{\sigma} = -E\dot{\epsilon}_r(\sigma/\sigma_r)^n$ indicates a decreasing stress with respect to time.

3.3.4 Constitutive relations with ABAQUS

Numerical simulations of element tests and a complete formulation of boundary problems can be carried out by means of finite elements. The finite-element program ABAQUS has been found to be suitable for this purpose as it provides tensorial formulations of the constitutive equations which have been outlined in Sec. 3.3.2. According to [22], the combination of linear elasticity and non-linear viscosity with a power law is implemented with (3.25).

Linear elastic material behavior according to (3.26) can be employed with ABAQUS by using the keyword $*ELASTIC, TYPE = ISOTROPIC$. The definition of isotropic linear elasticity requires two material constants, E (Young's modulus) and ν (Poisson's ratio), which are declared in a keyword-specific data line. The elastic constants have been determined by measurement of propagation delay of ultrasonic waves as described in Sec. 2.2.

Non-linear viscous material behavior according to (3.30) can be employed with ABAQUS by using the keyword $*CREEP, LAW = TIME$. The definition of non-linear viscosity with a power law requires two material constants, A and n, which are declared in a keyword-specific data line.

The definition of n is identical with the one in (3.30). Thus, n can be calculated from a reference stress state $\underline{T_r}^*$ at a reference deformation state $\underline{D_r}^*$ and a stress state $\underline{T}^*$ at a deformation state $\underline{D}^*$ which is different from the reference deformation rate by

$$n = \frac{\ln\left(\|\underline{D}^*\| \,/\, \|\underline{D_r}^*\|\right)}{\ln\left(\|\underline{T}^*\| \,/\, \|\underline{T_r}^*\|\right)}. \tag{3.38}$$

The parameter A is a substitution which can be calculated from a reference stress state $\underline{T_r}^*$ at a reference deformation state $\underline{D_r}^*$ according to (3.30) by

$$A = \left(\sqrt{\frac{3}{2}}\right)^{n+1} \cdot \left(\frac{\|\underline{D_r}^*\|}{\|\underline{T_r}^*\|^n}\right). \tag{3.39}$$

The dimension of A is $[T^{-1}F^{-n}L^{2n}]$, with chosen dimensions of time T, force F and length L. Thus, a A is dependent on n. ABAQUS provides so-called user-subroutines, which allow for programming user-defined material behavior (UMAT) by means of FORTRAN code. This would enable the use of the material constants $\|\underline{T_r}^*\|$, $\|\underline{D_r}^*\|$ and n. However, A is a constant for a constant temperature with constant reference stress state at a reference deformation rate. Thus, the use of the parameters A and n is sufficient for the boundary value problems at constant temperature which are considered in the sequel.

The differential equation (3.32) cannot be solved analytically. ABAQUS uses the backward Euler method (also referred to as the modified Crank-Nicholson operator) for implicit time integration. This works also with the one-dimensional equation 3.36 [22]. Additional detailed information on material definitions, numerical methods and syntax rules with ABAQUS can be found in [21], [22] and [23].

3.4 Numerical simulations of tests

3.4.1 Assumptions and restrictions

Numerical simulations of laboratory tests have been carried out by means of the finite-element method. A single first-order, axisymmetric continuum element (with ABAQUS a so-called CAX4 element) suffices for simulating shortening tests as long as the shape of a sample remains cylindrical, and as long as boundary conditions within a test (i.e.

applied stresses and deformations) remain axially symmetric. Boundary conditions have been defined for the numerical simulations in accordance with testing conditions in the laboratory, and material constants for nonlinear viscosity have been calculated from the results of laboratory tests. Fig. 3.5 shows boundary conditions for numerical simulations of an unconfined shortening test with controlled axial loading σ_{ax} (a), and of a confined shortening test with controlled axial deformation velocity v_{ax} and confining pressure p (b). Unconfined conditions have been simulated with (b) and $p = 0$. The four nodes of the finite element are labeled N1 to N4.
According to the observations that have been explained in Chap. 2, it has been assumed for the laboratory test that volumetric deformations are negligible and that the tested samples remain cylindrical. Thus, the components of the tensor of deformation rates hold

$$D_{rad} = D_{tan} = 0.5 \cdot D_{ax}. \tag{3.40}$$

In (3.40), rad, tan and ax are the indices for the radial, tangential and axial directions of a polar coordinate system).

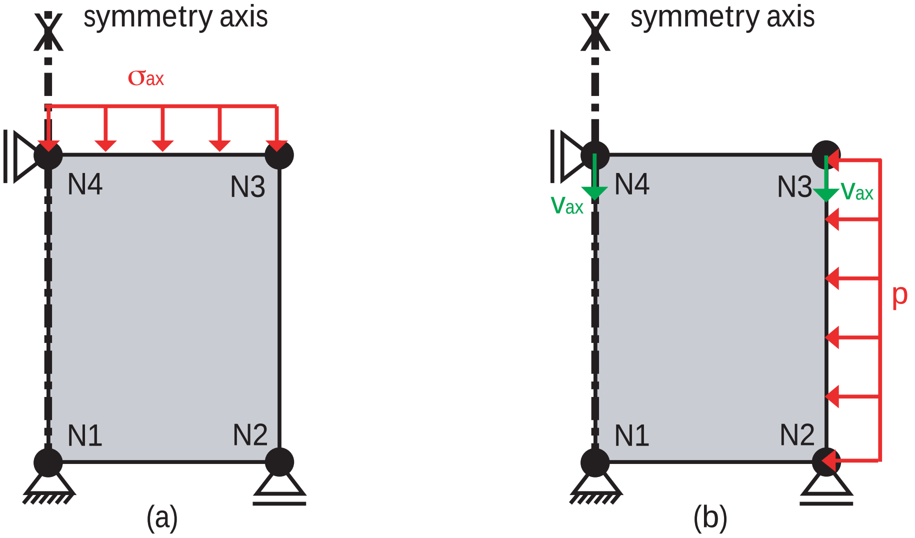

Figure 3.5: Boundary conditions for numerical simulations; (a) unconfined shortening test with controlled axial loading σ_{ax}, (b) confined shortening test with controlled axial deformation velocity v_{ax} and confining pressure p

The shape of the single finite element remains also cylindrical during the calculation. Bulging is excluded with the chosen first-order element. Friction at the contact faces between the sample and the load plates is excluded with the chosen boundary conditions. Continued shortening at constant velocity leads to a slight increase of the calculated axial stress. This can be neglected for small shortenings with respect to the sample height, and the axial shortening rate may be assumed as constant. An increase or decrease of the average axial stress due to an increasing (softening) or a decreasing (self-healing and hardening) number of micropores has been observed with the laboratory test, but the constitutive equation (3.30) that has been used for the calculations is not capable of these effects. Imperfections of the testing conditions (e.g. temperature changes during the test or oscillating deformation velocity) have not been considered in the calculations. Thus, the validity of the simulations of laboratory tests is restricted to constant material properties and idealized testing conditions.

3.4.2 Simulation of an unconfined shortening test with paraffin with controlled axial loading

A creep test with paraffin as described in Sec. 2.3 was simulated with boundary conditions according to Fig. 3.5(a), load stages according to Tab. 2.1 and with the constants of Tab. 3.1. n can be calculated with (3.38) in the range from about 3 to 4. $\|\underline{D}^*\|$ and $\|\underline{T}^*\|$ have been calculated from stages 3 and 4 of Tab. 2.1 with $\sigma = T_{ax}$, $T_{rad} = T_{tan} = 0$ (unconfined test), $\dot{\epsilon} = D_{ax}$ and $D_{rad} = D_{tan}$ according to (3.40). The components D_{ij} and T_{ij} are zero for axial symmetry.
Fig. 3.6 shows the results of the laboratory test (black) and those of a numerical simulation with ABAQUS (red). The result of the numerical simulation shows immediate axial deformations at the onset of each load stage as they have been observed with the laboratory test, but much smaller. The difference of immediate deformation between laboratory test and numerical simulation may result from vibrations which have been caused by adding or removing weights to or from the testing device, and to imperfect contact of the plates and the sample. Stationary creep is reached with the numerical simulation after less transition time than with the laboratory test, but the axial shortening rates that are reached at the end of each load stage are in good accordance with those of the laboratory test. Thus, the result of the numerical simulation shows that the markedly nonlinear viscoplastic behavior with stationary creep can be captured with the constitutive relation (3.30).

Table 3.1: Material constants for an unconfined creep test with paraffin

E	ν	$\|\underline{D_r}^*\|$	$\|\underline{T_r}^*\|$	n
[MPa]	[-]	[1/min]	[kPa]	[-]
1300	0.42	3.7E-7	18	3.4

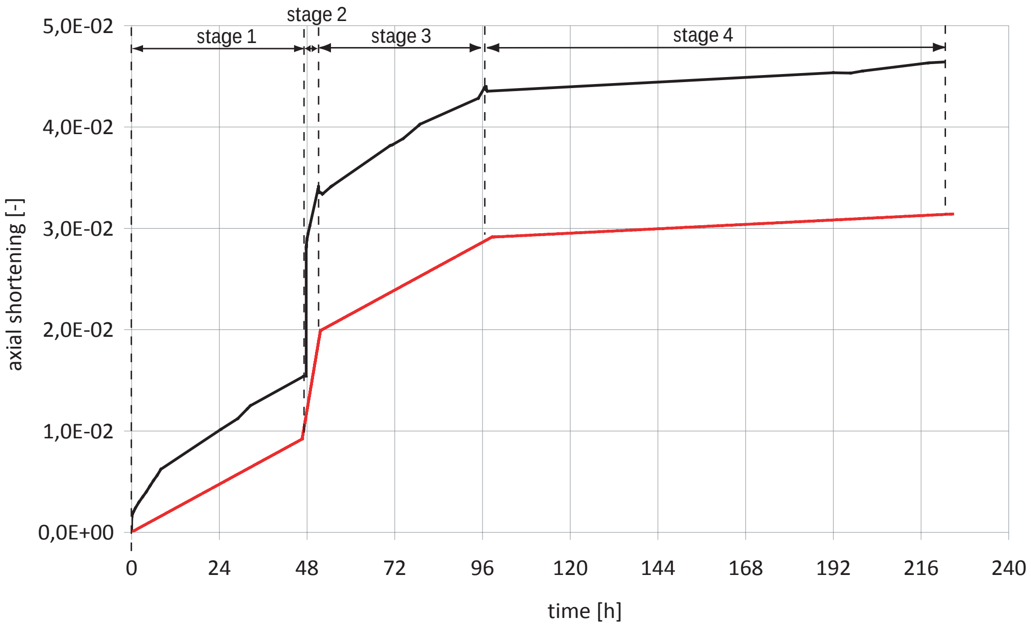

Figure 3.6: Unconfined axial shortening test with paraffin with controlled axial loading, axial shortening vs. time, results of laboratory test (black) and numerical calculation (red)

3.4.3 Simulation of unconfined shortening tests with paraffin with controlled axial deformation velocity

Unconfined shortening tests with paraffin with controlled axial deformation velocity as described in Sec. 2.3 were simulated with stages of constant shortening velocity according to Fig. 3.5(b) with $p = 0$.
A shortening test with paraffin as described in Sec. 2.3 was simulated with velocity stages according to Tab. 2.2 and with the constants of Tab. 3.3. n can be calculated with (3.38) in the range from about 4 to 5. $\|\underline{D}^*\|$ and $\|\underline{T}^*\|$ have been calculated from stages 1 and 4 of the test as outlined in Sec. 3.4.2 with axial stresses and shortening rates according to Tab. 3.2.

Fig. 3.7 shows the results of the laboratory test (black) and those of a numerical simulation with ABAQUS (red). At the onset of the numerical simulation of the laboratory test, the calculated axial stress increases with continued deformation as it has been measured during the laboratory test, but faster. The calculated initial stiffness is higher than for the laboratory test. According to the test result, a limit state is asymptotically attained with the calculation and characterized by a maximum axial stress, which indicates a steady state. A sudden decrease or increase of the axial shortening velocity can be

Table 3.2: Unconfined axial shortening test with paraffin, magnitudes of shortening rates and related stresses at evaluated velocity stages

stage	D_{ax}	T_{ax}
	[1/min]	[kPa]
1	2E-4	800
4	2E-3	1300

Table 3.3: Material constants for an unconfined shortening test with paraffin

E	ν	$\lVert \underline{D_r}^* \rVert$	$\lVert \underline{T_r}^* \rVert$	n
[MPa]	[-]	[1/min]	[kPa]	[-]
1300	0.42	2.5E-4	653	4.6

simulated with a modification of boundary conditions during the numerical calculation. As observed with the laboratory test, the axial stress decreases, or respectively increases, after a modification of the axial velocity of the nodes N3 and N4 (Fig. 3.5(b)). New limit states with limit stresses related to the corresponding shortening rate are reached. The calculated transition times are shorter than during the laboratory test, but the calculated maximum stresses are in good accordance with the maximum stresses that have been measured in the laboratory. As outlined in Sec. 3.4.1, the calculated axial stress increases slightly with continued deformation due to an continued increase of the shortening rate. A peak and subsequent softening is not captured with the calculation. A disproportionally high increase of the limit stress after an increase of the initial shortening rate by a factor of hundred can also be calculated and is in good accordance with the test result if the sample material remains ductile (stage 6). Thus, the constitutive relation (3.30) is suitable for numerical calculations of the markedly nonlinear argotropic behavior of paraffin in the ductile regime.

A shortening test with paraffin with testing conditions according to Tab. 2.3 has been described in Sec. 2.3. The stages 1 to 6 of this test were simulated with stages of constant shortening velocity according the testing conditions (Tab. 2.2) and with the constants of Tab. 3.5. The constants have been calculated with axial stresses and shortening rates according to Tab. 3.4 as outlined above. n can be calculated with (3.38) in the range from about 2 to 4. Shear localization began during stage 6, and the axial symmetry of the test was lost. Thus, stage 7 of the laboratory test was not simulated with the axially symmetric numeric model.

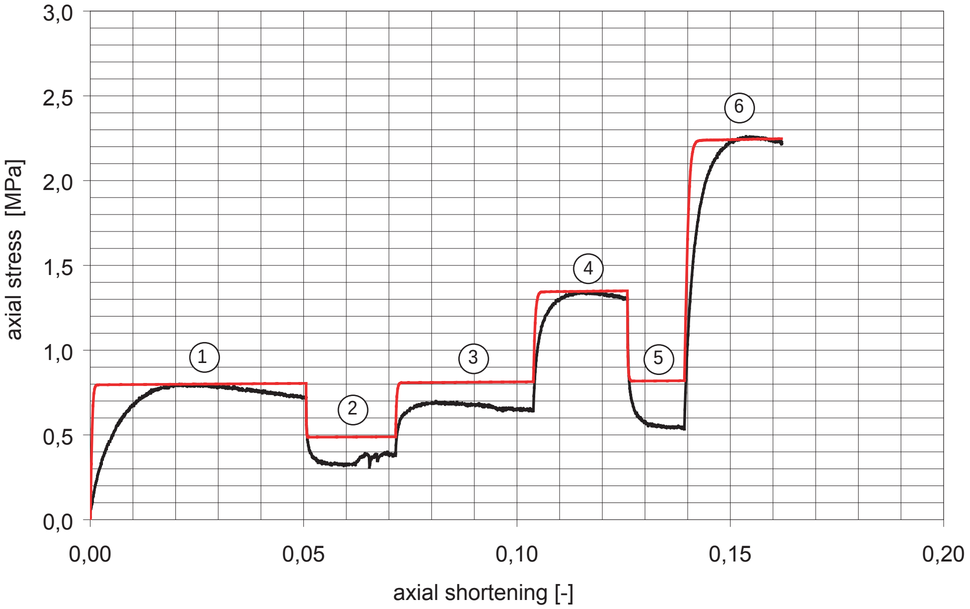

Figure 3.7: Unconfined shortening test with paraffin with controlled axial deformation velocity, axial stress vs. axial shortening, results of laboratory test (black) and numerical simulation (red)

Fig. 3.8 shows the results of the laboratory test (black) and of a numerical simulation with ABAQUS (red). With the simulation, limit states are also attained asymptotically with maximum axial stresses, but within shorter transition times than during the laboratory test. The attained limit states are related to a corresponding shortening rate, and the calculated maximum stresses are again in good accordance with the maximum stresses that have been measured with the laboratory test during the stages 1 to 5 (i.e. ductile regime). Thus, the constitutive relation (3.30) is suitable for numerical calculations within the range of deformation rates that have been tested during the stages 1 to 5.

The increase of the shortening rate during stage 6 of the laboratory test leads to clastic behavior. The marked peak of the axial stress and its subsequent decrease with continued shortening (Fig. 3.8) was accompanied by the onset of shear localization. In contrast to the measured stress-deformation behavior, the numerical simulation leads to a steady state for the deformation rate of stage 6. A peak of the axial stress is not attained with the simulation and the simulated axial stress is higher than it was reached with the laboratory test. Thus, the axial stress that can be reached with the shortening rate of stage 6 is overestimated with the carried-out numerical simulation. The evolution of the axial stress that has been measured with the laboratory test during this stage cannot be captured.

Thus, with the onset of clastic behavior, the constitutive relation (3.30) is no more valid to describe the stress-deformation relationship of keroids. Numerical simulations within a clastic regime with (3.30) are misleading. The results of such simulations are fertile ground for misinterpretations and may lead to dangerous mispredictions of material behavior. Therefore, the suggested use of (3.30) is restricted to the ductile regime.

Table 3.4: Unconfined shortening test with paraffin, magnitudes of shortening rates and related stresses at evaluated velocity stages

stage	D_{ax}	T_{ax}
	[1/min]	[kPa]
1	3E-4	660
4	3E-3	1450

Table 3.5: Material constants for an unconfined shortening test with paraffin

E	ν	$\lVert \underline{D_r}^* \rVert$	$\lVert \underline{T_r}^* \rVert$	n
[MPa]	[-]	[1/min]	[kPa]	[-]
1300	0.42	3.7E-4	539	2.8

3.4.4 Simulation of confined shortening tests with reconstituted clay with controlled axial deformation velocity

A shortening test with reconstituted clay with testing conditions according to Tab. 2.5 has been described in Sec. 2.5. The testing conditions were modeled with stages of constant shortening velocity according to Tab. 2.5 and with the constants of Tab. 3.7. n can be calculated with (3.38) in the range from about 45 to 55. The constants have been calculated with axial stresses and shortening rates according to Tab. 3.6 as outlined above.

Fig. 3.9 shows the results of the laboratory test (black) and of a numerical simulation with ABAQUS (red). The limit states that have been reached with the laboratory test are also asymptotically attained with the simulation, but within shorter transition times. The calculated maximum stresses are in good accordance with the maximum stresses in the test. Thus, the numerical model is capable to simulate the argotropic stress-deformation behavior within the tested range of deformation rates. However, the observed decrease of deviatoric stress after a critical point has been reached (stage 6 of the laboratory test) cannot be simulated with this numerical model.

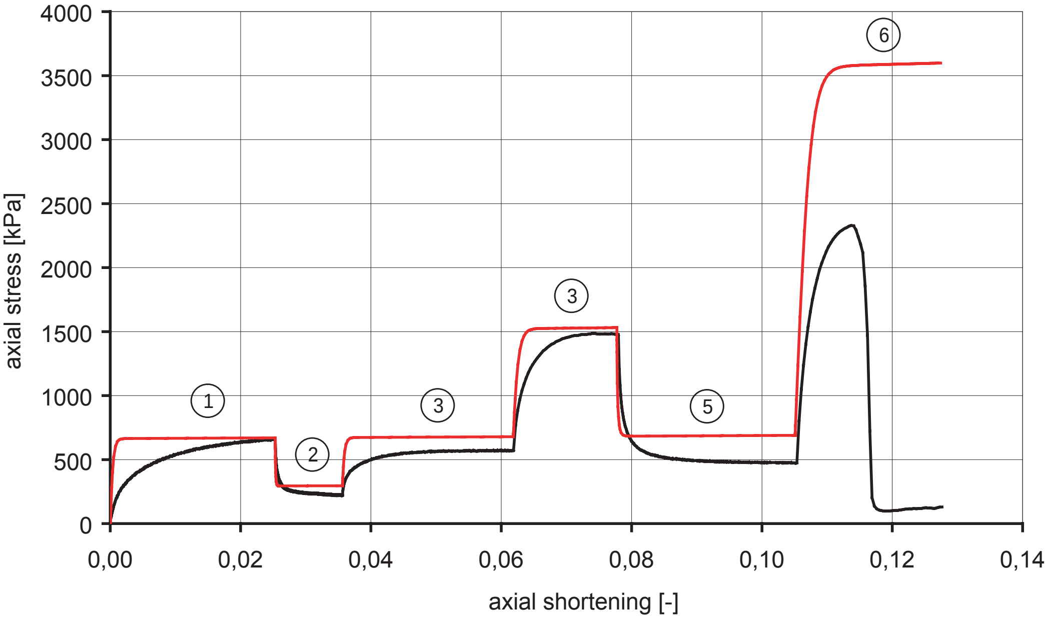

Figure 3.8: Unconfined shortening test with paraffin with controlled axial deformation velocity, axial stress vs. axial shortening, results of laboratory test (black) and numerical simulation (red)

Table 3.6: Confined shortening test with reconstituted clay, magnitudes of shortening rates and related stresses at evaluated velocity stages

stage	D_{ax}	T_{ax}	T_{rad}
	[1/min]	[kPa]	[kPa]
3	1.5E-4	3870	5000
4	1.5E-3	4050	5000

Table 3.7: Material constants for a confined shortening with a clay sample

E	ν	$\|\underline{D_r}^*\|$	$\|\underline{T_r}^*\|$	n
[MPa]	[-]	[1/min]	[kPa]	[-]
3512	0.36	1.8E-4	6320	50.1

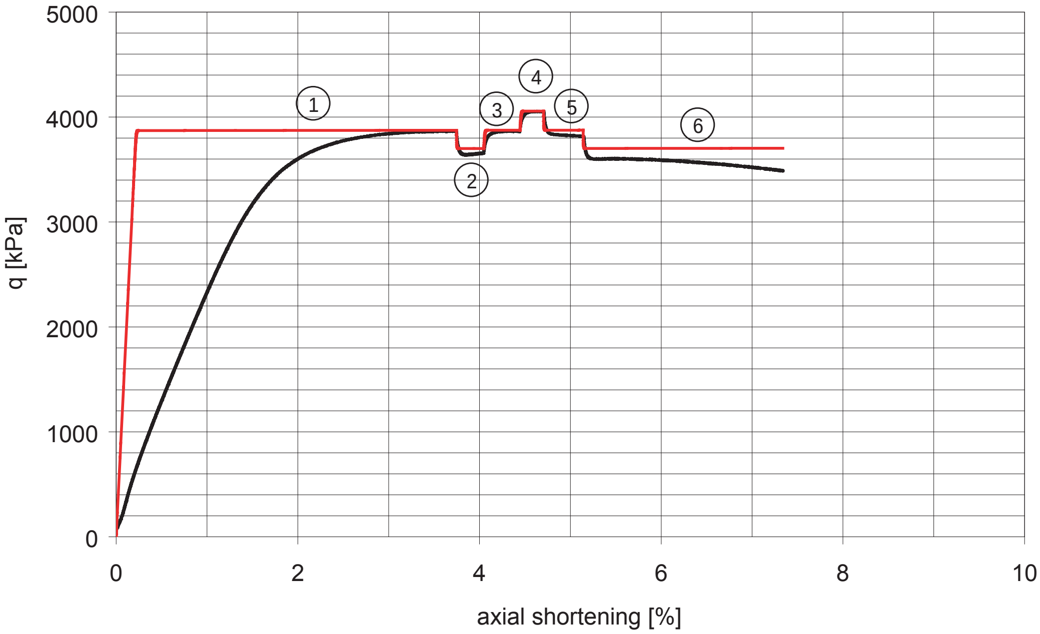

Figure 3.9: Confined shortening test with reconstituted clay with controlled axial deformation velocity, deviatoric stress q vs. axial shortening, results of laboratory test (black) and numerical simulation (red)

3.4.5 Simulation of confined shortening tests with reconstituted bentonite samples with controlled axial deformation velocity

Axial shortening tests with reconstituted bentonite samples have been described in Sec. 2.4. Two confined shortening tests with controlled axial deformation velocity have been simulated with the numerical model described above.

A laboratory test has been modeled with velocity stages according to Tab. 2.4 and with the constants of Tab. 3.9. The constants have been calculated with axial stresses and shortening rates according to Tab. 3.8 as outlined above and with the following assumptions. It appears, from the results of the laboratory test, that a limit state is reached at the end of stage 7 for a shortening rate of about 1.4E-3 1/min (stages 1,3,5,7). Therefore, the maximum deviatoric stress $T_{ax,7}$ at the end of stage 7 has been chosen as reference stress. The difference of deviatoric stresses between the stages 1 or 3 (same shortening rates as stage 7) and stage 2 amounts approximately $\Delta\sigma = 400$ kPa. Thus, the maximum axial stress which would be reached with continued deformation at the constant shortening rate of stage 2 can be calculated with $T_{ax,2} = T_{ax,7} + 2\Delta\sigma$.

Fig. 3.10 shows the results of the laboratory test (black) and of a numerical simulation with ABAQUS (red). At the onset of the numerical simulation (stage 1), the calculated axial stress increases faster with continued deformation than it has been observed during the laboratory test. Fig. 3.10 reveals that the material behaves stiffer with the simulation than in the laboratory test. A limit state is asymptotically attained with the simulation at an axial shortening of approximately 0.5%. The calculated maximum axial stress indicates a steady state and remains nearly constant until the end of stage 1. The measured axial stress is still increasing at the end of stage 1 of the test thus, a limit state is not yet reached within stage 1 of the laboratory test. The subsequent simulated stages show likewise differences with the test results as the first stage. However, the increases or decreases of calculated deviatoric stresses for increases or decreases of simulated shortening rates are in good accordance with those which are observed with different shortening rates with a laboratory test. Thus, the numerical model is capable to simulate the argotropic behavior of the material within the tested range of deformation rates.

Table 3.8: Confined shortening test with reconstituted bentonite, magnitudes of shortening rates and related stresses at evaluated velocity stages

stage	D_{ax}	T_{ax}	T_{rad}
	[1/min]	[kPa]	[kPa]
7	1.4E-3	22200	10000
2	1.4E-2	23000	10000

Table 3.9: Material constants for a confined shortening with a reconstituted bentonite sample

E	ν	$\left\|\underline{D_r}^*\right\|$	$\left\|\underline{T_r}^*\right\|$	n
[MPa]	[-]	[1/min]	[kPa]	[-]
2470	0.29	1.7E-3	9961	35.7

A laboratory test with a single shortening velocity stage, according to a constant shortening rate of 1.4E-3 1/min, has been modeled with the constants of Tab. 3.11. The constants have been calculated with axial stresses and shortening rates according to Tab. 3.10 as outlined above and with the following assumptions. The maximum deviatoric stress $T_{ax,1}$ at the end of the laboratory test has been chosen as reference stress. According to a laboratory test with temporarily constant velocity stages (Tab. 2.4), the difference of deviatoric stresses between the stages for an increase of the shortening rate from 1.4E-3

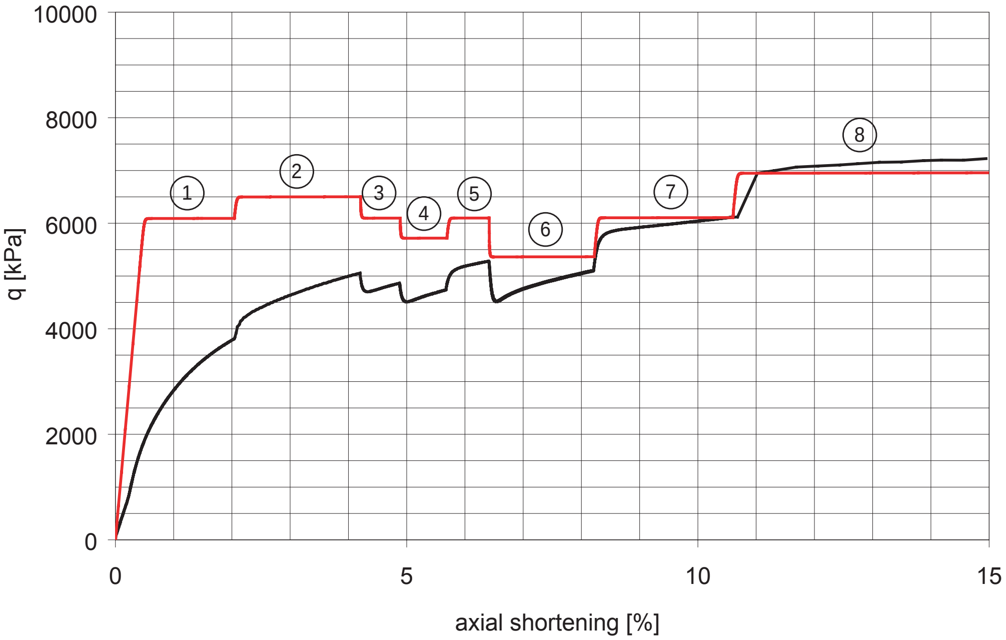

Figure 3.10: Confined shortening test with reconstituted bentonite with controlled axial deformation velocity, deviatoric stress q vs. axial shortening, results of laboratory test (black) and numerical simulation (red)

1/min to 1.4E-2 1/min has been assumed with $\Delta\sigma = 400$ kPa. Thus, a maximum axial stress which would be reached with a shortening rate of 1.4E-2 1/min (fictitious stage 1*) can be calculated with $T_{ax,1*} = T_{ax,1} + 2\Delta\sigma$.

Fig. 3.11 shows the results of the laboratory test (black) and of a numerical simulation with ABAQUS (red). The evolution of the axial stress reveals that the initial stiffness of the material is higher with the simulation than with the laboratory test. A limit state is asymptotically attained with the simulation as with the laboratory test, but with less axial deformation. The transition to a steady state is smoother with the laboratory test than with the calculation, thus the axial deformation is underestimated with the calculation at deviatoric stresses near the limit state. However, the maximum deviatoric stress, which is attained with the simulation, is in good accordance with the result of the laboratory test. The ductile behavior can thus be roughly captured with the numerical simulation.

The direction of the axial deformation was reversed during the laboratory test when an axial shortening of approximately 16% (Fig. 3.11) has been reached. Then the sample was axially lengthened with a same constant rate (1.4E-3 1/min) as for the shortening. A comparison of the evolution of the calculated deviatoric stress with those measured with the laboratory test reveals that the stiffness coincides for small decreases of the deviatoric stress (i.e. small lengthenings). Continued lengthening of the sample leads to a disproportionally high decrease of the deviatoric stress down to an isotropic stress state during the laboratory test, whereas the numerical simulation shows a nearly linear relation between the decreasing deviatoric stress and the axial stress. Thus, the hysteretic stress-deformation behavior for alternated shortening and lengthening that has been observed with the laboratory test cannot be captured with the proposed numerical simulation.

Table 3.10: Confined shortening test with reconstituted bentonite, magnitudes of shortening rates and related stresses at evaluated velocity stages

stage	D_{ax}	T_{ax}	T_{rad}
	[1/min]	[kPa]	[kPa]
1	1.4E-3	15140	5000
1*	1.4E-2	15940	5000

Table 3.11: Material constants for a confined shortening with a reconstituted bentonite sample

E	ν	$\lVert \underline{D_r}^* \rVert$	$\lVert \underline{T_r}^* \rVert$	n
[MPa]	[-]	[1/min]	[kPa]	[-]
2470	0.29	1.7E-3	8279	29.8

3.4.6 Simulation of confined shortening tests with cored claystone samples with controlled axial deformation velocity

Shortening tests with cored claystone samples have been described in Sec. 2.6. A confined shortening test with controlled axial deformation velocity has been simulated with the numerical model described above.

A laboratory test has been modeled with velocity stages according to Tab. 3.12 and with the constants of Tab. 3.14. The constants have been calculated with axial stresses and shortening rates according to Tab. 3.13 as outlined above and with the following assumptions. It appears, from the results of the laboratory tests which have been described in Sec. 2.6, that a limit state is reached with a shortening rate of about 2.8E-5 1/min at a maximum deviatoric stress of approximately q_{ref} = 24000 kPa (Fig. 2.24 and 2.25). For a test with temporarily constant shortening velocities (Fig. 2.25), the increase of deviatoric stress from the stages 3 or 5 (D_{ax} = 2.8E-5 1/min) to stage 4 (D_{ax} = 2.8E-4

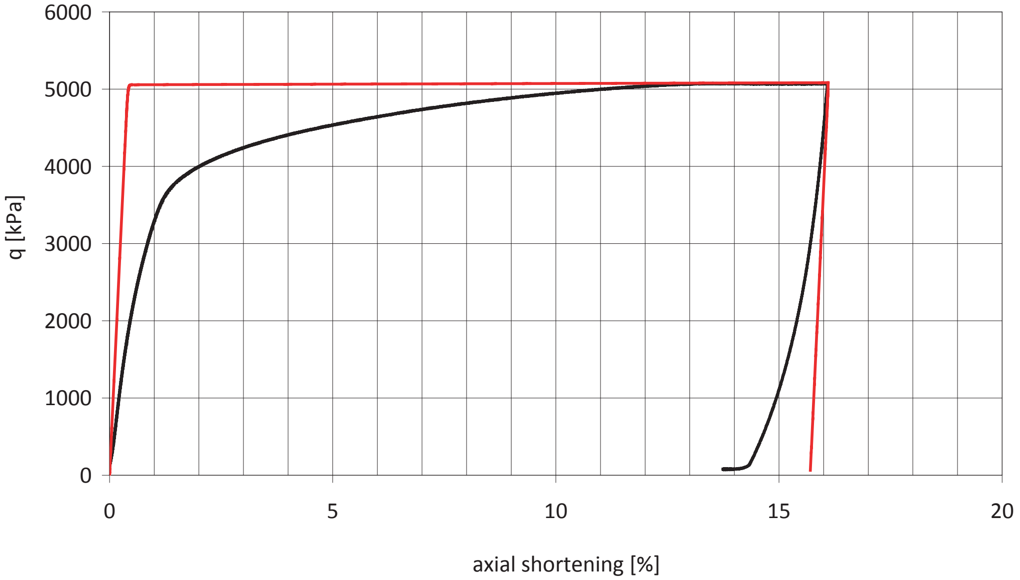

Figure 3.11: Confined shortening test with reconstituted bentonite with controlled axial deformation velocity, deviatoric stress q vs. axial shortening, results of laboratory test (black) and numerical simulation (red)

1/min) amounts approximately Δq = 850 kPa. Thus, the maximum deviatoric stress which would be reached with continued deformation at the constant shortening rate of stage 4 can be calculated with $q_4 = q_{ref} + \Delta q$.
Fig. 3.12 shows the results of a laboratory test with a single velocity stage (black) and of a numerical simulation with ABAQUS (red). The comparison of the evolution of deviatoric stresses reveals that the material behaves markedly stiffer with the simulation than observed in the laboratory test. A limit state is asymptotically attained with the simulation like with the test, but with less deformation. The calculated and the measured maximum deviatoric stress are in fair accordance. The laboratory test has been stopped after an axial shortening of 1.9%. A subsequent simulated velocity stage with an increase of the shortening rate by a factor of ten shows a similar increase of the deviatoric stress as it has been observed with a laboratory test (Fig. 2.25, stage 4). The increase or decrease of calculated deviatoric stresses for a simulated increase or decrease of shortening rates by a factor of ten are in good accordance with observations at equivalent shortening rates during a laboratory test. Thus, the numerical model is at best capable to simulate the argotropic behavior of a cored claystone within the tested range of deformation rates.

Table 3.12: Simulation of a confined shortening test with cored claystone, shortening rates at constant velocity

stage	D_{ax}
	[1/min]
1	2.8E-5
2	2.8E-4
3	2.8E-5

Table 3.13: Confined shortening test with cored claystone, magnitudes of shortening rates and related stresses at evaluated velocity stages

stage	D_{ax}	T_{ax}	T_{rad}
	[1/min]	[kPa]	[kPa]
1	2.8E-5	58000	10000
1*	2.8E-4	59700	10000

3.5 Conclusions

Plasticity is a kind of nonlinear viscosity, and is thermally activated. Viscous effects in solids can be physically explained with thermally activated changes of pre-existing dislocations. Therefore, constitutive equations should be based on a kind of rate process theory and provide a description of argotropic behavior, creep and relaxation. Such approaches are, at least for the time being, restricted to monotonous evolutions, therefore cyclic deformations and ratcheting are not considered in this study. The assumed absence of pores excludes fracturing with an increasing number and size of pores, and self-healing is prevented by too fast extensions. Mechanical heating due to insufficient conduction of dissipated energy is excluded. In other words, the material is assumed as ductile at sufficiently low stretching rates. Thus the state of the material (including its fabric) is

Table 3.14: Material constants for a confined shortening with a cored claystone sample

E	ν	$\|\underline{D_r}^*\|$	$\|\underline{T_r}^*\|$	n
[MPa]	[-]	[1/min]	[kPa]	[-]
13100	0.31	3.4E-5	39191	65.6

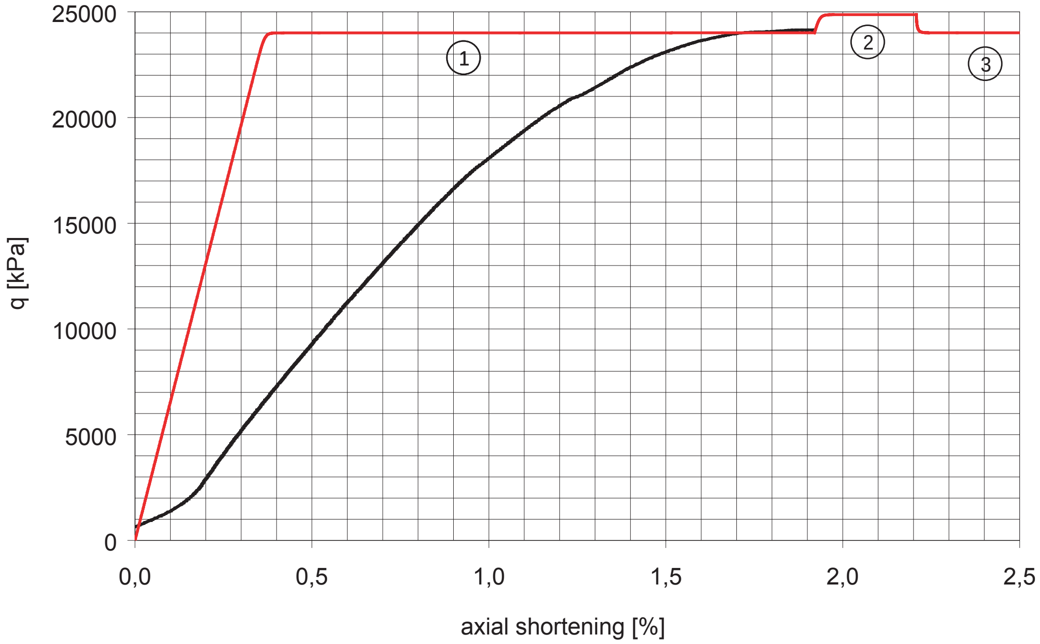

Figure 3.12: Confined shortening test with cored claystone with controlled axial deformation velocity, deviatoric stress vs. axial shortening, results of laboratory test (black) and numerical simulation (red)

determined by stress only so that an inherent anisotropy is neglected. Such idealized materials are named keroids (Greek: wax-like).

The employed viscoplastic constitutive equation for keroids satisfies the requirements of objectivity. Arbitrary isochoric deformations can be captured by deviatoric relations of stress rate with stress and deformation rate. Invariance with respect to units is achieved by two material constants, viz. a stress which can be expressed as an energy per volume and a time which can be expressed by a frequency. Invariance with respect to an arbitrarily chosen reference system is guaranteed by an isotropic tensor function. Thus, there is no influence of a rotating coordinate system, and since only deformation rates (and not strain) matters for the material behavior there is also no influence of an arbitrarily chosen starting time. Since no internal variable is employed, the fabric of the keroid is assumed to be determined by deviatoric stress only. The employed constitutive relation is applicable to processes without volume change up to a steady state, but not beyond this limit.

Chapter 4

One-dimensional boundary value problems

4.1 Overview

In this chapter two one-dimensional boundary value problems with creeping formations are considered with respect to the evolution of velocity and stress. The first problem considers the stationary creep of an infinite slope. First an analytical solution for the stationary field of velocity and stress is presented. Then results of numerical simulations of this problem are compared with the analytical solution. The second problem considers the convergence of a borehole. Numerical simulations are presented, which show that an initially not radially symmetric stress field leads to a radially symmetric one if the shape of the hole is kept radially symmetric. The considered boundary problems imply idealizing assumptions. The presented results are nevertheless of practical use since initial stress and velocity fields of real problems with corresponding conditions can thus be estimated in an objective way.

4.2 Stationary creep of an infinite slope

4.2.1 The boundary value problem

The boundary value problem described below is an idealization of an *extended slope* with a homogeneous viscous formation. Extended means that its lateral extents are much longer than its thickness. The inclined viscous layer is bound by a formation called *bedrock*,

which can be considered as not viscous and much stiffer than the *overburden*. Examples for such geological structures can be creeping slopes of rock, soil or glaciers. The range of applications may be extended to a viscous layer underlying non-viscous formations of a slope with a dead load on the surface of the viscous layer, however this is not considered in the sequel.
An idealized boundary value problem is an *infinite slope* with a constant thickness d (Fig. 4.1). Infinite means that the extension of the slope in the directions of dipping and striking is not limited, and that no changes of state and velocity occur along those directions. The slope is homogeneous and consists of a keroid in the sense of Chap. 2, with the specific gravity γ. The surface of the slope is free and thus unloaded. The inclination of the slope is called β, the bedrock is not deformable and remains in place.

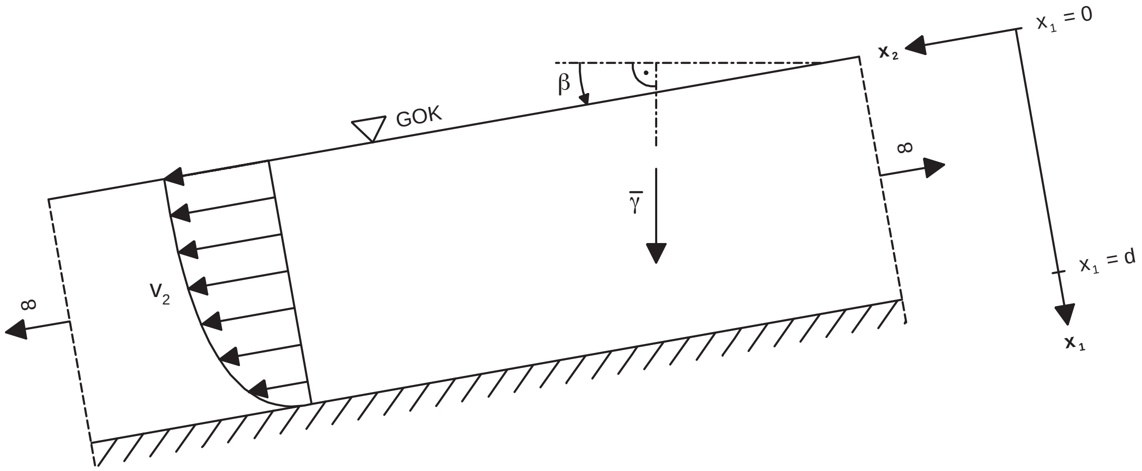

Figure 4.1: Infinite slope, geometry and boundary conditions

4.2.2 Analytical solution

The boundary value problem of an infinite slope is considered as a plane strain problem in a vertical cross section parallel to the direction of dipping. Plane strain conditions require

$$D_{i3} = D_{3i} = 0 \tag{4.1}$$

for the tensor of strain rates, and the infinite extension of the slope in 2-direction requires $\partial/\partial x_2 = 0$, thus

$$D_{22} = \frac{\partial v_2}{\partial x_2} = 0 \; . \tag{4.2}$$

A stationary state requires

$$D_{11} = \frac{\partial v_1}{\partial x_1} = 0 \ , \tag{4.3}$$

otherwise the thickness of the slope would change indefinitely.
Thus, all components of the tensor of strain rates except $D_{12} = D_{21}$ are zero:

$$\begin{aligned} &D_{ii} = 0 \ , \\ &D_{23} = D_{31} = 0 \ , \\ &D_{12} = \tfrac{1}{2}\partial v_2/\partial x_1 \ . \end{aligned} \tag{4.4}$$

With tr$\underline{D} = 0$ the constitutive equation for keroids (3.32) can be reduced to

$$\underline{D}^* = D_r \frac{\underline{T}^*}{\|\underline{T}^*\|} \left(\frac{\|\underline{T}^*\|}{\sigma_r} \right)^n . \tag{4.5}$$

with $\underline{D} = \underline{D}^*$ for a stationary stress field $\dot{T}_{ij} = 0$.

Static equilibrium requires

$$T_{ij,j} + f_i = 0 \tag{4.6}$$

for the tensor of stresses, with the abbreviation

$$T_{ij,j} = \sum_{j=1}^{3} \frac{\partial T_{ij}}{\partial x_j} \ , \ i = 1, 2, 3 \ . \tag{4.7}$$

For an infinite slope with gravity the vector of volume forces is

$$\bar{f} = x_1 \gamma \begin{bmatrix} \cos\beta \\ \sin\beta \\ 0 \end{bmatrix} . \tag{4.8}$$

Infinity of the slope in 2- and 3-direction requires that there are no changes of state along these directions, i.e. partial derivatives in these directions vanish for any quantity Q,

$$\frac{\partial Q_{i,2}}{\partial x_2} = \frac{\partial Q_{i,3}}{\partial x_3} = 0 \ . \tag{4.9}$$

Plane-parallelity of the problem requires also

$$T_{23} = T_{31} = 0 \tag{4.10}$$

for the shear stresses T_{23} and T_{31}.
With the Cauchy stress vector

$$t_i = T_{ij} n_i \tag{4.11}$$

and the boundary condition $t_i = 0$ at the free surface $x_1 = 0$, with the unit vector

$$\bar{n} = \begin{bmatrix} -1 \\ 0 \\ 0 \end{bmatrix} , \tag{4.12}$$

we have thus a system of equations by which the stress tensor is defined except for two components T_{22} and T_{33}, viz.

$$\underline{T} = \begin{bmatrix} -\gamma x_1 \cos\beta & -\gamma x_1 \sin\beta & 0 \\ -\gamma x_1 \sin\beta & T_{22} & 0 \\ 0 & 0 & T_{33} \end{bmatrix} . \tag{4.13}$$

(Note that pressure is negative in continuum mechanics). In general the two unknown components are different, $T_{22} \neq T_{33}$. In the case of a stationary velocity field the tensor of strain rates and the constitutive equation are given by (4.4) and (4.5). Then,

$$T_{11} = T_{22} = T_{33} \tag{4.14}$$

holds for a stationary state. The components T^*_{ij} of the tensor of deviatoric stresses can be derived from (4.5) with (4.4) and (4.13). For stationary conditions, the norm of deviatoric stresses $\|\underline{T}^*\|$ is temporally constant, and all components except T^*_{12} are zero.
Thus, the only equation which has to be solved is

$$D_{12} = \frac{D_r}{\sigma_r^n} \left(\sqrt{2} \gamma x_1 \sin\beta \right)^{n-1} T^*_{12} , \tag{4.15}$$

or with (4.4)

$$\frac{\partial v_2}{\partial x_1} = -\alpha x_1^n \tag{4.16}$$

and the constant factor

$$\alpha = -\frac{D_r}{\sigma_r^n}\sqrt{2}\left(\sqrt{2}\gamma\sin\beta\right)^n \ . \tag{4.17}$$

Integration of (4.16) yields

$$v_2 = -\alpha\frac{1}{n+1}x_1^{n+1} + C \ , \tag{4.18}$$

and the integration constant C is determined by the boundary condition that the slope is fixed on the bedrock. This means $v_2 = 0$ for $x_1 = d$, and thus

$$C = \alpha\frac{1}{n+1}d^{n+1} \ . \tag{4.19}$$

Thus, the only non-zero velocity component depends on the coordinate x_1 by

$$v_2 = \frac{\sqrt{2}}{n+1}\cdot\frac{D_r}{\sigma_r^n}\left(\sqrt{2}\gamma\sin\beta\right)^n\left(d^{n+1} - x_1^{n+1}\right) \ . \tag{4.20}$$

The maximum velocity is obtained at the surface $x_1 = 0$, viz.

$$v_{2,0} = \frac{\sqrt{2}}{n+1}\cdot\frac{D_r}{\sigma_r^n}\left(\sqrt{2}\gamma\sin\beta\right)^n d^{n+1}. \tag{4.21}$$

The velocity profiles are parabolas of the order $n+1$ (Fig.4.2). For convenience, the profiles are referred to the velocity at the surface $v_{2,0}$. The shapes of the velocity profiles depend only on the power n for a given keroid and on the inclination of the slope. For high values of n the major part of deformations occurs near the bottom of the slope. The thickness of this zone decreases with increasing n.

This analytical solution includes linear viscosity for $n = 1$. Then, the velocity profile is a quadratic parabola which is known for Newtonian fluids, viz.

$$v_2 = \frac{1}{2\eta}\gamma\sin\beta\left(d^2 - x_1^2\right) \ , \tag{4.22}$$

with $2\eta = \sigma_r/D_r$.

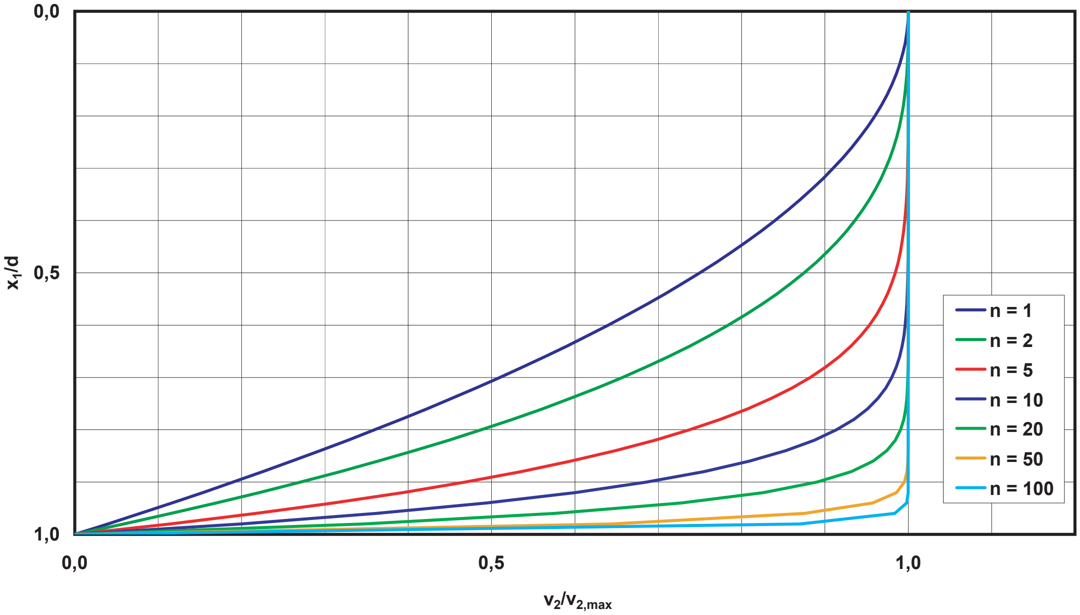

Figure 4.2: Normalized velocity profiles by (4.20) for an infinite slope

4.2.3 Numerical approach

Fig.4.3 shows a finite-element mesh which is apt to simulate evolutions for different inclinations β of an infinite slope. No modification of the mesh is necessary by taking the gravitation vector $\bar{g}$ inclined by β. Any thickness d can be considered, and a constant specific weight γ.

The viscoplastic layer is fixed at the bottom $x_1 = d$. Plane strain continuum elements with 4 nodes are used. The plane-parallelity, due to infinite extension in 1-direction, is captured by the condition that displacements of nodes in planes parallel to the 2-3-plane are identical. The corresponding equations for the two node sets n_{left} at $x_2 = 0$ and n_{right} at $x_2 = -1$ are thus

$$\begin{aligned} u_1^{(left)} - u_1^{(right)} &= 0 \; , \\ u_2^{(left)} - u_2^{(right)} &= 0. \end{aligned} \tag{4.23}$$

Van den Ham [37] has also developed a model of an extended slope, but boundary conditions have not been properly chosen. Thus, asymptotic states cannot be attained with his model.

The simulations were carried out with material parameters of paraffin ($n = 3.2$) and of

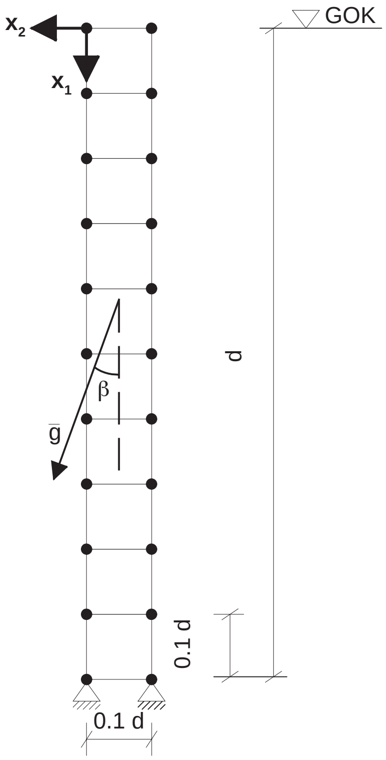

Figure 4.3: Finite-element model

reconstituted claystone ($n = 41.9$) as presented in Chap. 2. The results are only presented for paraffin, they are qualitatively the same for claystone. Differences for the two materials will be pointed out. The numerical simulation started with an arbitrary allowable state of stress, e.g. a geostatic state, i.e. $T_{11} = \gamma x_1$, $T_{22} = K_0 T_{11}$, $K_0 = 0.67$. The initial velocity of the slope was assumed as zero.
Fig. 4.4 shows the evolution of displacements in the direction of dipping. After a transition the displacement profiles get affine and the velocities do not change anymore. This means that a stationary state is reached so that further curves can be obtained by scaling U_1/d with a constant factor U_1. The stationary state is reached within the dimensionless time 0.4 tD_r, and the required displacement at the surface to reach this state is less than $10^{-3}d$. As will be shown further below for typical claystones, a time $2 \cdot 10^{10}/D_r$ and a displacement at the surface less than $10^{-6}d$ are required to reach stationarity.

A calculated evolution of the velocity at the surface is shown in Fig. 4.5. The analytical solution (4.21) provides a constant velocity. This asymptotic value is reached in the numerical simulation within the dimensionless time 0.5 tD_r for paraffin, and 2.5 $\cdot 10^{10}$ tD_r for claystone. This is in good accordance with the evolutions of displacement profiles. The differences between the numerical results and the analytical solution are about 1% after the stationary velocity has been reached.

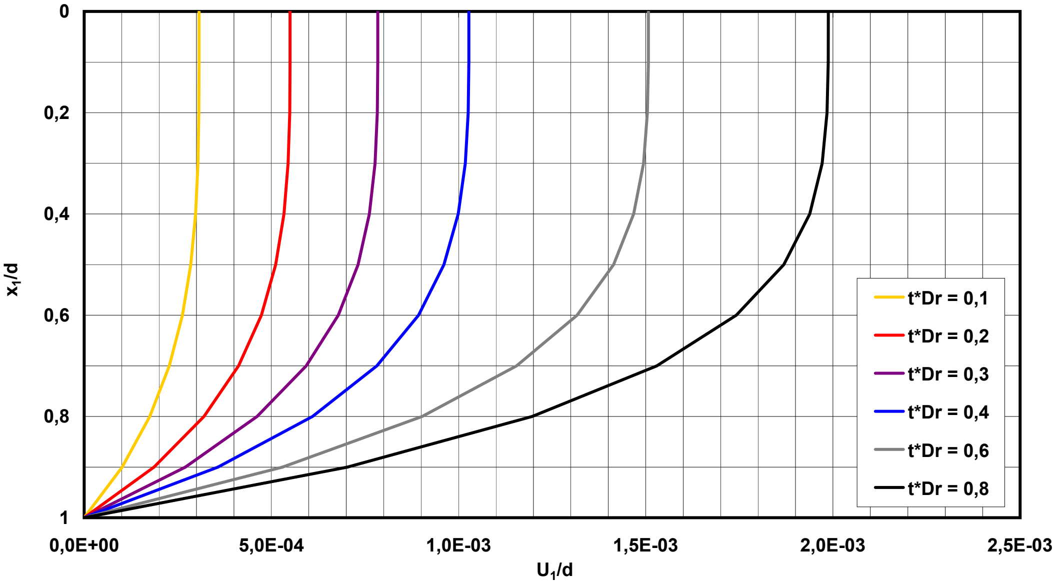

Figure 4.4: Evolution of displacements in direction of dipping

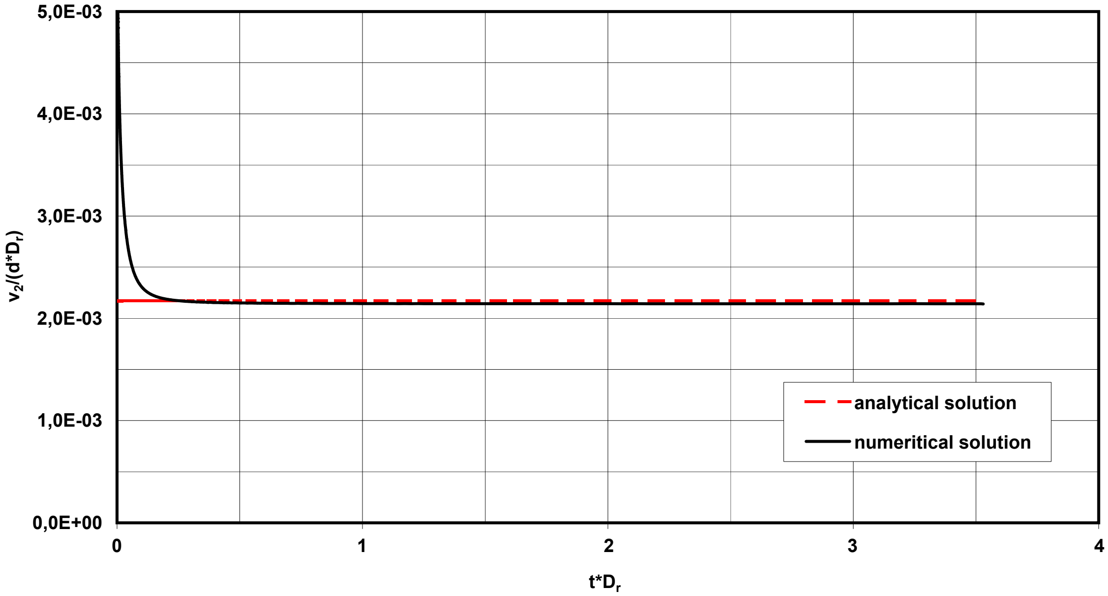

Figure 4.5: Evolution of the velocity at the surface

Fig. 4.6 shows velocity profiles from simulations for paraffin and for claystone in a vertical cross section perpendicular to the direction of dipping. The numerical results are in good accordance with the analytical solution. For claystone deformations are concentrated in a narrow band with a thickness of approx. $0.2d$ at the bottom of the slope, this is due to the high value of n.

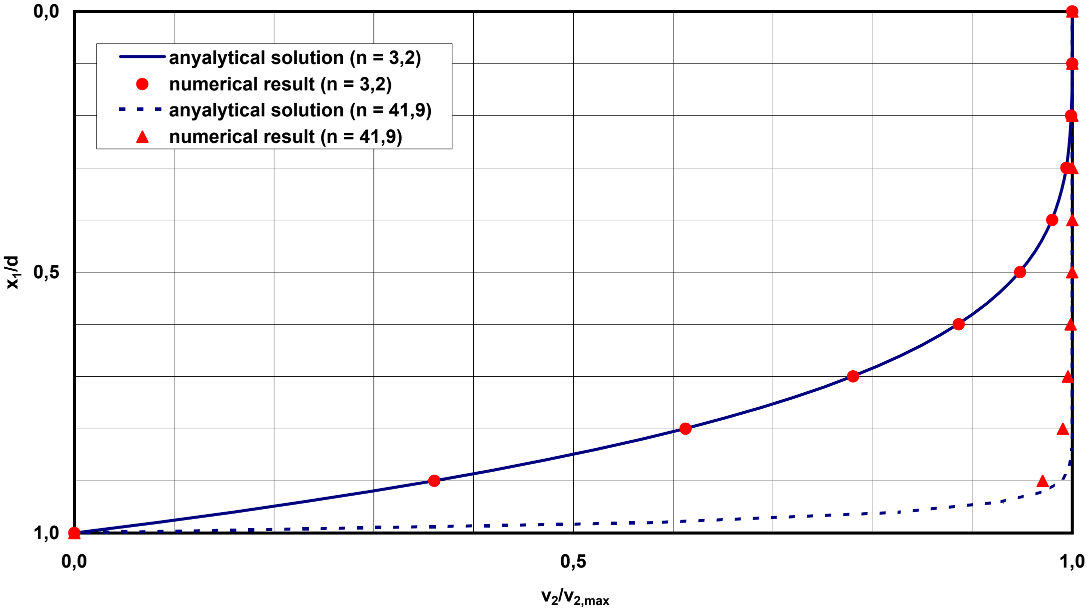

Figure 4.6: Velocity profiles in a vertical cross section compared to the analytical solution with n=3.2 (paraffin) and n=41.9 (claystone)

The evolution of the stress component T_{22} at different depths x_1/d and the constant stress components T_{11} and T_{12} are shown in Fig. 4.7. T_{33} is always equal to T_{11} and not shown. Therefore T_{11} and T_{12} remain constant with respect to time while T_{22} increases from its assumed initial value $T_{22} = K_0 T_{11}$ to $T_{22} = T_{11}$ which is reached asymptotically. As shown for the analytical solution 4.14 holds for a steady state. $T_{11} = T_{22} = T_{33}$ is reached asymptotically with the numerical calculations, thus the stress tensor provided by the numerical simulation agrees with the stress tensor from the analytical solution for a stationary velocity field. As (4.13) the numerical results reveal that T_{12} increases linearly with depth. $T_{22} = T_{11}$ is reached faster near the bedrock where the deviatoric stress is bigger. Near the surface $T_{22} = T_{11}$ has not been reached within the simulation period as the amount of shearing is too small.

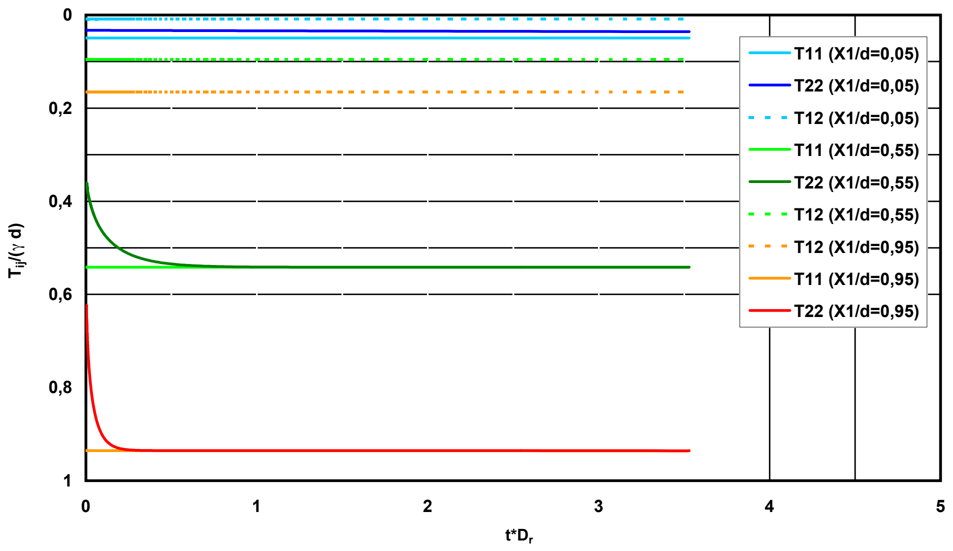

Figure 4.7: Evolutions of stress components at different depths

4.2.4 Discussion

Steady states of stress and velocity are assumed for the analytical solution and are reached in the numerical simulation after a transition. A steady state could as well be determined with affine displacement profiles which represent a steady state velocity profile. $T_{11} = T_{22} = T_{33}$ and $\dot{T}_{12} = 0$ result from the numerical simulation and with the analytical solution. Velocity profiles are parabolas of the order $n + 1$ with the maximum velocity at the surface and zero velocity at the bedrock. The velocity profiles for both solutions agree quite well.

A stationary stress state is attained independently of the assumed initial stress field. The initial stress components T_{11} and T_{22} may thus be assumed at will in simulations as they are swept out by subsequent creep. The assumed initial deviatoric invariant should be in the allowable range. The asymptotic stress is reached slower near the free surface of the slope due to low deformation rates.

Assumption (4.23) is justified for uniformly inclined layers which are far wider than thick. Thus, creeping layers may be substituted by a stack of uniformly sheared thin layers. Asymptotes of the stress- and velocity-field are attained with properly chosen boundary conditions and plane-parallelity. Initial states of stress- and velocity-fields should thus be assumed as those attained asymptotically by a system. Then, subsequent states are independent of arbitrary initial states.

This approach cannot strictly be validated with model tests or with observations in-situ. Inclined layers are always bounded laterally and in the direction of dip. They may be homogeneous in the laboratory, and plane-parallelity may then be achieved with smooth out-of-plane confining walls. However a steady state would require feeding the layer continuously uphill, and to remove it downhill with the same rate. This is hardly practicable in the laboratory. Field observations with a claystone slope by van den Ham [37] agree pretty well with the calculations outlined above.

4.3 Convergence of a circular borehole

4.3.1 Description of the boundary value problem

A finite-element model has been developed which enables simulations of the radial convergence of a circular borehole due to radial displacements in the far-field. It suffices to consider a cross section perpendicular to the axis of a borehole if one principal stress axis is parallel to it. Apart from the surface and apart from the top and the bottom of a homogeneous formation, the axial extension of the borehole may thus be considered as infinite. This simplification will be justified and delimited with more realistic boreholes in Chap. 5. Deformations occur only in the plane of the cross section, thus plane strain elements can be used. An initially orthotropic stress field has been assumed for the considered cross section. Initial values of internal stresses have been specified using the *INITIAL CONDITIONS option of ABAQUS. Due to symmetry, it suffices to model one quarter of the cross section (Fig. 4.8). Radially symmetric displacements are assumed at the outer boundary of the model, and a constant radial velocity v is applied to the nodes at $r = r_a$. Boundary displacements at the model edges may be radial, so radial displacements u_r are equal at all nodes for $r = r_i$. Thus, the shape of the model is kept radially symmetric, and the internal stress field can smoothly redistribute from its initial state due to viscoplastic deformation.

4.3.2 Numerical results

The simulation was carried out with material parameters of paraffin (Tab. 3.3). The simulation starts from an arbitrary, but orthotropic and initially *not radially symmetric* stress field with $\sigma_1 = 0.5$ MPa, $\sigma_2 = \sigma_1/3$ (Fig. 4.9). With continued deformation the directions of the principal stresses rotate in the considered cross section until a radially symmetric stress field is reached alongside with a nearly stationary state (Fig. 4.10). The principal stresses are radial and tangential. Fig. 4.11 and Fig. 4.12 show evolutions of

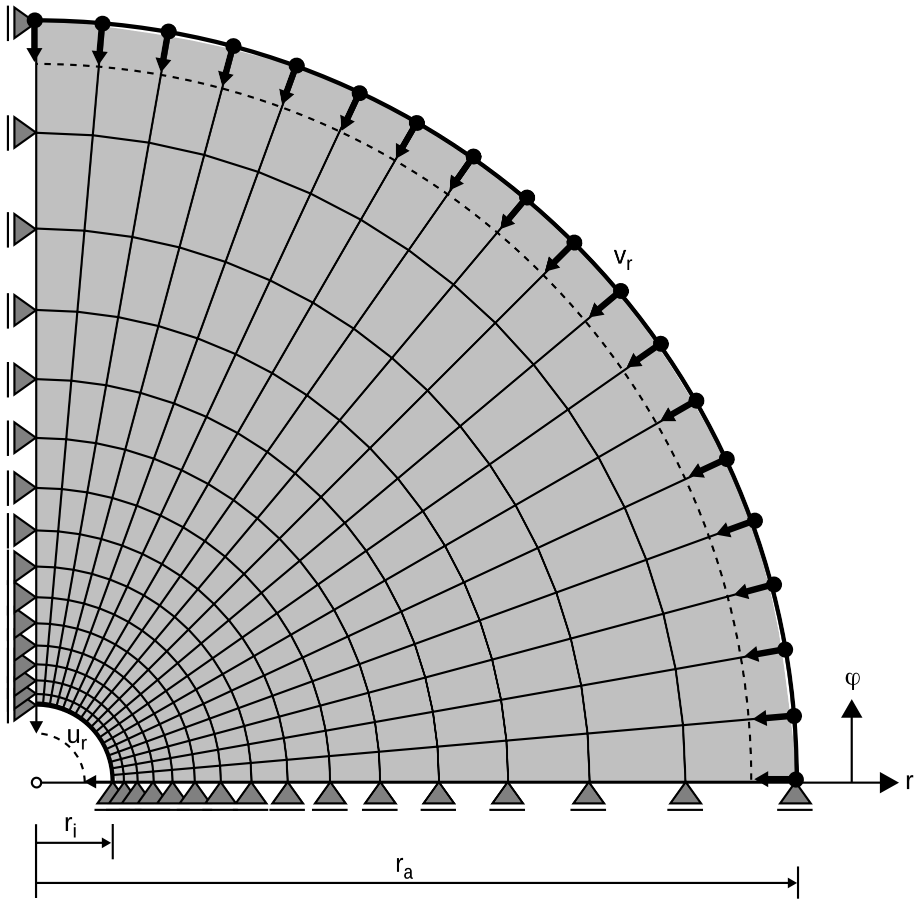

Figure 4.8: Finite-element model

the magnitudes of the maximum principal stresses SP_{max} and minimum principal stresses SP_{min} for different angles φ against the symmetry line at a constant radius $r/r_i = 1.08$ near the borehole. At the onset the magnitudes vary with the angle, but with continued deformation they reach the same asymptotic value after a time of about 2.5 10^{-3} tD_r for different φ.

Fig. 4.13 shows the evolution of radial convergence at $r = r_i$. Due to a constant radial velocity at $r = r_a$, the radial velocity increases continuously at $r = r_i$. The calculation results reveal that relative displacements u_r/r_i are small. Thus, geometrical effects may be neglected for the considered stress alignment.

Increasing radial velocity implies increasing strain rates in this direction. Thus the magnitudes of the principal stresses change with continued radial deformation, even if their principal directions remain. A stationary state cannot be attained in this boundary problem, but one can at least state that an initially not radially symmetric stress field leads to a radially symmetric one if the far-field and shape of the hole are kept radially symmetric.

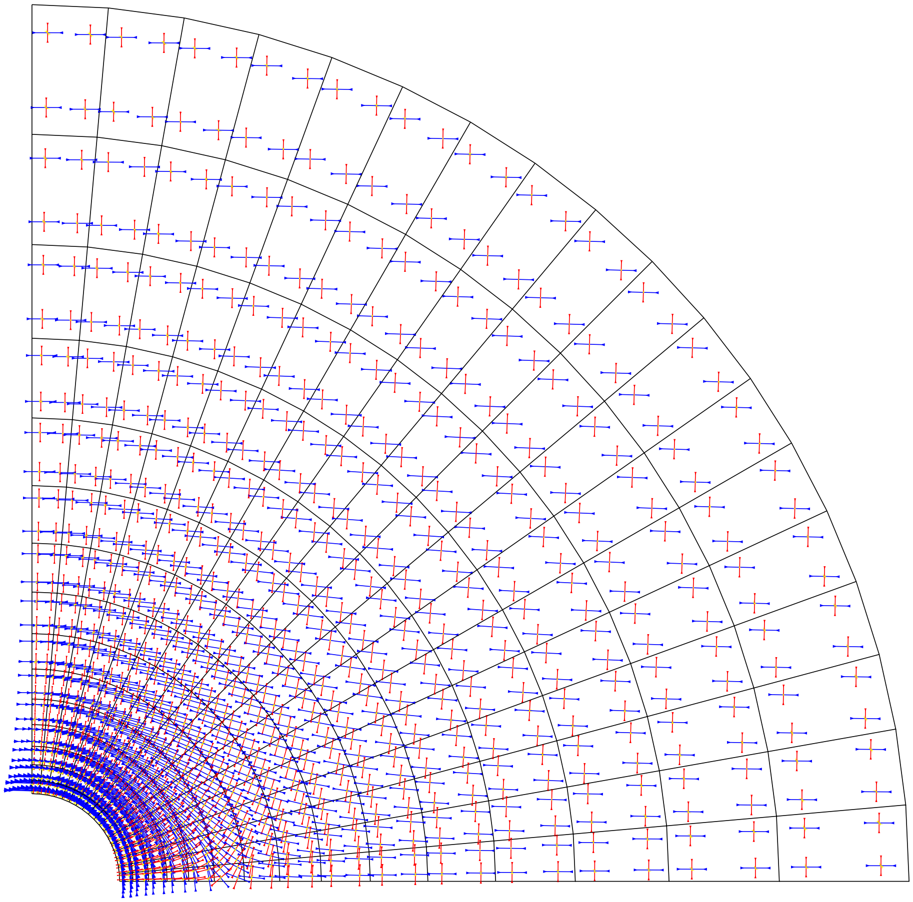

Figure 4.9: Assumed principal stresses at initial state (sign convention: pressure negative)

4.3.3 Discussion

The calculations show how radially symmetric fields can arise from orthotropic ones in a given depth near a converging borehole. For such an asymptote the outer boundary has to be guided so that it can move only in the radial direction. Two orthogonal symmetry planes have to be assumed. Only with the attained radial symmetry the asymptotic radial creep velocity can be estimated. Validation experiments with this symmetry could hardly be carried out. An actual ovalization of boreholes cannot thus be captured. A similar boundary value problem with radial expansion, instead of convergence, could more easily be validated with model tests and in-situ. Initial states of stress- and velocity-fields for numerical simulations should be assumed as those, that are attained asymptotically.

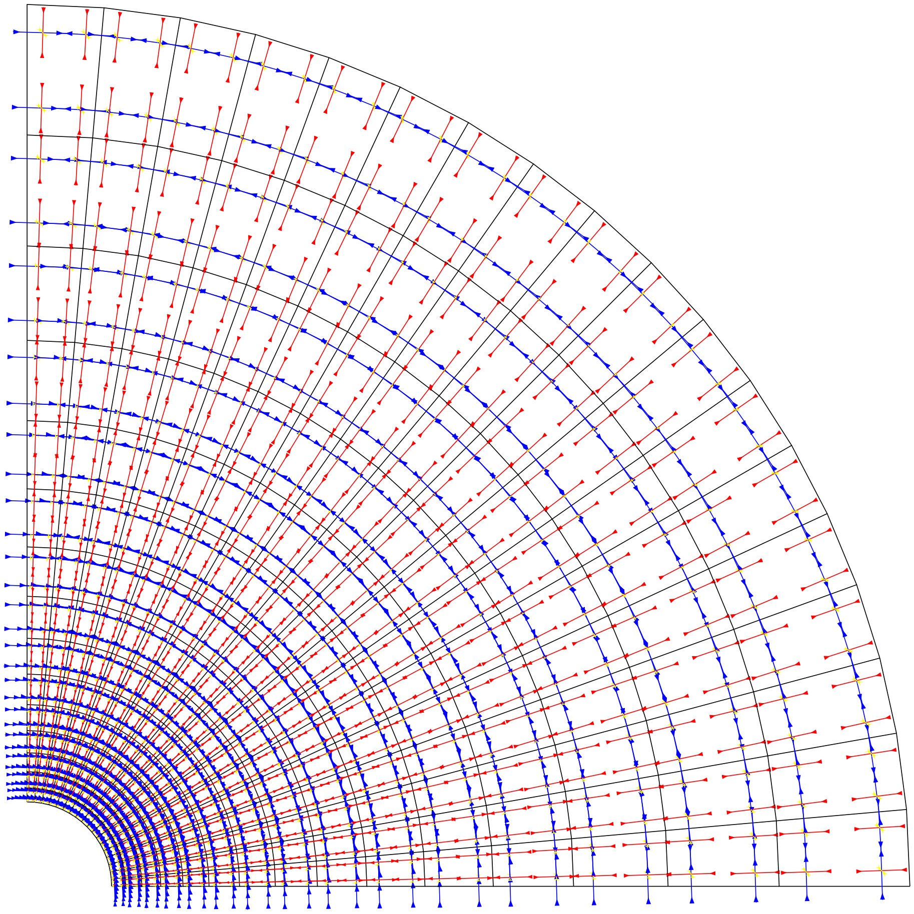

Figure 4.10: Maximum principal stresses (red) minimum principal stresses (blue) at stationary state (sign convention: pressure negative)

4.4 Conclusions

One-dimensional creep of a slope with an arbitrary allowable initial stress and velocity field leads asymptotically to a stationary field of velocity and stress. A radial convergence of a borehole with an initially not radially symmetric stress field leads to a radially symmetric field of stress if the shape of the hole is kept radially symmetric. After a radially symmetric field has been attained, the changes of radial pressure and displacement with time come close to the changes of deviatoric stress and strain of a representative element near the hole. Initial states of stress- and velocity-fields should be assumed as such distinguished states, that are attained asymptotically by a system. Then, subsequent states are independent of the initial one. Apart from the ovalization of boreholes the simplifying assumptions of radial symmetry is thus justified.

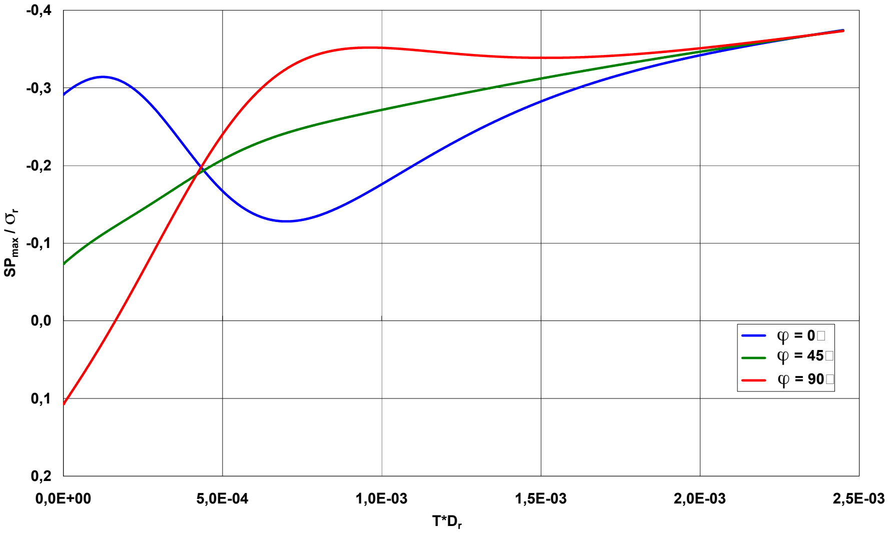

Figure 4.11: Evolution of maximum principal stresses at $r/r_i = 1.08$ and different angles φ (sign convention: pressure negative, $\sigma_r = 0.6$ MPa, $D_r = 2$E-4 1/min)

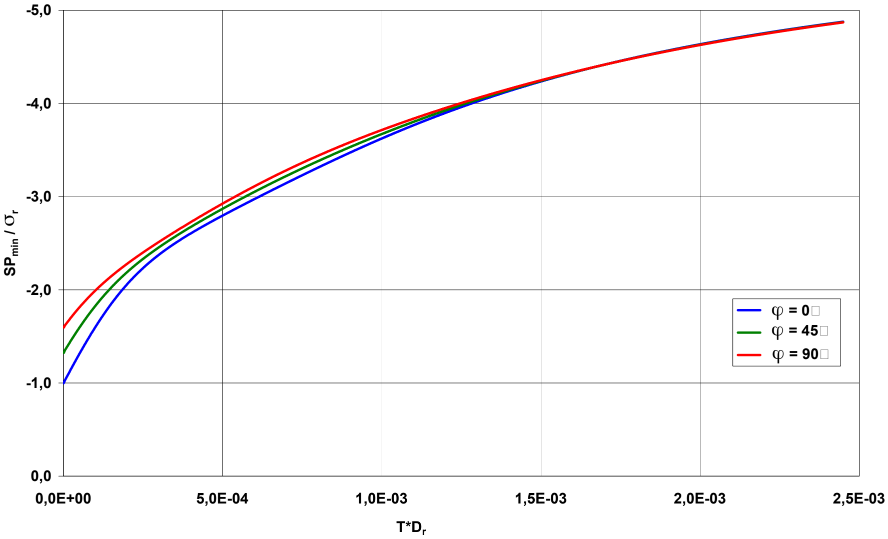

Figure 4.12: Evolution of minimum principal stresses at $r/r_i = 1.08$ and different angles φ (sign convention: pressure negative, $\sigma_r = 0.6$ MPa, $D_r = 2$E-4 1/min)

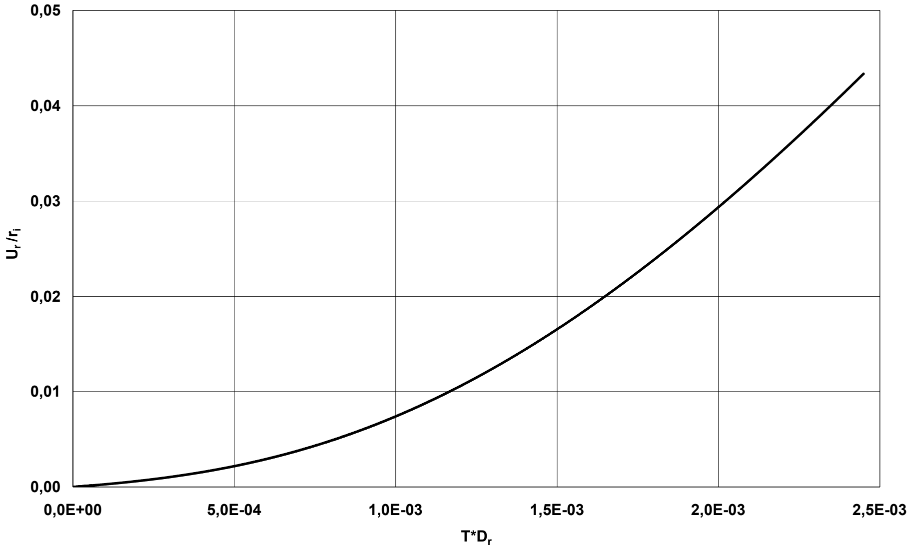

Figure 4.13: Simulated evolution of radial displacement at $r = r_i$

Chapter 5

Axisymmetric boreholes

5.1 Motivation and overview

This chapter deals with the gradual closure (a kind of creep) of axisymmetric boreholes in viscoplastic formations. Gradual closure is a considerable obstacle for the access to new reservoirs. A geothermal project located at the Upper Rheingraben has thus been realized with a cost overrun of more than two million Euro due to extended drilling periods, the total loss of already drilled sections and the loss of drilling equipment (drilling engines, cutter heads, drilling rods). Problems which can be observed with drilling indicate that sensitive formations consist of rock with markedly viscous behavior. Then small changes of deviatoric stress induce disproportionately high changes of deformation rates with these rocks.

The convergence of a vertical borehole has been studied with laboratory tests with novel testing devices and with a suitable model material. Additional laboratory tests have been carried out to determine elastic and viscous properties of the material. Large-scale convergence tests show the evolution of the deformation of a borehole which is induced by the dead load of the material. Small scale convergence tests exhibit the influence of deviatoric stress on the convergence velocity. Numerical calculations of the laboratory tests have been carried out. The numerical results have been compared to the results of the laboratory tests in order to validate the numerical model. The influence of the borehole bottom on the convergence velocity has been investigated with an axisymmetric model. Various numerical models of a horizontal cross section have been assessed with respect to accordance of the convergence with an axisymmetric model. The influence of supports (e.g. casings, linings) on convergence has been studied with a plane strain model of a horizontal cross section.

The master thesis of J. Eisenmann [6] arose in relation with this chapter and was intensively prepared and guided by the author. Some results of [6] are presented in this chapter.

5.2 Hydrogel

5.2.1 Motivation

The convergence rate of a wellbore is determined by its geometry and the viscosity and the stress field of the circumjacent rock formation. *Gradual closure* of boreholes in a ductile rock formation, which means considerable convergence rates without brittle fracture, occurs at depths and with stresses that can hardly be realized in a laboratory test and with all the physical properties of in-situ material. Thus, it is advisable to observe the convergence of boreholes in the laboratory with a model material. *Hydrogel* was found to be a suitable material for this purpose as it exhibits elastic and markedly viscous material properties. Convergence can be studied with hydrogel in the laboratory at moderate stresses which result from its weight. The absence of pores and thus the transparency of the material enables visual observation of the deformations of the borehole wall. The absence of pores also indicates independence of the deformation rates from the mean pressure which implies purely deviatoric creep.

5.2.2 Preparation

Gels are disperse systems of at least two components. Based on their surface interaction with water, one can differ hydrophobic gels (oleogels) and hydrophilic gels (hydrogels). Hydrogels consist of cross-linked polymers which are swollen in water. A hydrogel has been prepared for the laboratory tests based on the following components and quantities:

- 65% vol. demineralized water,
- 25% vol. polyethylen-30-cetyl-stearyl-alcohol (trade name: Emulgin B3),
- 10% vol. polyol fatty acids ester (trade name: Cetiol HE).

For the preparation of hydrogel from its particular components, the water is heated up to 80°C. Then the solid Emulgin chips and the liquid Cetiol are added and the mixture has to be stirred until it appears to be homogeneous. In order to avoid pores and inhomogeneities in the material, it is recommended to fill the warm fluid into a mould in which the gel, after solidification, has the definite shape required for the projected test. Subsequent handling of the material is difficult as imperfections of sample geometry can be induced already by touching it. The solidification of one liter gel takes approximately 18 h at room temperature. The suggested method enables the production of a sufficient number of samples with an identical, almost arbitrary shape and with identical material properties. Therefore, tests with this model material are well reproducible.

5.2.3 Material properties

Due to the absence of pores, solidified hydrogel is transparent. It is also achromatic at room temperature. These properties enable visual monitoring of the convergence of artificially generated cavities during a laboratory test.

Audible vibrations can be imposed to a hydrogel which has been solidified in a measuring cup with slight knocks on the cup without any visible remaining deformation. A groove can be scratched into the gels surface in order to carry out a laboratory test with a Casagrande device. This groove remains open after a hundred bounces of the cup of the testing device. Thus, it appears that elastic material properties dominate the material behavior with high deformation rates and small amplitudes. These elastic deformations occur without volume change [19]. The material constants E and ν of the elastic part of the constitutive equation (Chap. 3) have been determined by measurement of propagation delay of ultrasonic waves as described in detail in Chap. 2. The determined parameters are shown in Tab. 5.1.

Permanent deformation can be easily applied to a cylindrical sample with an unconfined creep test. At constant axial force, axial shortening s continues with time due to viscosity. The diameter of the sample increases with continued deformation as its height decreases, but the volume of the sample remains constant due to the absence of pores. The shape of the sample remains almost cylindrical during the test (Fig. 5.2 and 5.3). Slight bulging of the circumferential surface indicates some lateral confinement at the contact of the sample with the load plates. At constant axial force the axial stress σ decreases with continued axial shortening due to increase of the sample cross section (line (b) in Fig. 5.1). Thus, stationary creep can be reached with this test apart from the decrease of the axial shortening rate which results from the geometrical nonlinearity of the problem. On the other hand, the evolution of axial shortening (line (a) in Fig. 5.1) reveals that a sudden increase of the axial stress during the test induces a spontaneous shortening and leads to a disproportionately high increase of the axial shortening rate. Thus, the result of the unconfined creep test indicates that the material properties of hydrogel are a combination of elasticity and nonlinear viscosity.

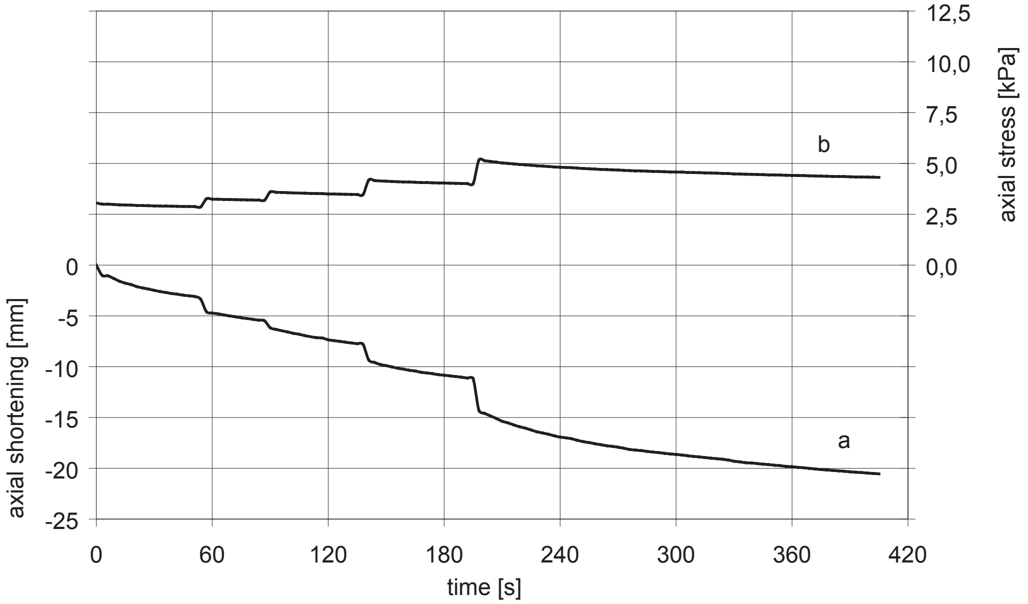

Figure 5.1: Evolution of axial shortening (a) and axial stress (b) at temporarily constant axial loading with an unconfined creep test with a hydrogel [6]

An unconsolidated and undrained confined compression test has been carried out in order to investigate the viscous behavior of hydrogel. The sample had a cylindrical shape with a diameter $d = 50$ mm and a height $h = 100$ mm. Thin non-adhesive interlayers have been inserted between the faces of the sample and the load plates of the testing device in order to minimize lateral confinement due to friction at the faces. A low confining pressure p has been preferred with respect to the planned convergence tests. Therefore, the triaxial test has been carried out with $p = 101.5$ kPa, which was the lowest constant confining pressure that could be controlled with the chosen testing device. The mean pressure p does not influence the deformation rate as long as the hydrogel is free of pores.

The test has been carried out with stages of temporarily constant axial shortening velocity. The test started with a reference velocity of $v = 0.1$ mm/min. In subsequent stages the axial deformation velocity was repeatedly varied by a factor of ten up and down (Fig. 5.4).

Since the sample is shortened, the axial shortening rate increases slightly with continued deformation at constant shortening velocity. A testing device which allows the control of axial deformation velocity depending on the actual height of the sample would be required for the performance of tests with exactly constant axial deformation rate. However, the increase of axial deformation rate with the carried out test can be regarded as negligible

Figure 5.2: Cylindrical shape of the hydrogel sample at the beginning of the creep test (h = 52 mm, d = 35 mm) [6]

with respect to the determination of viscous parameters.

Fig. 5.4 shows the axial shortening velocity v and the deviatoric stress response q in the unconfined compression test. The test results reveal a markedly nonlinear rate-dependence of the stress response. The material constants n and D_r for the viscous part of the constitutive equation have been determined in [6]. The results are specified in Tab. 5.1.

Table 5.1: Material constants of hydrogel [6]

G	ν	E	$\|\underline{D_r}^*\|$	$\|\underline{T_r}^*\|$	n
[MPa]	[-]	[MPa]	[1/min]	[kPa]	[-]
26.08	0.496	78.03	1.7 E-3	1.5	14.3

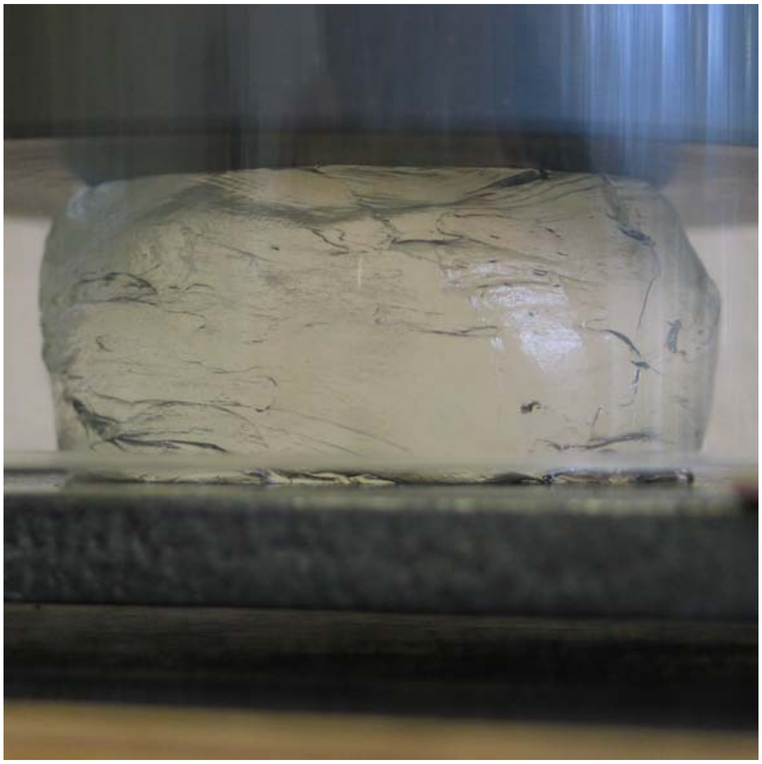

Figure 5.3: Shape of the hydrogel sample at the end of the creep test (h = 32 mm, d = 45 mm) [6]

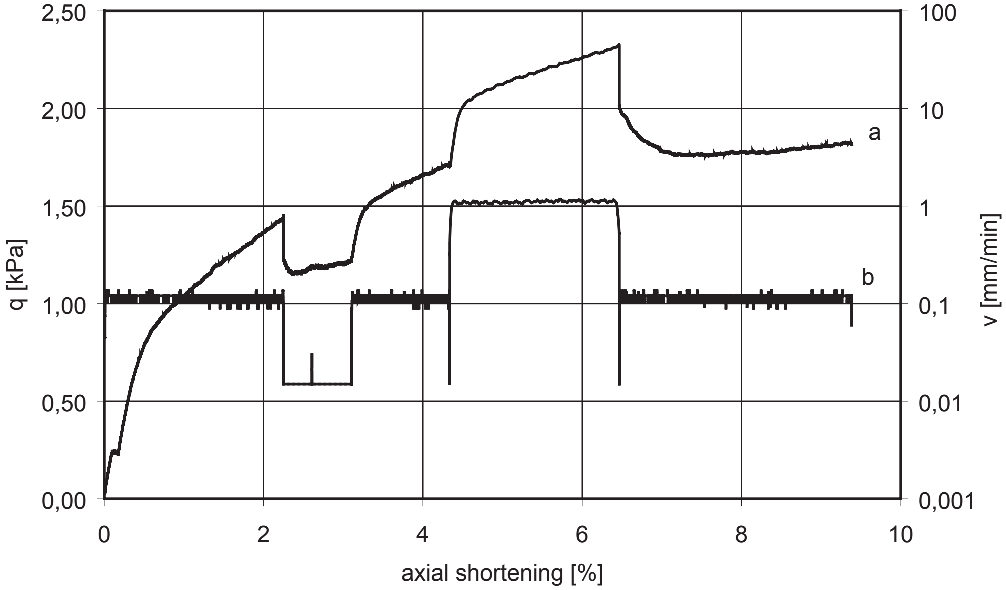

Figure 5.4: Evolution of deviatoric stress response (a) with various temporarily constant shortening velocities (b) in a confined compression test with hydrogel [6]

5.3 Experimental findings with convergence tests

5.3.1 Small-scale convergence tests

The convergence velocity of a borehole has been investigated with small-scale tests which have been carried out in a novel testing device (Fig. 5.5). The device consists of a cylinder of transparent acrylic glass. The cylinder has an internal radius of 54 mm and a height of 180 mm. It can be fixed with three screws on a removable bottom plate. An o-ring allows for a proper sealing of the cylinder and the bottom plate. Thus, it can be filled with liquid hydrogel. A hydrophobic release agent which is applied to the inner surfaces of the cylinder reduces the adhesion at the contact with the hydrogel. Silicone oil has been found to be a suitable medium for this purpose. After the device has been filled with warm, liquid hydrogel it takes approximately 18 hours at room temperature for solidification.
After solidification, a stiff load plate is applied at the top of the hydrogel. The load plate provides an even surface and uniform distribution of the vertical load. A circular opening in the center of the load plate allows for punching a vertical hole with a lubricated steel tube. The hydrogel inside the tube is removed with a spatula, then the tube is pulled out. A circular vertical borehole remains (Fig. 5.6).

Figure 5.5: Testing device for small-scale convergence tests [6]

A plug is inserted into the opening of the load plate. This avoids extrusion of the hydrogel

Figure 5.6: Circular vertical borehole at the beginning of a small-scale convergence test [6]

during the test. Air can exhaust through a small drill hole in the plug. Direct measurement of radial displacements inside the borehole is difficult to realize, but the evolution of the vertical displacement of the load plate indicates the convergence velocity of the borehole due to constant volume of the material. Readings of the vertical displacement are taken manually. Fig. 5.7 shows the operating testing device with attached caliper and clock.

The stress field due to the material's weight induced no visible convergence of the borehole wall, and no vertical displacement of the load plate could be measured within one hour. The vertical stress was increased by adding weights on the load plate. The evolution of the vertical displacement of the load plate and the corresponding vertical stress are shown in Fig. 5.8. An increase of the vertical stress leads to a disproportionately high increase of the velocity of the load plate. Tilting and jamming of the plate stopped its vertical movement at the end of the second stage for some time.

An axially symmetric convergence of the borehole can be observed during the test. Convergence of the borehole is enhanced by an increase of the vertical stress. This is also indicated by the measured vertical displacement of the load plate (Fig. 5.8).
Due to some remaining adhesion at the top and the bottom of the testing device, the borehole converged slower at these locations. Thus, the maximum convergence and the first closure of the hole have been observed in the middle third along the borehole axis

Figure 5.7: Operating testing device and convergence of the borehole during the small-scale test, [6]

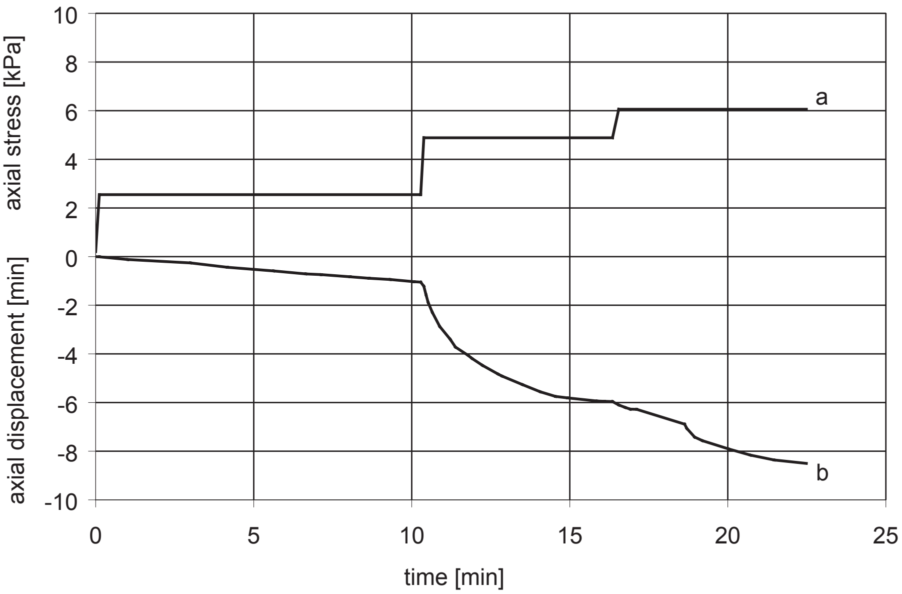

Figure 5.8: Evolution of vertical displacement(b) at various stress stages (a) in a small-scale convergence test, after [6]

(Fig. 5.9). From there the closure continued upwards to the top of the hole.

The closure of the borehole led to an entrapment of air in the lower part of the borehole (Fig. 5.10). Due to the different densities of hydrogel and air, the entrapped air rose slowly to the surface at room temperature.

Figure 5.9: First closure in the middle third section of the borehole in a small-scale test [6]

5.3.2 Large-scale convergence tests

A novel large-scale testing device has been developped in order to observe the evolution of the shape of a vertical borehole in a stress field that is initiated only by the material weight. The testing device consists of a cylinder of transparent acrylic glass with an internal radius of 225 mm and a height of 850 mm (Fig. 5.11). It is attached to a bottom plate with a rubber coating on its upper surface which allows for a proper sealing. Inside the cylinder the rubber coating is covered with a teflon sheet, and the wall of the barrel is coated with silicone oil in order to reduce adhesion at the contact with the hydrogel. Approximately 110 l of liquid hydrogel are required to fill the cylinder up to a level of 70 cm above the bottom plate. The hydrogel has been prepared and filled in quantities of 10 liters.

Experiences from the small scale-tests were used to improve some features such as the

Figure 5.10: Enclosed air at the bottom after closure of the borehole at the end of a small-scale convergence test [6]

vertical tracking of the tube for punching the hole. The radius of the tube is 37.5 mm. Thus, the surface contacting the hydrogel is much larger than in the small-scale test. Due to adhesion between the tube and the hydrogel a crane is required to pull out the tube. This method provides the required force for the uplift of the tube with a constant pulling velocity. The result is a vertical borehole with a smooth and circular surface (borehole wall).
Radial convergence of the hole can be measured with scales which are attached to a rod at its center. The scales are made of thin metal sheets which are cutting into the hydrogel during the convergence of the material. The transparency of the material allows for readings of the scales during the test. The scales had no visible influence on convergence. The hydrogel in the testing device has a free upper surface. Thus, any convergence of the borehole is caused only by the weight of the model material. A filled testing device for the large scale tests is shown in Fig. 5.11. The construction is similar to the small-scale testing device presented in Sec. 5.3.1, but its dimensions are much bigger. Thus, the handling of the testing device and the performance of the test is more difficult.

Tests have been carried out in order to study the influence of the bottom of the borehole on its convergence. A borehole with a depth which amounts half of the height of the hydrogel was punched (Fig. 5.12). Axially symmetric convergence started immediately

Figure 5.11: Testing device filled up with hydrogel [6]

after the punching tube was pulled out (Fig. 5.13). The borehole converged until its total closure within approximately half an hour (Fig. 5.14). Due to the stabilizing influence of the bottom of the hole, the convergence velocity of the borehole wall appears to be the highest at approximately one or two diameters above the borehole bottom. Thus, the first closure has been observed also at this section. Starting from this location, the closure continued upwards to the surface where a subsidence mould was observed (Fig. 5.15).
Fig. 5.16 shows the evolution of convergence in two tests. The radius of the boreholes was measured at the same depth, approximately two diameters above the bottom of the hole. The observed evolution indicates that the boreholes converge with approximately constant velocity. The evolution until closure is similar for both tests. Thus, the test appears to be reproducible.

Figure 5.12: Testing device with tube and measurement system [6]

5.3.3 Discussion

The convergence of boreholes induced by different stress fields can be studied with convergence tests up to their total closure. Novel devices have been developped for small-scale and large-scale tests. Small-scale tests exhibit a significantly nonlinear influence of different stess fields on the convergence velocity. Large-scale tests allow for studies of convergence with a stress field that is induced by the weight of the material. With large-scale tests the evolution of convergence exhibits the retarding influence of the borehole bottom. Due to the good reproducibility of the model material, convergence tests are reproducible. However, the preparation of the hydrogel in small quantities may lead to some inhomogeneity of the material properties. Thus, the preparation of hydrogel in large quantities has to be preferred in order to avoid inhomogeneities and to provide reproducible tests.

Small geometrical imperfections, such as an initially slightly ovalized surface of the borehole or a borehole axis which is not perfectly straight, appear to have a significant influence on the evolution of convergence. Geometrical imperfections may locally induce an increased or reduced convergence rate which can result in unsymmetric convergence.

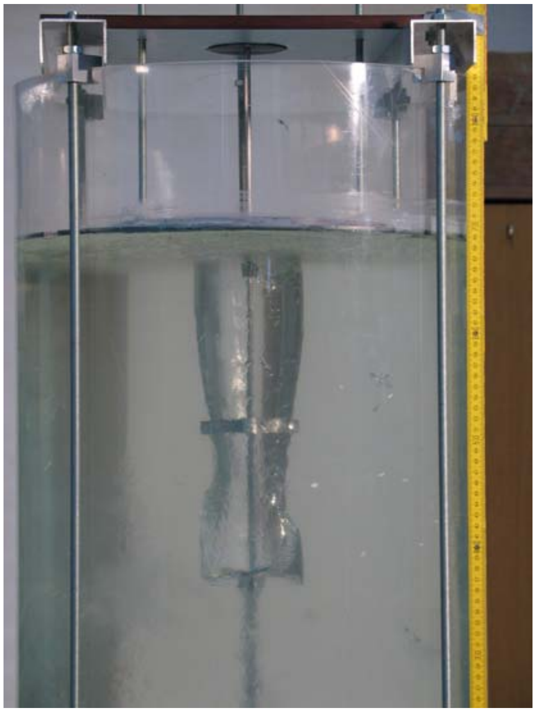

Figure 5.13: Deformation of the borehole immediately after removing the punching tube [6]

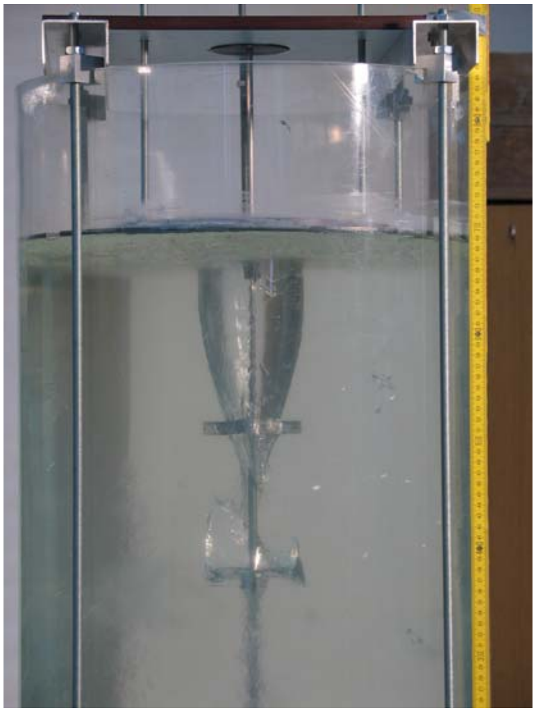

Figure 5.14: Closure of the borehole [6]

Figure 5.15: Subsidence mould

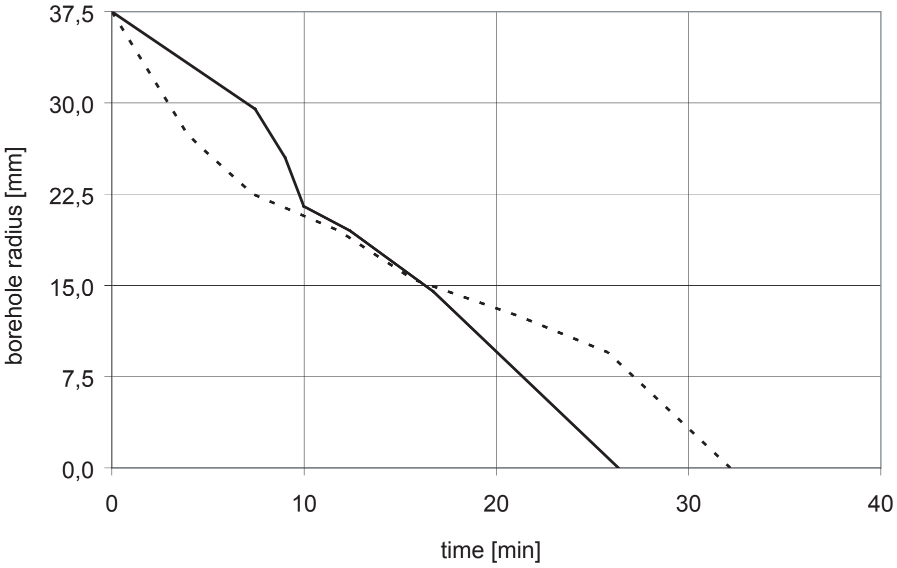

Figure 5.16: Evolution of the borehole radius, two diameters above the bottom, in two large-scale convergence tests [6]

Eccentric loading of the upper surface of the hydrogel can lead to tilting and jamming of the load plate and to a stick-slip downward movement.

5.4 Numerical simulations

5.4.1 Small-scale convergence tests

The small-scale test of Fig. 5.3.1 was modeled by means of FEM [6]. The numerical model can thus be validated with the results of the laboratory tests. An axially symmetric model is used for the simulation. A vertical cross-section along the borehole axis suffices for the spatial discretization of the test. Assembly dimensions of the numerical model, boundary conditions and simulated time steps are analogous to the laboratory test described in Sec. 5.3.1. Principal sketches of the laboratory test and the numerical model are shown in Fig.5.17.

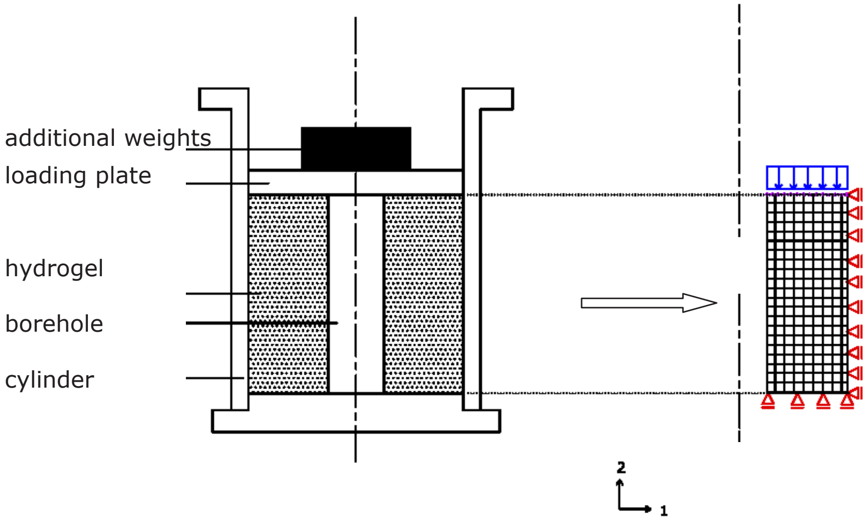

Figure 5.17: Principal sketches of the laboratory test, and a finite element substitute, after [6]

The weight of the hydrogel is modeled by means of the material density and the gravity field. An additional pressure at the upper surface of the gel is induced by the dead load of the load plate and applied weights. This additional pressure is modeled as a distributed load at the upper surface of the gel. The stiffness of the load plate is taken into account by assuming uniform displacements of the nodes at the upper surface.

The excavation of the vertical hole can be simulated with different modeling techniques. One technique is to discretize the entire cross section of the gel with continuum elements (Fig. 5.18a). After a geostatic equilibrium step with an initial stress field (which is compatible to the gravity-induced stress field) the elements within the borehole geometry are removed (Fig. 5.18b). The borehole is now free to converge. Another technique is to discretize the cross-section of the gel except for the area of the borehole, and to fix the surface of the borehole with radial constraints (Fig. 5.18c). After a geostatic equilibrium step the constraints are removed and the borehole is free to converge (Fig. 5.18d). These two techniques have been compared in [6] and have been found to lead to the same result. The modeling technique with a removement of elements has been chosen for the numerical simulation of the convergence tests.

The following assumptions have been made for the boundary conditions:

- The acrylic cylinder is undeformable, thus the radial displacement of the vertical boundary of the model is constrained.
- There is always contact between the cylinder and the hydrogel, contact separation is not allowed.
- There is no friction at the contact between cylinder and hydrogel. Thus, a parallel displacement of the hydrogel relative to the vertical boundary is not constrained.
- The stiff load plate enforces uniform vertical displacement of the upper surface of the gel. The load plate itself is not discretized as the uniform displacement can be modeled by defining the mutual displacements of the surface nodes to be zero in the axial direction.
- The bottom of the model is fixed in the axial direction due to the undeformable bottom plate in the test.
- Radial displacements at the bottom boundary of the hydrogel have been varied and adapted according to the observations during the laboratory tests.

First, the assumption has been made that the contact of the hydrogel with the bottom plate of the testing device is free of adhesion due to wetting with silicone oil. Thus, the displacements at this location have been constrained only in the axial direction, the radial direction remained free. However, the deformed shape of the borehole in the numerical simulation differs significantly from the shape observed during the laboratory test. In the numerical simulation the convergence increases steadily with increasing depth (Fig. 5.19), whereas during the laboratory test the maximum convergence has been observed in the

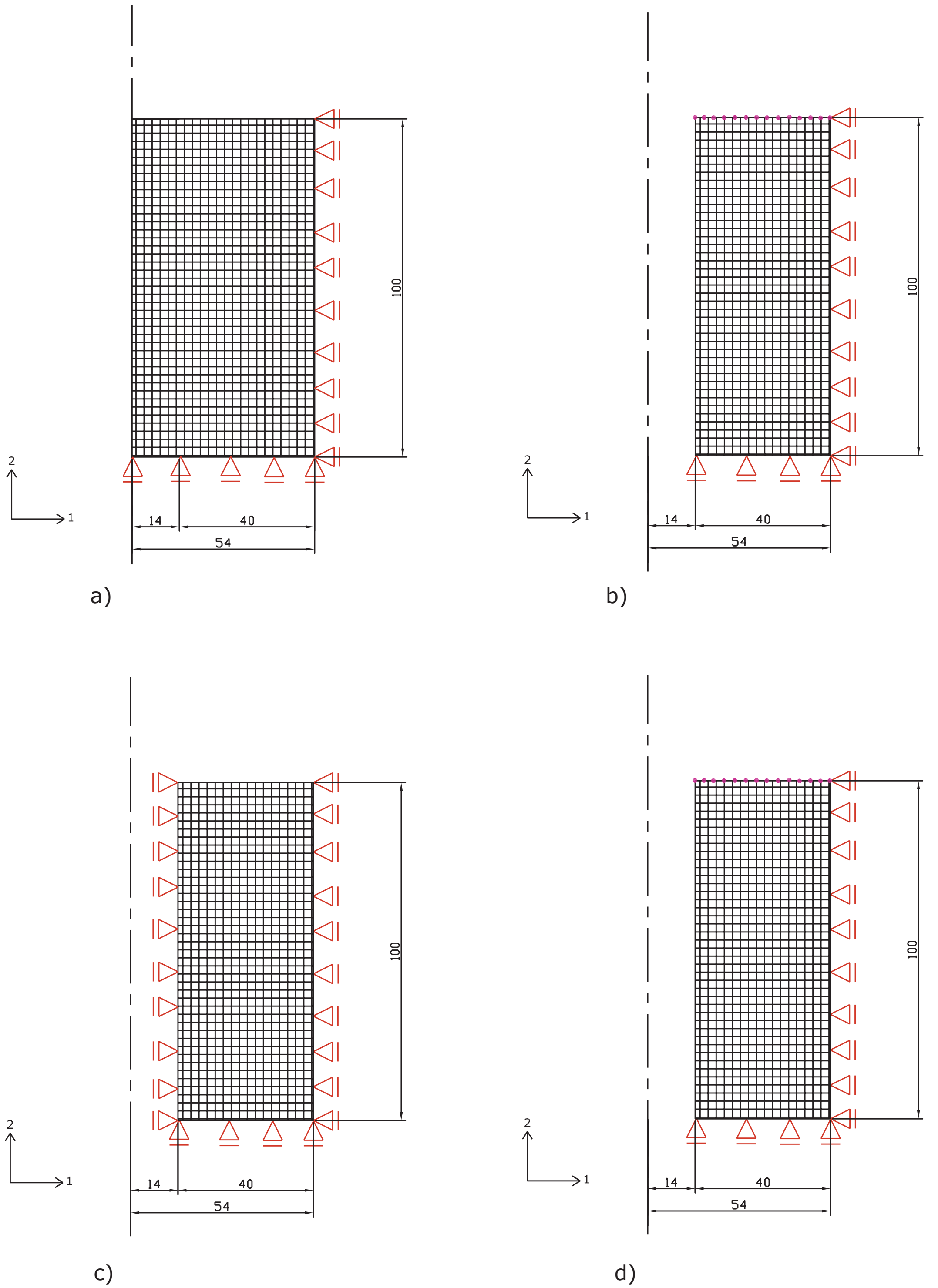

Figure 5.18: Modeling techniques for borehole excavation, [6]

middle third of the boreholes axis. Thus, the numerical simulation indicates that wetting of the bottom plate with silicone oil did not completely eliminate adhesion at the contact with hydrogel.

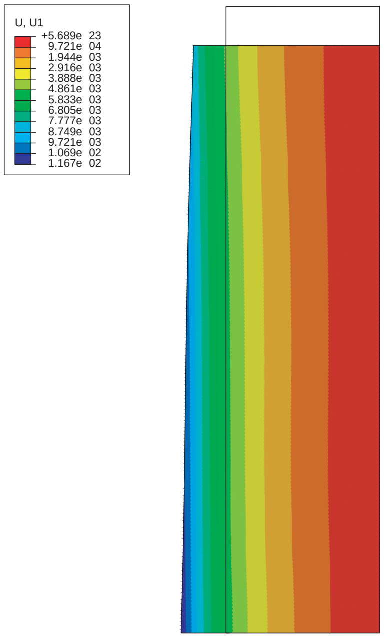

Figure 5.19: Radial displacement with unconstrained lower boundary at the end of the simulated test

Subsequently, the boundary displacements have been constrained also in radial direction, which corresponds to the observed convergence of the borehole bottom during the test. The modified boundary conditions lead to a coinciding shape of the deformed borehole with the test (Fig. 5.20a) and the numerical calculation (Fig. 5.20b). Fig. 5.20 illustrates that, according to the test results, the maximum convergence evolves approximately two to three diameters above the borehole bottom.

The evolution of axial displacement of the load plate in the numerical simulation resembles the evolution in the test. However, the rate of axial displacement (slope of displacement curve in Fig. 5.21) during the first loading stage is lower than in the test. At the beginning of the second loading stage the rate of axial displacement is higher than in the test, but at the end of the stage the displacement vs. time curves appear to run parallel. At the beginning of the third loading stage the results of the numerical simulation and the laboratory test are not comparable. The measured axial displacement during the test shows a rather discontinuous evolution due to tilting and jamming of the load plate which

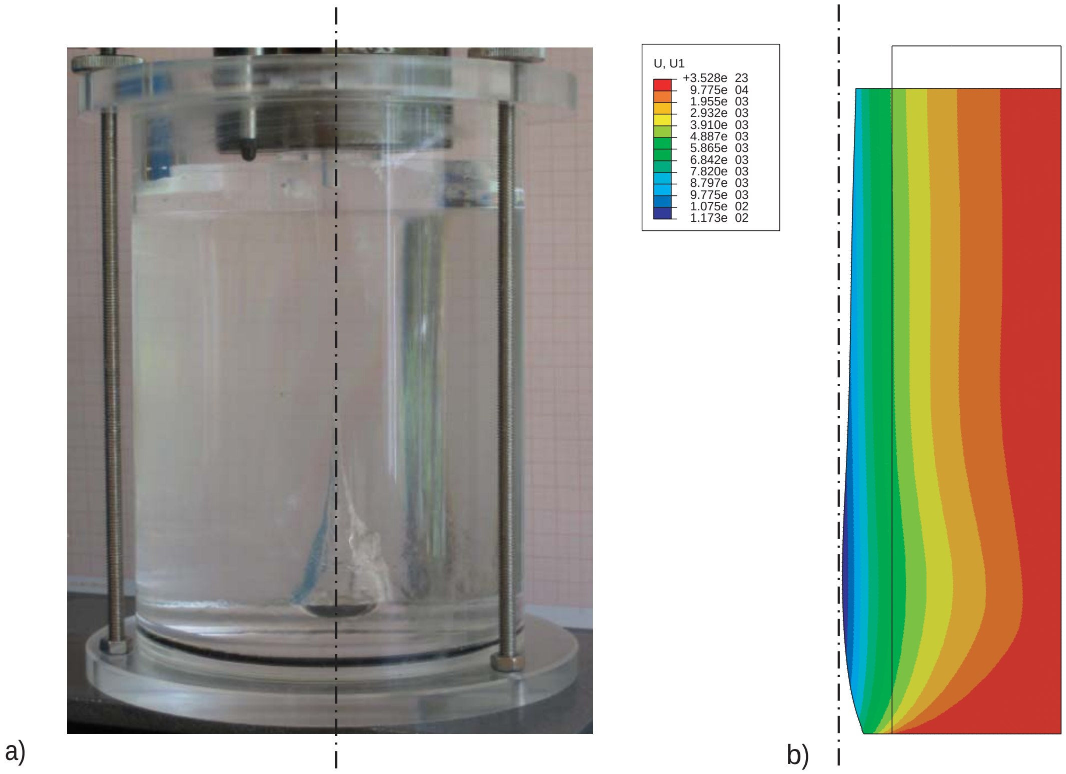

Figure 5.20: Radial displacement with constrained lower boundary at the end of the simulated test, after [6]

cannot be accounted for in the axially symmetric numerical model. Nevertheless, at the end of this stage the displacement vs. time curves appear to run parallel again.

The results of the numerical simulation are thus in good accordance with the test results. Differences of the axial displacement rate indicate a frictional contact between the load plate and the inner surface of the cylinder. This can lead to tilting if the friction is not axisymmetric. Thus, an improvement of the axi-parallel bearing of the load plate is recommended for the performance of further tests.

5.4.2 Supporting effect of the borehole bottom

The supporting effect of the borehole bottom has been investigated with an axisymmetric model also in [6]. A free surface is modeled, thus deformation is induced only by weight. The subsequent own calculations are carried out with material constants of hydrogel. Other materials could also be considered with the same models. Starting from a geostatic initial state, a borehole is modeled the depth of which amounts half of the model height (Fig. 5.22). The subsequent calculation step allows for convergence of the borehole.

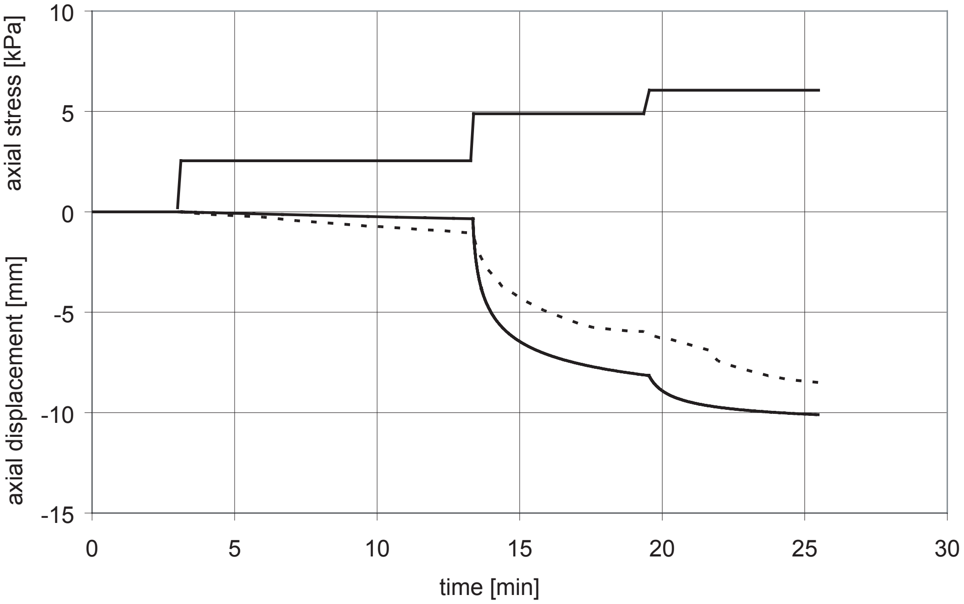

Figure 5.21: Evolution of axial displacement of the load plate with the numerical simulation (solid) and laboratory test (dashed), after [6]

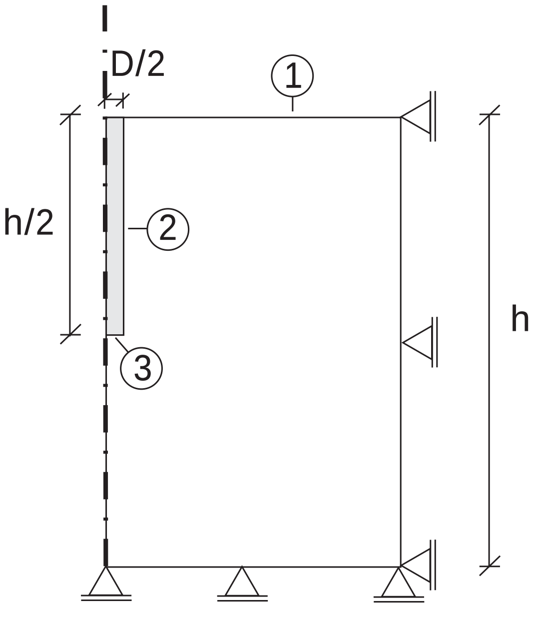

Figure 5.22: Axisymmetric model for investigation of the influence of the borehole bottom on convergence, (1) free surface, (2) borehole wall, (3) borehole bottom, after [6]

Fig. 5.23 illustrates the evolution of radial displacements of the borehole wall. The results of the numerical simulation indicate that the maximum convergence is located approximately one diameter above the borehole bottom. This result is in good accordance with the observations of the large scale convergence test.

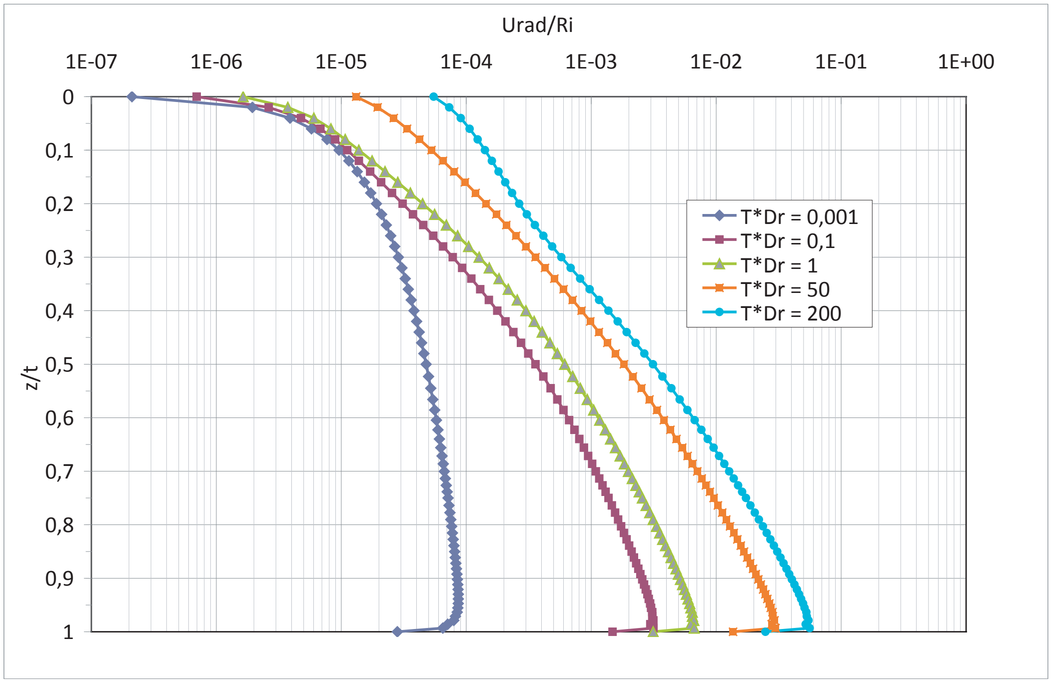

Figure 5.23: Evolution of radial displacements of the borehole wall

Fig. 5.24 shows the evolution of radial displacement at the location of maximum convergence. The result indicates that the rate of convergence (slope in Fig. 5.23) is decreasing with continued deformation. This occurs also with the vertical heave of the center of the borehole bottom (Fig. 5.25).

Fig. 5.26 shows the deviatoric stress immediately after the excavation (a) and at the end of the calculation (b). It appears that a maximum deviatoric stress is induced approximately one diameter above the borehole bottom. This is in good accordance with the location of maximum convergence. The evolution of deviatoric stress shows that the deviatoric stress induced by the excavation is reduced by viscous redistribution of stress. This leads to a decreasing rate of convergence.

5.4.3 Estimation of convergence with horizontal cross sections

Axisymmetric models provide a good estimation of the convergence of vertical boreholes. *Horizontal cross sections* of vertical boreholes at a constant elevation (depth) enable a

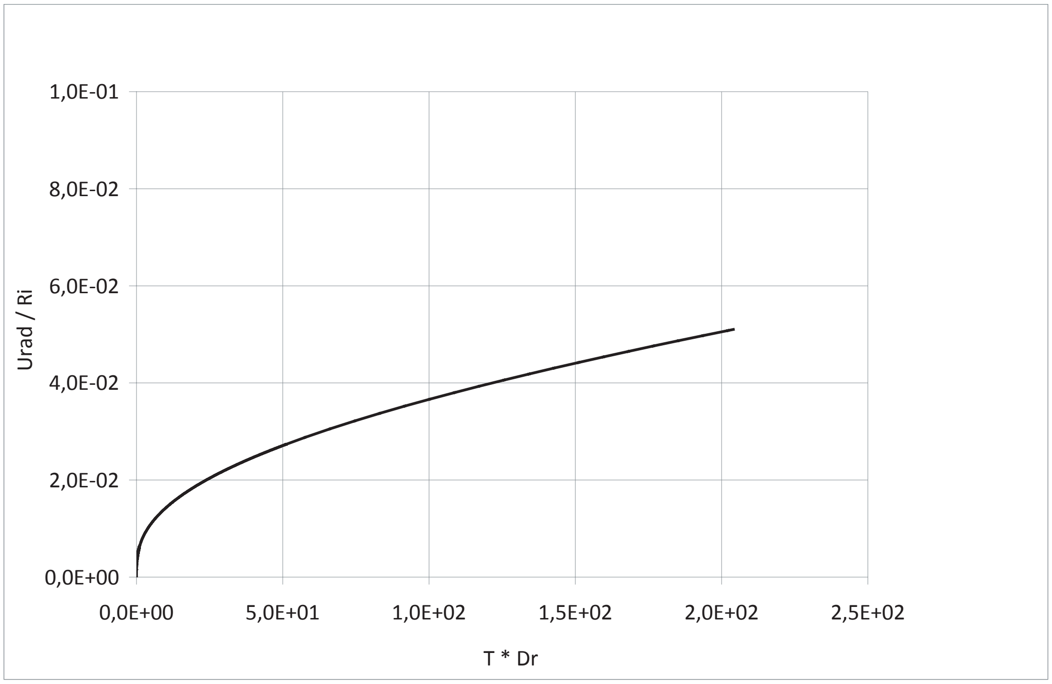

Figure 5.24: Evolution of radial displacements at the location of maximum convergence

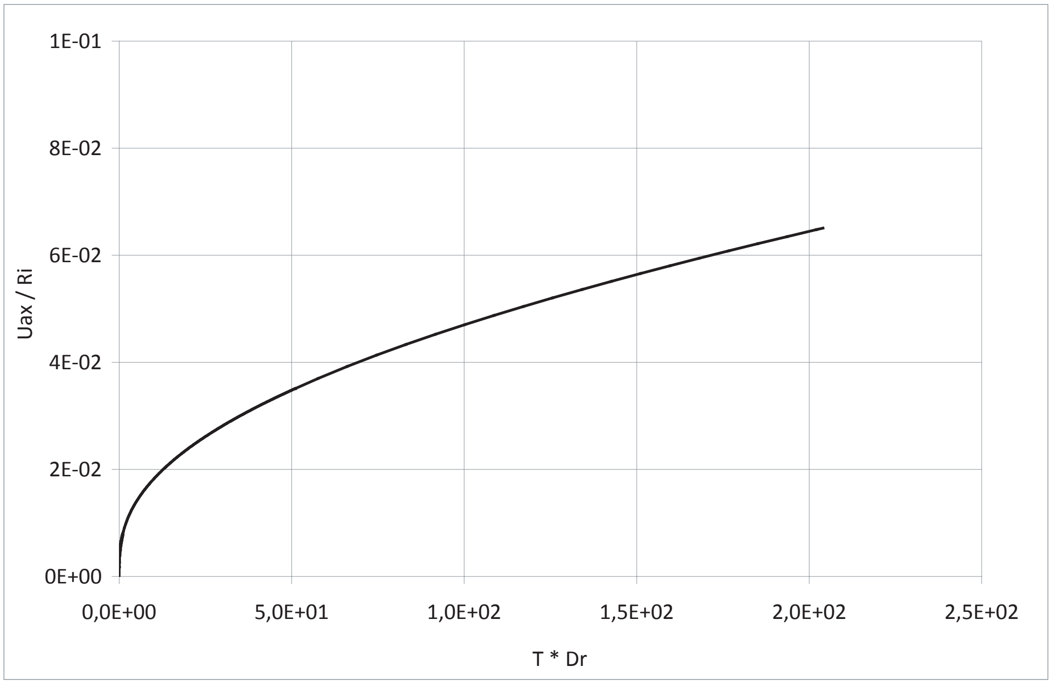

Figure 5.25: Evolution of axial uplift of the center of the borehole bottom

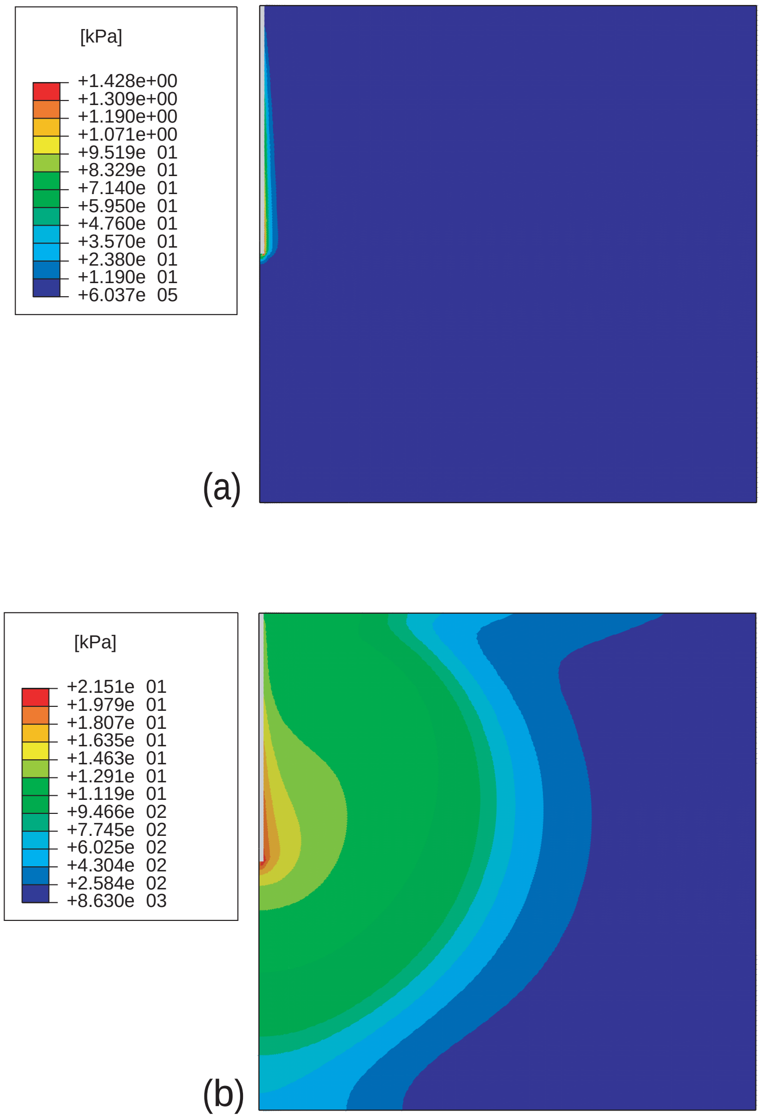

Figure 5.26: Deviatoric stress immediately after the excavation (a) and at the end of the calculation (b)

further reduction of the complexity of numerical modeling, in particular with deep boreholes. However, information about the distribution of convergence along the borehole axis is not available with models of horizontal cross sections.

Modeling of a horizontal cross section at constant depth (e.g. at the approximate location of maximum convergence) implies the assumption that the borehole bottom has negligible influence on the stress field at the cross section. It also implies that the formation can be considered as homogeneous in the vicinity perpendicular to the modeled plane, i.e. that the variations of material properties (e.g. boundaries of rock layers) are of negligible influence on the stress field at the cross section.

The axisymmetric model (Sec. 5.4.2) provides a reference base for the evolution of convergence along the borehole wall. The changes of axial shortening (Fig. 5.27) and the changes of the axial stress component (Fig. 5.28) during the calculation of the axisymmetric model reveal that neither the assumption of plane strain conditions nor the assumption of constant axial pressure is correct. Nevertheless, plane strain models and models with an axisymetric disk have been studied and compared with respect to their suitability for a crude estimation of convergence with models of a horizontal cross section at the location of maximum convergence in the axisymmetric model.

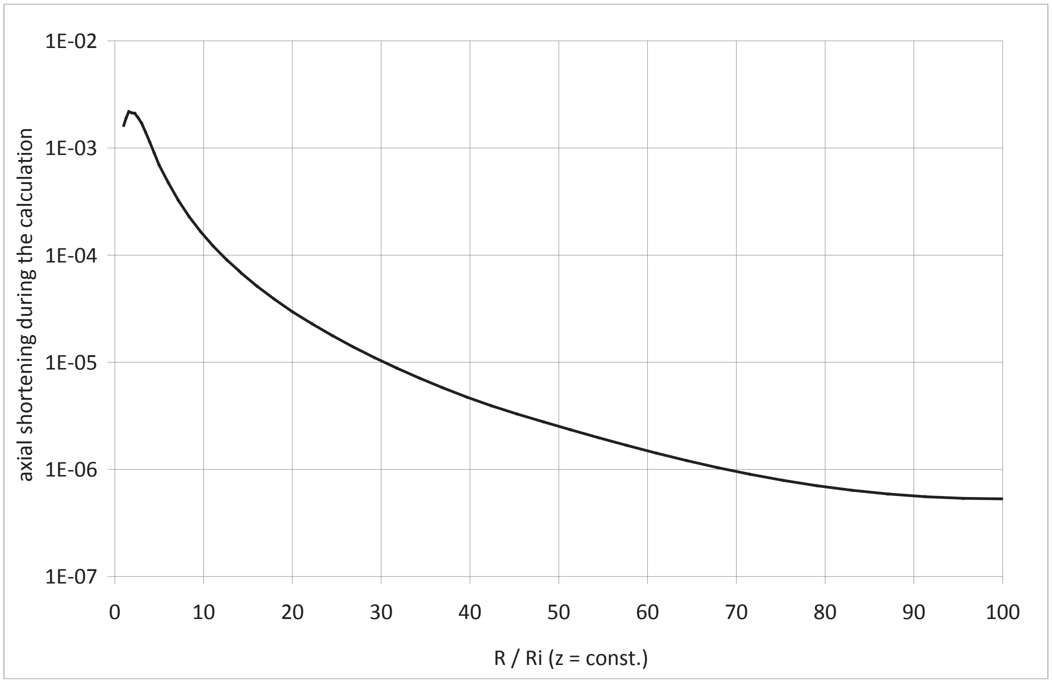

Figure 5.27: Changes of axial shortening during the calculation

Horizontal cross sections of a borehole at constant depth are often modeled with plane strain condition which is characterized by the assumption that out-of-plane stains are zero. (Note: The out-of-plane stress component is non-zero in the plane strain model and corresponds to the vertical stress of a horizontal cross section. Nevertheless, out-of-plane stress components can be only conditioned (user-defined) in the initial state of the calculation. In-plane displacements during the calculation induce rearrangements of the in-plane stress field. But this causes also changes of the out-of-plane stress components due to plane strain condition. The out-of plane component of total strain is zero by definition. Nevertheless, the elastic and viscous fractions of total strain can be non-zero.) Plane strain modeling allows for discretization of a horizontal cross section with two-dimensional finite elements. Compared with three dimensional finite elements (with the same geometrical order) the number of degrees of freedom and the number of integration

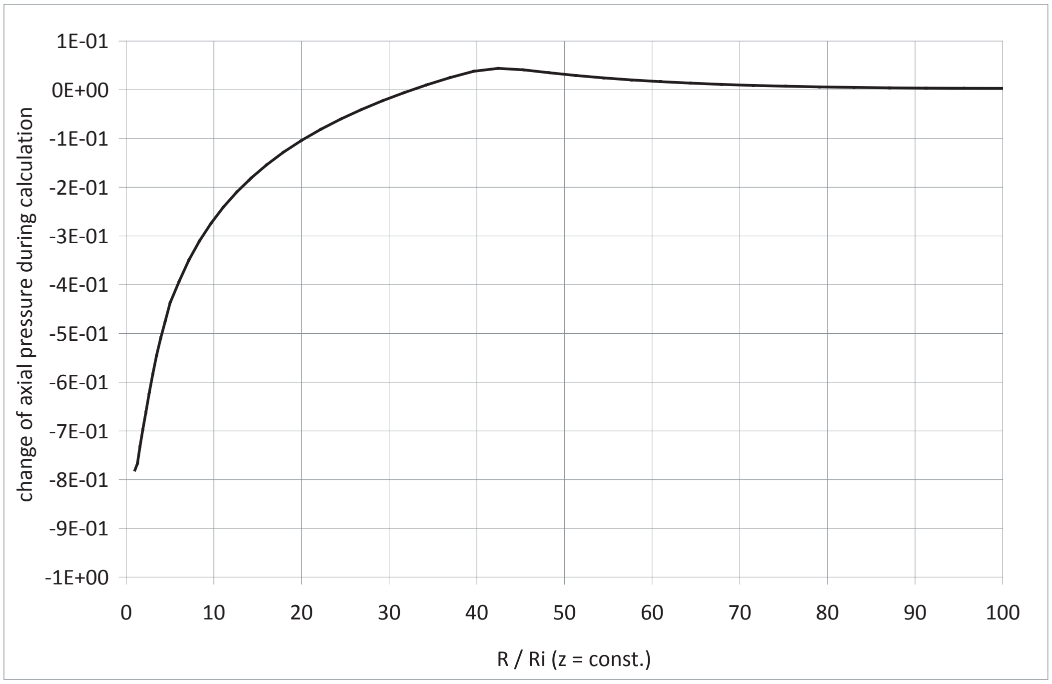

Figure 5.28: Changes of axial stress component during the calculation

points per element are reduced, thus the required calculating time is significantly shorter. Discretization of one quarter of the cross-section suffices due to symmetry of the problem (Fig. 5.29). Tangential displacements at the symmetry axes are constrained. The outer boundary (far-field) can be either radially constrained (a) (which is in accord with the axisymmetric model of Fig. 5.4.2 and for the undeformable cylinder of the testing device), or a constant horizontal pressure is acting (b) (which assumes that the far-field stress is not influenced by the borehole). Alternative modeling can be carried out with a horizontal disk of axisymmetric elements and the assumption that a constant vertical load is acting at the cross section. Fig. 5.29 shows principal sketches of the model. According to the plane strain models, the boundary conditions at the far-field can be either radially constrained (c) or unconstrained with constant radial pressure (d).

These four alternative models have been studied and compared with the results of the axisymmetric model outlined in Sec. 5.4.2. The numerical simulation starts with all models from an isotropic stress state which complies with the initial stress field at the constant depth of the considered cross section. The excavation, respectively the drilling process, is modeled by removing the stress at the borehole wall.
Fig. 5.30 shows the evolution of the calculated convergence. The results reveal that, compared with the results of the axisymmetric model, the plane strain model with constrained outer boundary (a) underestimates the convergence. The calculation result indicates that

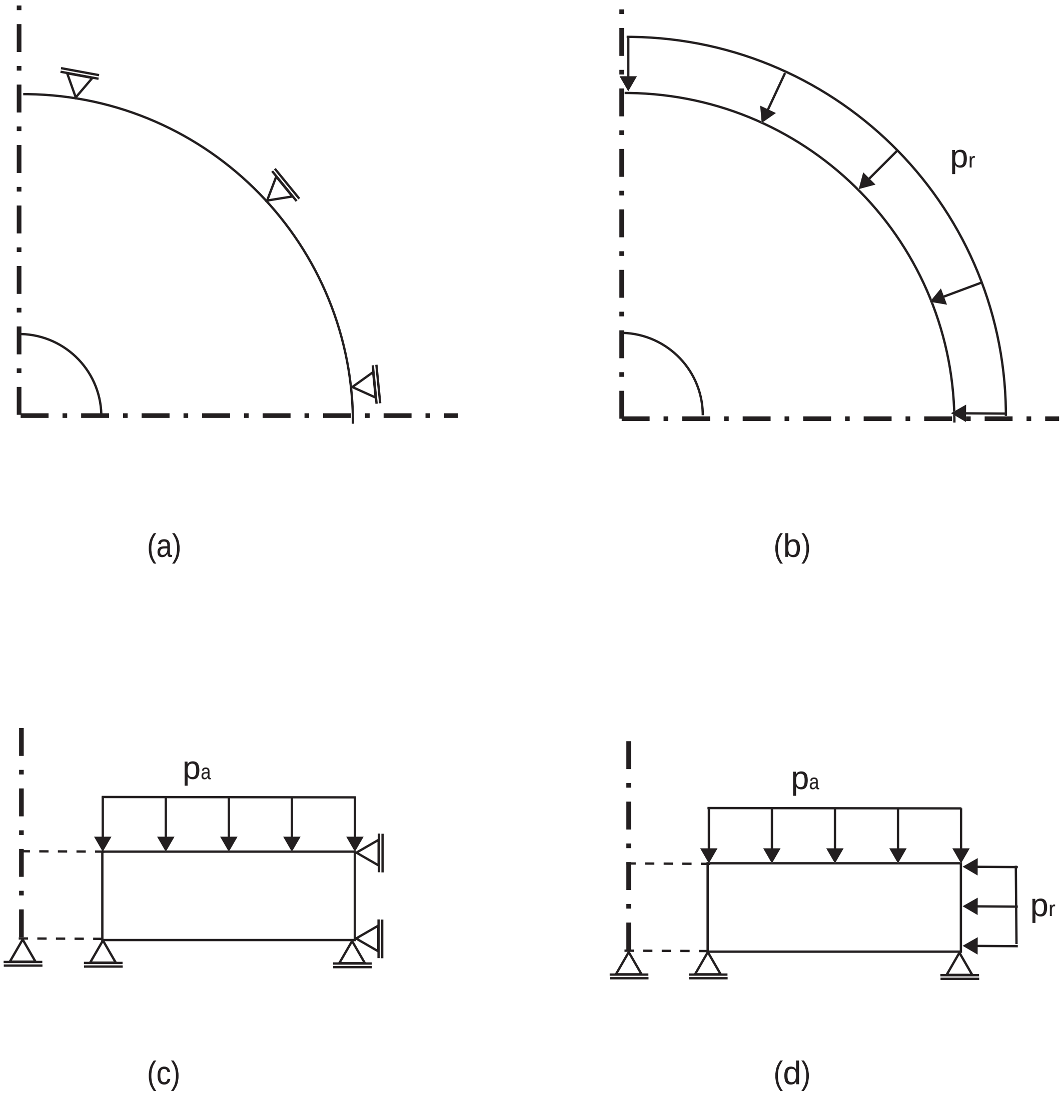

Figure 5.29: Alternative models for horizontal cross sections of vertical boreholes

convergence drifts to a rather static end of deformation without closure of the borehole. The axial displacement of the model is restrained due to the assumed plane strain condition. The radial deformation of the outer boundary is also constrained with this model (a). An initial deformation of the borehole wall is enabled by redistribution of the stress field. The subsequent convergence of the borehole is prevented due to the constant volume of the model (which is equivalent to the modeled area due to plane strain). The calculation results reveal thus that models of a horizontal cross section with plane strain conditions and with the assumption of a radially constrained outer boundary are not suitable for convergence problems.

The plane strain model with constant far-field pressure (b) and the two models with an axisymmetric disk (c) and (d) overestimate the convergence. In contrast to model (a) these models allow for deformation of the boundary of the borehole wall even with constant area (b) or constant volume (c and d) of the model. However, as outlined above, the supporting effect of the borehole bottom on convergence cannot be taken into account with these models. As the borehole bottom influences the stress field at the considered cross section (one diameter above the borehole bottom) with the axisymmetric model this leads to an overestimation of convergence with horizontal cross sections. However, this overestimation is on the safe side if numerical calculations are carried out with respect to maximum expected convergence within a defined period of time.

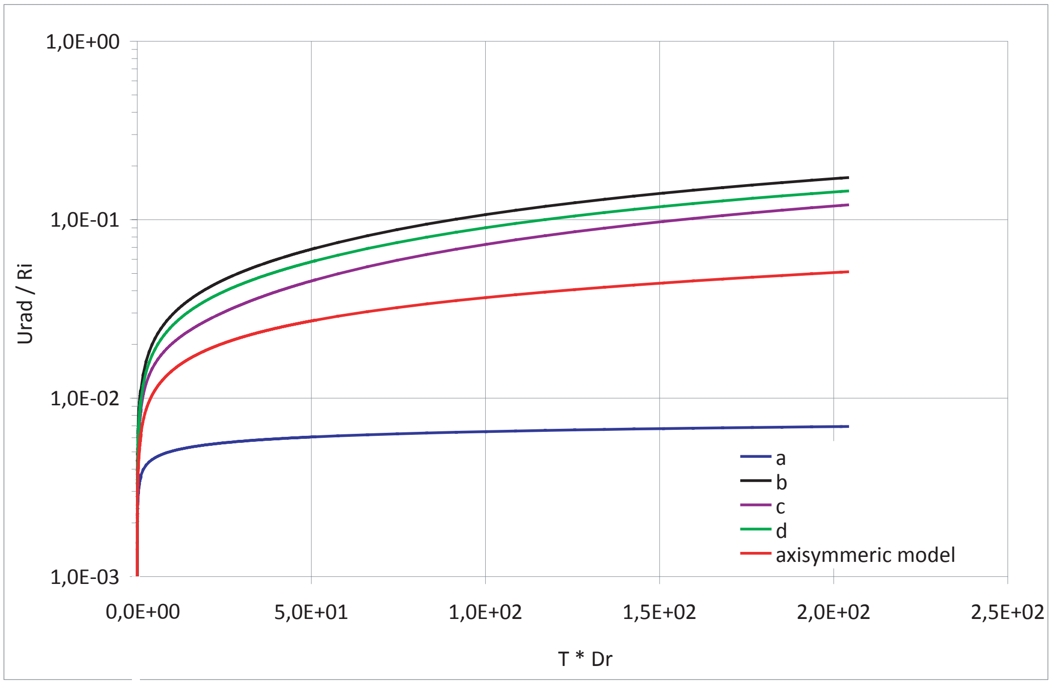

Figure 5.30: Evolution of the calculated convergences with different numerical models (labels explained in the text)

5.4.4 Supporting effect of drilling fluids, casings and linings

The convergence of circular excavations like boreholes, shafts and tunnels can be reduced with a support at the excavation surface. The support can be applied with e.g. drilling fluids, casings and linings. Numerical simulations with plane strain models have been carried out in order to investigate the influence of supports on the convergence of circular excavations. The simulations have been carried out with assumed material constants of a viscoplastic formation according to Tab. 5.2 and a support according to Tab. 5.3. A cross-section perpendicular to the longitudinal axis of the excavation has been considered.

A constant pressure $p_o = 6.5$ MPa at the outer boundary of the model has been assumed according to Fig. 5.29b. Thus, the model holds for a horizontal cross-section of a vertical borehole. The overestimation of convergence is the highest with this model, thus on the safe side (Fig. 5.30). Nevertheless, the model could serve also for an inclined borehole or a tunnel within an isotropic horizontal stress field at great depths where the gradient of vertical stress may be neglected. A supporting fluid is modeled with a constant pressure, casings and linings can be modeled with a ring of beam elements at the excavation surface. Symmetry allows for modeling of only one quarter of the cross section (Fig. 5.31). Note that this model allows also for consideration of a stress field whose ratio of principal in-plane stress components deviates from one.

Table 5.2: Assumed material constants of a viscoplastic formation (plane strain simulations)

E	ν	$\left\|\underline{D_r}^*\right\|$	$\left\|\underline{T_r}^*\right\|$	n
[MPa]	[-]	[1/min]	[kPa]	[-]
10000	0.49	5 E-9	6000	5.0

Table 5.3: Assumed elastic constants of a support (plane strain simulations)

$E_{support}$	$\nu_{support}$
[MPa]	[-]
25000	0.25

The results of the numerical calculations show that the convergence can be reduced significantly with an internal fluid pressure p_i. Fig. 5.32 reveals that an internal pressure p_i that amounts 25% of the far-field pressure p_o at the outer boundary of the model reduces the convergence to less than one half of the convergence of an unsupported ecxavation. An increase of support pressure leads to a disproportionaly high reduction of convergence. Fig. 5.33 shows characteristic lines for the radial displacement of the excavation wall depending on the ratio p_i/p_0. The characteristic line at $t_0 = 0$ holds for the elastic behavior of rock and is well known from tunneling. The calculation results show that characteristic lines for viscoplastic rock vary with time.

Casings and linings enable a reduction or even a stopping of convergence. Fig. 5.34 compares the evolution of convergence of a circular excavation which is supported with a casing and an unsupported excavation. The calculation results reveal that the convergence

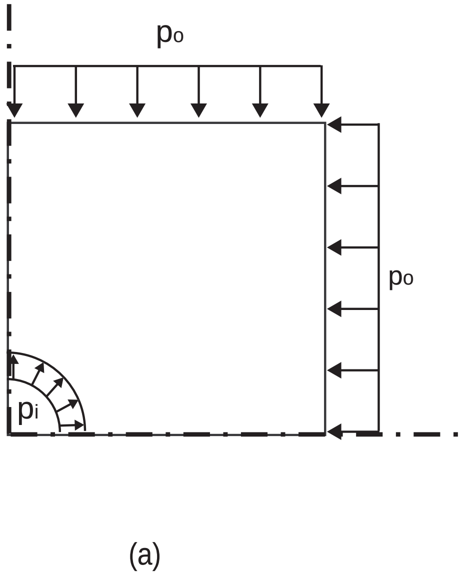

Figure 5.31: Models to investigate the influence of a supporting pressure (a) and of an supporting structure (b), (1) support

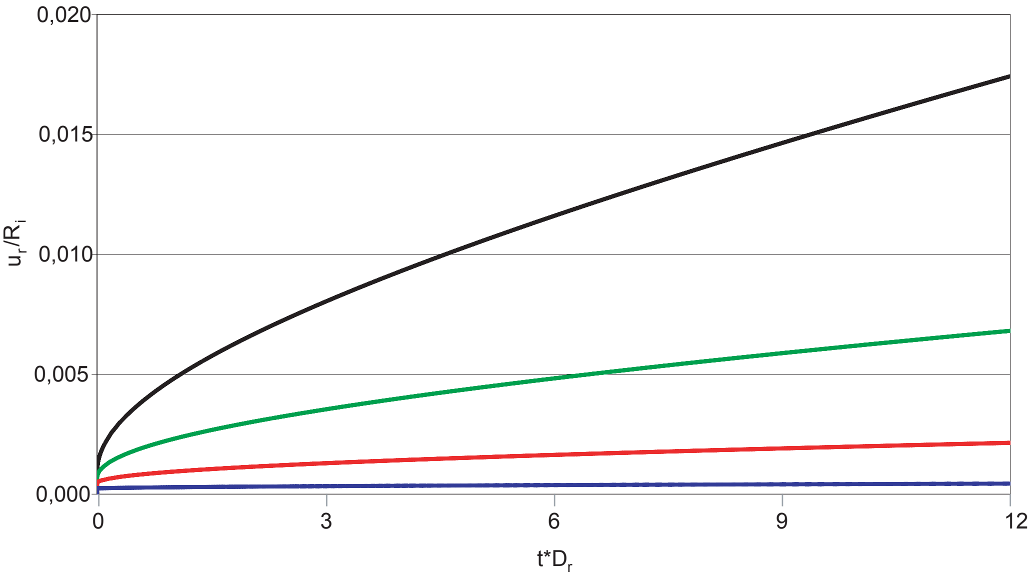

Figure 5.32: Results of numerical calculations with different ratios of fluid pressures, $p_i/p_o = 0$ (black), $p_i/p_o = 0.25$ (green), $p_i/p_o = 0.50$ (red), $p_i/p_o = 0.75$ (blue)

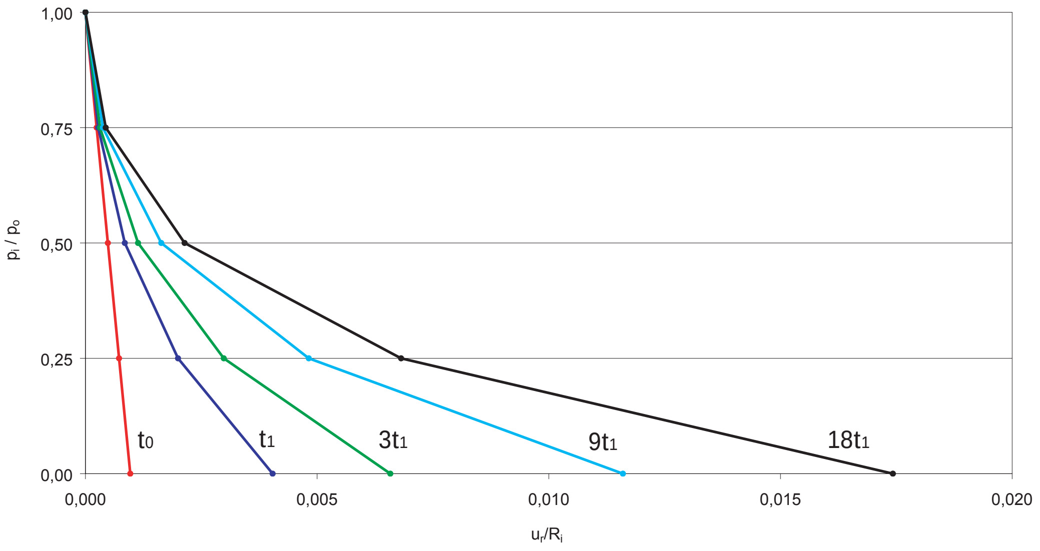

Figure 5.33: Characteristic lines for the radial displacement of the excavation wall

can be significantly reduced with a perfect linear-elastic support (curve a). It appears that the convergence tends asymptotically to a constant value. However, this at rest state can only be attained with an adequate material strength of the support.

Curve (b) shows the calculation results of a model with linear-elastic and plastic material properties with limited ductility. The convergence evolves in three stages. The first stage (i) is characterized by the elastic behavior of the support. The second stage (ii) starts when the yield stress of the support is reached. The convergence increases faster than with a perfectly elastic support. However, ductility of the casing material enhances the resistance of the support, thus for a supporting pressure at the excavation surface. The third stage (iii) starts when the end of the ductile regime of the casing material is reached. Softening of the material leads to a sudden increase of the convergence rate. The supporting pressure decreases suddenly due to softening of the casing, and convergence evolves like with an unsupported excavation.

The results of the numerical calculations with support of the excavation reveal the importance of ductility of the support. Ductile casings enable an early detection of borehole closure before a sudden collapse. The yield strength of the casing provides a support pressure which has a retarding effect on convergence. This enables a continued use of the borehole within a limited time period and for planning a rehabilitation. Ductile tunnel linings enable a sufficient time to detect an increase of convergence, to evacuate staff and to reinforce the support in order to prevent a collapse.

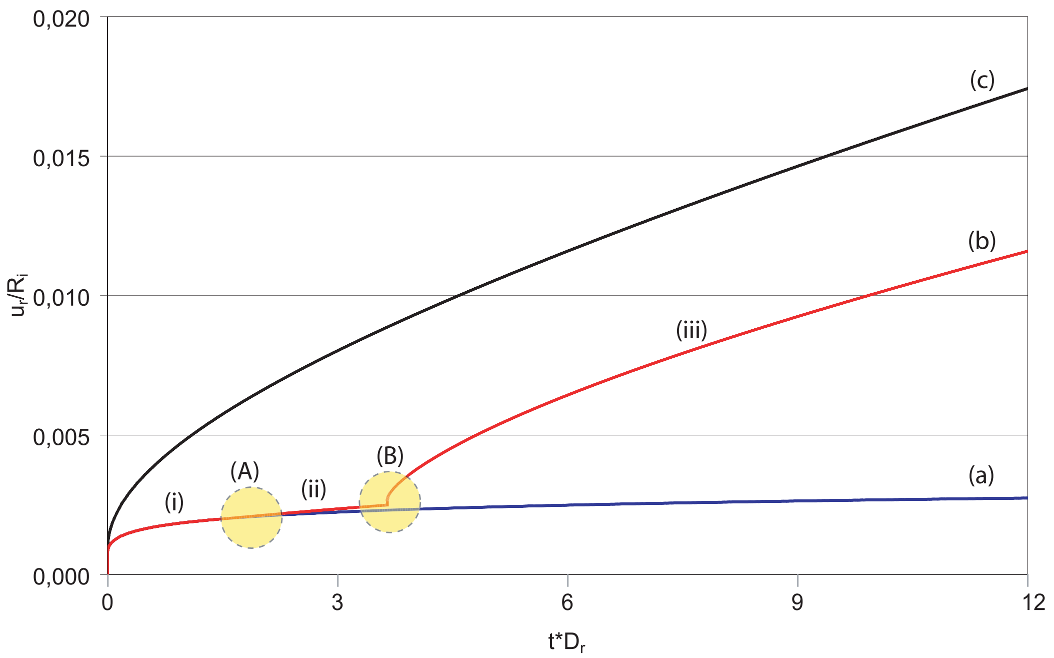

Figure 5.34: Evolution of convergence of an circular excavation with linear elastic support (a), elastoplastic support with limited ductility (b) and without support (c), plastic yielding of support (A), end of the ductile regime of the supporting material (B)

5.5 Conclusions

The convergence of a vertical borehole by creep increases significantly in its major part if the deviatoric part of the far-field stress (often called far-field pressure) exceeds a critical value. This is confirmed by model tests with a hydrogel. The influence of formation strength and viscosity can thus be estimated. Suitable far-field conditions can be formulated to estimate the convergence with a representative disc with suitable stresses. The same approach works also with a support of a borehole. The results of simulations with discs or plane strain models show, that such models are not capable to substitute estimations of cavings with axisymmetric models. Caving which exceeds shortening of approx. 5 - 10% of a borehole diameter are regarded as problematic in drilling praxis. The use of reconstituted samples may therefore serve as a crude approximation for the material in the vicinity of a borehole.

Chapter 6

Cap rock integrity

6.1 Motivation and overview

The development of strategies for sustainable and safe technologies for an efficient reduction of emissions of greenhouse gas to the atmosphere is a major challenge. Geological CO_2 storage in saline aquifers can be considered as one of the most promising technologies for such a reduction for an intermediate time period until other technologies will be available on a commercial scale. Anticlinal structures with a well-sealed cap rock above a storage reservoir provide a trapping mechanism for CO_2 in the underground. Leakage of a CO_2 storage facility has to be avoided for human health and protection of the environment. Sufficiently high deformation rates due to changes of pore pressure in a reservoir can lead to a reactivation and opening of existing crack systems and to new shear bands in clay smears of normal faults in a cap rock which imply potential leakage paths. Thus, the evaluation of expected deformation rates during and after an injection is a key issue for a safe underground storage of CO_2.

This chapter deals with the estimation and evaluation of deformation rates in a cap rock which may be expected during and after a CO_2 injection. The geotechnical framework of underground CO_2 storage is explained. Based on exemplary data, evolutions of deformation rates due to CO_2 injection are simulated with an axisymmetric model. It is shown with typical in-situ data that deformation rates in a seal can be kept low enough with reasonable changes of the reservoir pressures due to elastic stressing of the formations above and below.

6.2 Geotechnical framework of CO_2 storage

Different types of leakage of a storage site can be distinguished: sudden leakage or gradual leakage [27]. A sudden leakage can occur due to a failure of an injection well or along an abandoned well, and is likely to release a large volume of CO_2 within a short time. Thus, this type of leakage may be detected and stopped with techniques that are available from hydrocarbon industry to prevent blow-outs [27]. A gradual leakage can occur through undetected faults and fractures in a sealing cap rock formation or through undetected wells [27], but these risks can be reduced with intensive site investigations. They are not considered in the sequel.

A gradual leakage may also occur through reactivated and opened preexisting crack systems (Figure 6.1). The pore pressure in the target formation increases over a certain area within a certain time, which depend on the rate of injection, and causes a bulge of the cap rock with a smooth rim [25]. The seal overlying the target formation is extended along the lower part of the rim, and compressed along its upper part (a). Sufficiently high deformation rates can lead to a reactivation and reopening of existing crack systems along the lower part of the seal, but not yet to a breakthrough as the upper part is compressed. The increase of pore pressure during an injection causes also further deformations of *clay smears*, which can lead to new dilated narrow shear bands (b). A weak cementation of the sealing rock may be neglected in order to be on the safe side [24].

The pore water in the cap rock is slightly expanded by the minute opening of a latent crack system and the dilation of shear bands. This happens without filtration of pore water in the otherwise extremely impervious seal (e.g. a mudstone formation) [24]. A subsequent hydraulic breakthrough can only occur if the hydraulic gradient reaches a critical amount which is sufficient for erosion of the fine grained seal into an overlying coarser grained formation of the cap rock. This worst case scenario may lead to erosion channels in the seal which enable the passage of liquid, supercritical or gaseous CO_2. A hydraulic breakthrough and subsequent progressive erosion can evolve to a blow-out of a mixture of CO_2, water and eroded solid particles similar to an eruption of a mud volcano. This leakage scenario must be safely avoided with a very high probability. A sealing cap rock is indispensable for a successful injection of CO_2 into a deep saline aquifer, and the integrity of such a cap rock has to be preserved during the whole time of storage.

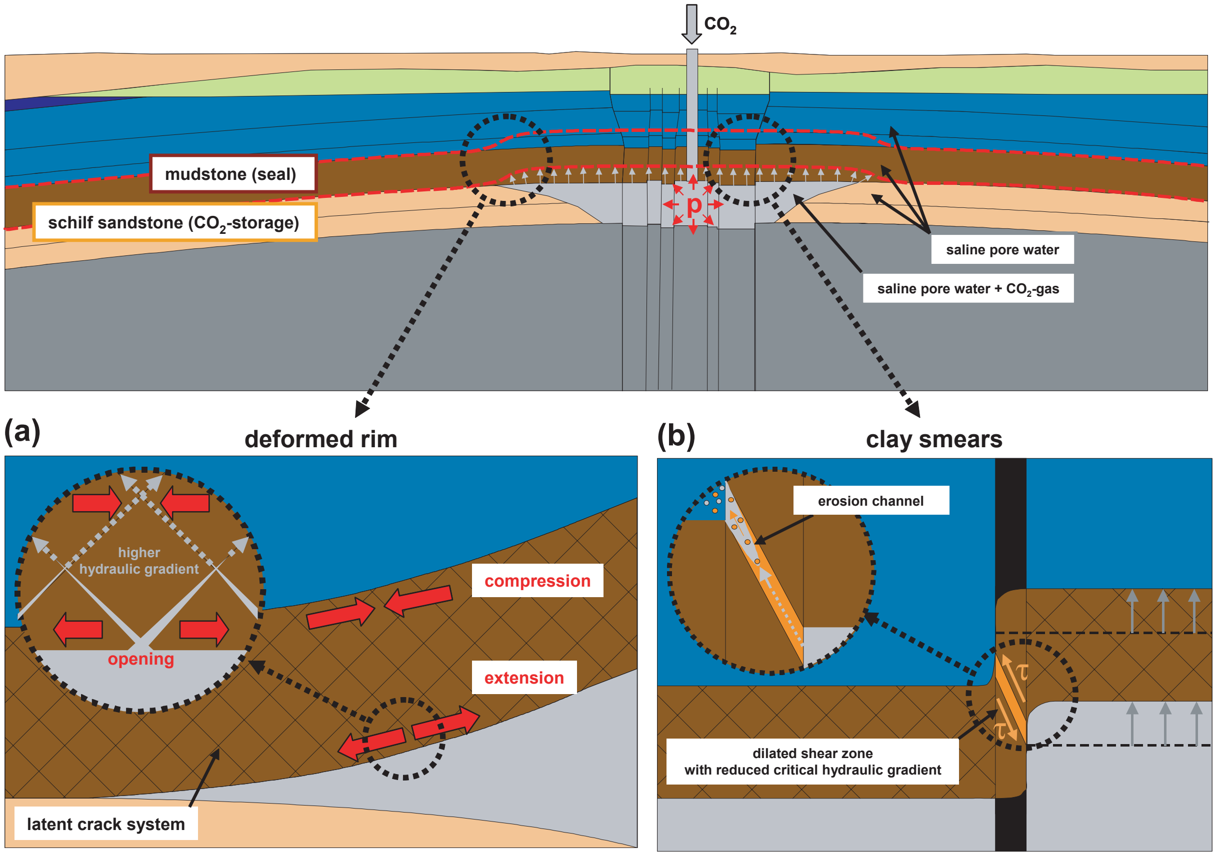

Figure 6.1: Leakage scenarios of a seal during CO_2 injection with opening of a latent crack system (a) and further shearing of clay smears (b), from [24]

6.3 Numerical calculations

6.3.1 Introduction

Sufficiently high deformation rates can lead to a reactivation and reopening of existing crack systems in a sealing formation and to new shear bands in clay smears. Thus, prognoses of deformation rates in a cap rock are indispensable for a safe CO_2 injection. This requires a suitable geotechnical model of the subsoil conditions and simulations of injection scenarios with realistic boundary conditions. Because of the complexity of such a model, numerical calculations by means of the finite-element-method (FEM) are principally suitable to estimate the deformation rates which result from a CO_2 injection. The first European onshore storage project for CO_2 injection into a deep saline aquifer at the town of Ketzin near Berlin, Germany, is a research and development project and is thought as an in-situ laboratory for CO_2 storage. The project site is an European pilot site for CO_2 storage in a populated area, and has been chosen to test geotechnical mechanisms which are relevant for a safe injection and storage of CO_2.

6.3.2 Geological setup

Ketzin is located in the northeast German Basin at the southern flank of an anticline. The anticline was formed by halokinesis (diapirism) above a salt pillow from the Zechstein formation at an approximate depth of 1500-2000 m below sea level [29]. Geological formations of the Triassic (Buntsandstein, Muschelkalk and Keuper) and of the Lower Jurassic build the immediate overburden above a salt pillow [29]. These formations were tectonically deformed to an anticline due to halokinetical uplift. Tertiary sediments of the Oligicene (Rupelton) are resting above the Jurassic sediments. Glacial erosional troughs in the Tertiary sediments are filled with Quaternary sediments. The geological structure and strata at Ketzin can be regarded as a typical trapping mechanism for CO_2 storage [29].

The target formation of the CO_2 injection is the Stuttgart formation of the Triassic age, the top of which is located at an approximate depth of 650 m b.s.l.. This lithologically heterogeneous formation consists of sandy rock facies with good reservoir properties, which alternate with muddy rock facies with rather poor reservoir quality [29]. CO_2 is injected into the porous and permeable sandstones of the Stuttgart formation at an approximate depth of about 700 m below surface [29]. The overburden of the target formation contains several aquifers and aquitards.

A 3D seismic survey over the Ketzin anticline, which was carried out before starting with the CO_2 injection, provided information on existing faults. The results show a fault system across the top of the anticline that may be termed the Central Graben Fault Zone (CGFZ) [30]. The CGFZ consists of approximately east-west-trending normal faults bounding a 600-800 m wide graben [30]. The discrete faults are well developed in the Jurassic section, where the main graben-bounding faults have throws of up to 30 m [30]. The fault system seems to die out in the Tertiary Rupelian clay [30].

6.3.3 Model description

A simplified axisymmetric model (Figure 6.3) has been chosen for numerical calculations of deformation rates. For reasons of simplification the injection is located at the symmetry axis of the model. The geological strata has been reduced to four characteristic layers: a layer below the reservoir (L1), a reservoir layer (L2) with a respective thickness of 100 m, an overlying sealing cap rock layer (L3) with a respective thickness of 100 m and a layer

(L4) which comprises all cap rock layers which overly the seal to the ground surface. The surfaces of the layers in the model are horizontal, assuming that a slight initial bulge due to a anticline structure can be neglected for the following considerations.
Up to 100 t/d of food grade CO_2 were injected at about 700 m b.s.l into a saline sandstone aquifer at the Ketzin storage site [29], [28]. Simulations of the evolution of the spatial distribution of injected CO_2 with tools for oil and gas reservoir management indicate that the maximum lateral extension of CO_2 in the reservoir will probably not reach the major fault system of the CGFZ at Ketzin [30]. However, the possible presence of undetected or minor clay smears at Ketzin, narrower fault systems at other storage sites and injection rates and quantities that may differ from those which have been simulated may lead to CO_2 distributions in a reservoir that reach a fault. Therefore, a model with a single representative fault with a throw up of half of the thickness of the sealing layer has been chosen for the model. Fig. 6.2 shows a simulated faulting with an arising clay smear from [13]. The band thickness of a clay smear does not evolve thinner than 15 - 20% of the source layer thickness and suffices to work as a hydrocarbon seal. Therefore, a thickness of 20% of the layer L3 has been chosen for the clay smear in the model (darker colored area in Figure 6.3).
Appropriate displacement boundary conditions have been chosen according to the assumption that radial or vertical displacements, which are induced by changes of the reservoir pressure, are negligible at the the outer and lower model boundaries (Figure 6.3).

The initial state of stress in the Ketzin anticline is rather unknown. Stresses in the upper earth crust have been estimated within the scope of the so-called World Stress Map, but at present they are not available for the region and depth of the Ketzin anticline [31]. Due to diapirism, the in-situ stress state in an anticline is expected to be rather complex and highly variable in space. Geostatic and isotropic conditions have been chosen to define an initial stress state in the model. Absence of initial deviatoric stresses is assumed in spite of these conditions, it prevents arbitrary viscous deformations in the model prior to an injection. Thus, it allows for a calculation of deformation rates which result only from changes of the reservoir pressure. The asymptotic stress fields outlined in Chap. 4 may serve as a support for this simplifying assumption.

As known from investigation boreholes, the geologic formations above the diapir at the Ketzin storage site comprise a large number of sedimentary rock layers with different properties. Elastic and viscoplastic properties of rock can be described and determined as outlined in Chap. 2 and 3. Determination of properties with natural rock samples from in-situ requires cost-intensive core drilling. Core recovery and the quality of rock samples depend strongly on drilling techniques and drilling fluids. Beside an inevitable disturbance of the in-situ state (e.g. due to stress relaxation), unsuitable core drilling

Figure 6.2: Simulated faulting with an arising clay smear, composite with dislocation, from [13]

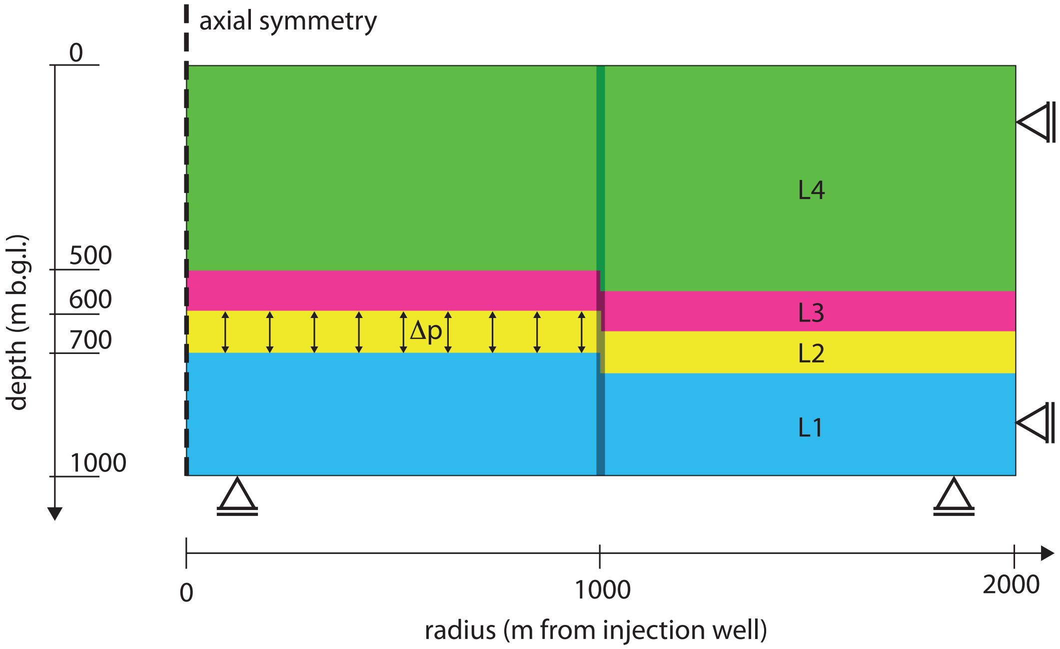

Figure 6.3: Simplified model of geological storage of CO_2

techniques or fluids may additionally cause modifications of rock properties (e.g. fracturing or soaking). From rock mechanics it is known that material properties of sedimentary rocks may be highly variable in space due to locally changing sedimentation conditions. Investigation boreholes are always pin-pricks into the subsurface, and only a sufficiently large quantity of core samples would allow a statistically representative determination of material properties. Thus, it is hardly practicable to determine a detailed spatial distribution of in-situ material properties within an entire geological structure (e.g. an anticline). Instead, estimations of deformations due to CO_2 injection by means of numerical calculations should be carried out with reasonable ranges of material parameters.
The layers L1, L2 and L4 in the model are assumed to be linearly elastic. The layer L3 (seal) has elastic and viscoplastic material properties. Viscoplastic material parameters may be assumed according to the results of laboratory tests as shown in Tables 3.7 and 3.14. Shearing in faults means remolding, thus material parameters of a clay smear can be determined with reconstituted samples. Numerical calculations in this thesis have been carried out with Young's moduli according to Table 6.1. The given ranges of parameters are based on experimental findings and include values that have been published in the literature for materials that may be comparable with those at Ketzin. Heterogeneous compositions of rocks within each of the four layers of the model lead to wide ranges of parameters. A refined resolution of the stratigraphy in the model would only be useful with a more detailed knowledge about the material properties of each resolved layer. However, the given values should be regarded as rough estimations which can serve as reasonable examples for heterogeneous material compositions of reservoirs and cap rocks.

Table 6.1: Reasonable ranges of elastic parameters

model layer	charact. function	typical rock types	range of E [GPa]	references
L4	overlying cap rock	quaternary soils (clays to sands), tertiary clays and marls, silt- and mudstones, sandstones, carbonates	0.1 - 10	[33], [34], [36]
L3	seal	mudstones and clayey siltstones with anhydrite	3 - 13	Chapter 2
L2	reservoir	porous sandstones	5 - 15	[28], [32],[35]
L1	underlying formations	marlstones, marly dolomite, anhydrite, gypsum, limestones, dolomite, sandstones	30 - 70	[32],[35]

A successful injection of CO_2 into a saline aquifer requires injection pressures which exceed the capillary entry pressure of the target formation. Higher injection pressures enable the replacement of the brine with CO_2 in the pore space of the rock. At constant permeability of the reservoir, higher injection rates require an increase of the injection pressure. A sufficiently high injection pressure can lead to so-called hydraulic fracturing of the reservoir if resulting stresses exceed the tensile strength (i.e. cohesion due to cementation of grains) of the rock. Although this may increase the permeability of a reservoir, new fractures from a reservoir may also propagate into an overlying seal and could lead to leakage. Thus, hydraulic fracturing has to be safely avoided.

Changes of the excess pore pressure Δp have been assumed in the mechanical model (Figure 6.3) with boundary conditions in the reservoir layer which vary during the run of a calculation. Evolutions of reservoir pressures have been assumed for the mechanical model, based on calculations which have been carried out at the University of Stuttgart, Institut für Wasserbau.

Figure 6.4 shows a typical evolution of reservoir pressures as a result of a simulated injection of 2 kg/s of CO_2 within a time period of two years. The result shows that the calculated pore pressure decreases from its maximum value at the injection well with increasing radial distance. The result indicates that a constant injection rate leads to a constant maximum pressure at the well, and to a continued increase of the pore pressure to a maximum at points off the well.

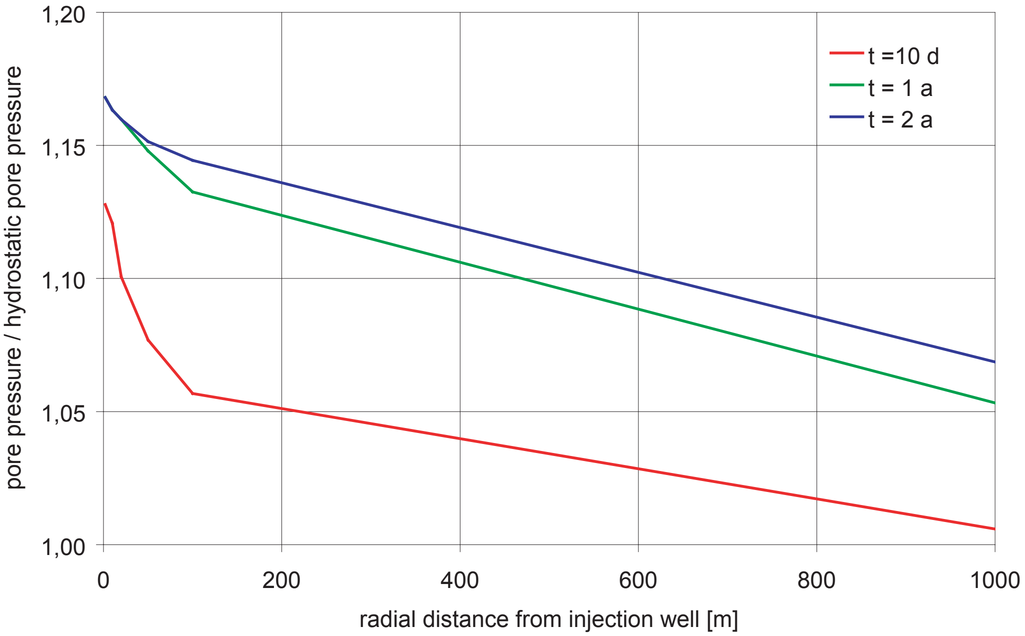

Figure 6.4: Typical evolution of reservoir pressure, result of a simulated injection [26]

The evolution of reservoir pressures as shown in Figure 6.4 has been linearized for further use with boundary conditions in the mechanical model for the calculation of deformation rates. Arbitrary spatial evolutions (pore pressure fields) from results of multiphase flow calculations could be applied to the mechanical model by means of user subroutines. However, the chosen linearized pressure distribution suffices to show typical evolutions of deformations due to a CO_2 injection. Figure 6.5 shows the linearized evolution of excess pore pressure as fractions of the maximum excess pressure at the well Δp_{max} which has been exemplarily chosen for the calculations in the sequel. The pressure increase Δp is applied during subsequent calculation steps (S1 - S3). A subsequent calculation step (S4) considers an additional scenario, where a continued injection for a time period of three years may lead to an increase to a maximum pressure Δp_{max} which is constant from the well to the fault. The pressure increase within each step is linear with respect to time. Table 6.2 gives an overview about the calculation steps with times and pressures at the end of each step.

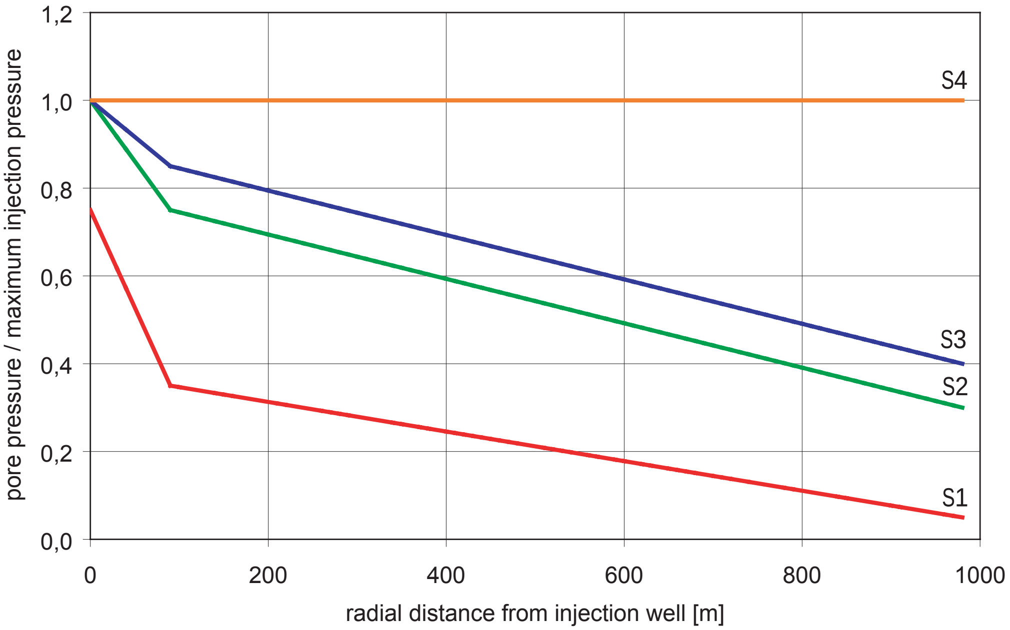

Figure 6.5: Linearized evolution of pore pressure as fractions of the maximum pressure at the well after 10 days (S1), 1 year (S2) and 2 years (S3). (S4) indicates a further increase to a constant pressure with an additional calculation step.

The chosen model and its dimensions are shown in Figure 6.3. The model may be regarded as a simplification for geological storage of CO_2. It is suitable to show some geomechanical principles which are considered to be relevant for a safe underground storage of CO_2 at comparable sites. A detailed model of the geology and the temporal and spatial evolution

Table 6.2: Calculation steps for numerical calculations of deformation rates due to a CO_2 injection

calc. step	time at end of step	Δp
S1	10 days	acc. to S1, Fig. 6.5
S2	1 year	acc. to S2, Fig. 6.5
S3	2 years	acc. to S3, Fig. 6.5
S4	3 years	acc. to S4, Fig. 6.5

of the reservoir pressure at Ketzin is beyond the scope of this work. Depending on the local geology of a storage site, plane strain or three dimensional modeling may be alternatives. A more detailed resolution of the geologic structures (e.g. layers and faults) will be adequate if the geometry, material properties and initial conditions of additional details have been sufficiently investigated and determined. Models of a CO_2 storage site can be nearly arbitrarily refined with the chosen software and with sufficient hardware capacities. A suitable model is only detailed enough to suffice for a realistic safety assessment.

6.3.4 Results and discussion

Numerical calculations have been carried out as described above with maximum excess pressures $\Delta p_{max} = 1.5$ MPa, 3.0 MPa and 4.5 MPa at the well. Viscoplastic constants according to Table 3.7 have been chosen for the seal. A set of characteristic mean values for the Young's moduli (set 1) according to Table 6.3 have been chosen from the ranges of Table 6.1. For the material in the fault, the moduli have been reduced to 10% since strong shearing of the fault material may have reduced its stiffness. This reduction may serve as a first crude assumption.

Table 6.3: Characteristic mean values for the Young's moduli (set 1)

model layer	E_{calc} [GPa]	ν_{calc} [-]
L4	1	0.30
L3	10	0.45
L2	10	0.30
L1	50	0.30

Figure 6.6 shows the norm of induced deviatoric stresses by maximum excess pressure at

the well $\|\underline{T}^*\|/\Delta p_{max}$ in the viscoplastic layer L3 (seal) at the end of each calculation step S1 to S4. The results are equal for all calculated pressures Δp_{max} since the numerically calculated viscoplastic deformations in the seal are practically zero.
The results show that deviatoric stresses in the seal increase with a continued pressure increase. Maximum deviatoric stresses are reached with all calculations at the end of step S4, where a constant maximum excess pressure Δp_{max} extends from the well to the fault in the model. The calculated induced deviatoric stresses are small, even with $\Delta p_{max} = 4.5$ MPa. Table 6.4 shows the maximum induced deviatoric stress $\|\underline{T}^*_{max}\|$ in the seal (L3) at the end of the steps S1 to S4 with $\Delta p_{max} = 4.5$ MPa. With equation (3.38) the norms of the deviatoric deformation rates $\|\underline{D}^*_{max}\|$ have been calculated from the maximum deviatoric stresses. Table 6.4 shows the calculated viscoplastic deformation rates. Due to their magnitude, they appear as zero values in the numerical calculations that have been carried out.

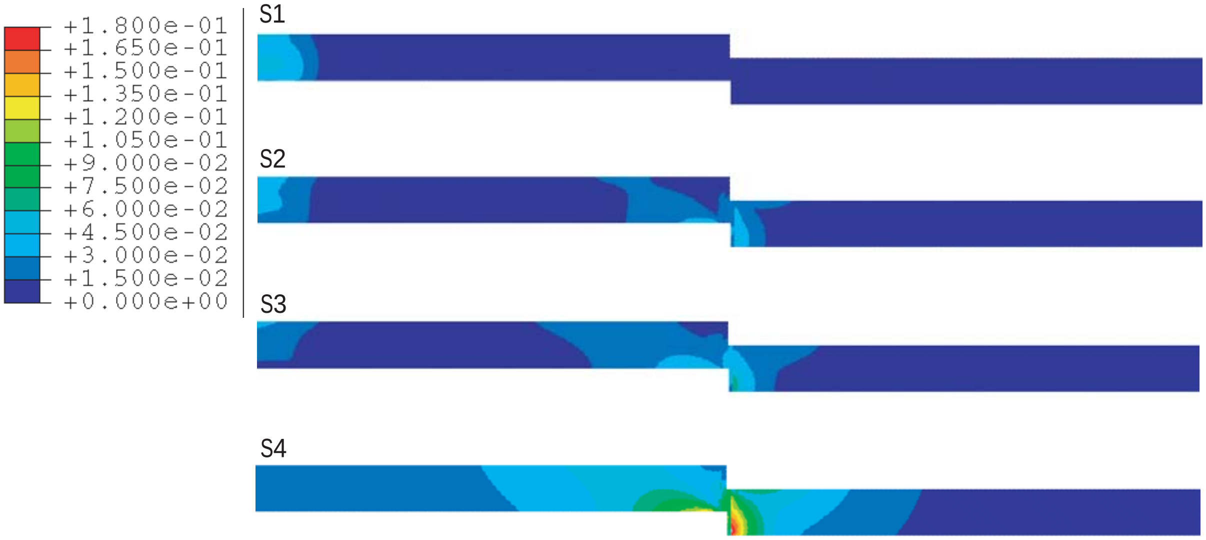

Figure 6.6: Induced deviatoric stresses $\|\underline{T}^*\|/\Delta p_{max}$ in layer L3 (seal), results of numerical calculations with set 1 at the end of the calculation steps S1 to S4.

A pressure increase Δp in the reservoir layer (L2) causes deformations in the layers L2, L3 and L4 of the model. L1 gets also deformed, but less. Compared to the Young's moduli of set 1 (Table 6.3), smaller stiffnesses of the layers L2 and L4 would lead to higher deformations due to Δp. A higher stiffness of the seal (L3) would lead to higher deviatoric stresses in this layer, thus to higher deformation rates. The results of the numerical calculations at the end of step S4 (Figure 6.6) show that maximum induced deviatoric stresses in the seal occur in the vicinity of the clay smear. They are somewhat smaller in the clay smear due to a reduced stiffness that has been assumed for this material. Higher deformation rates in the clay smear of the fault, which could be unfavorable for

Table 6.4: Maximum deviatoric stress $\|\underline{T}^*_{max}\|$ in the seal (L3) at the end of the steps S1 to S4 with $\Delta p_{max} = 4.5$ MPa

calc. step	$\|\underline{T}^*_{max}\|$ [MPa]	$\|\underline{D}^*_{max}\|$ [1/min]
S1	2.6E-01	1E-78
S2	2.3E-01	2E-81
S3	3.1E-01	1E-74
S4	8.2E-01	3E-53

the integrity of the seal, may be expected with a higher stiffness of the clay smear. Thus, additional calculations have been carried out without reduced stiffness of clay smear. Table 6.5 shows a set of elastic parameters (set 2) that has been chosen from the ranges given in Table 6.1 for numerical calculations with higher deformation rates in the clay smear.

Table 6.5: Young's moduli for calculations with higher deformation rates in the clay smear (set 2)

model layer	E_{calc} [GPa]	ν_{calc} [-]
L4	0.1	0.30
L3	13	0.45
L2	5	0.30
L1	70	0.30

A numerical calculation with set 2 has been carried out with $\Delta p_{max} = 4.5$ MPa. Figure 6.7 shows the norm of induced deviatoric stresses divided by maximum excess pressure at the well $\|\underline{T}^*\|/\Delta p_{max}$ in the viscoplastic layer L3 (seal) at the end of each calculation step S1 to S4. The results show that maximum deviatoric stresses are induced again in the clay smear with set 2. At the end of step S4 a maximum value $\|\underline{T}^*\| = 3.2$ MPa is reached in the clay smear next to the reservoir. The numerically calculated viscoplastic deformations in the seal are zero, as with the calculations with set 1. Thus, Figure 6.6 and Figure 6.7 are comparable. According to equation (3.38) the calculated maximum viscoplastic deformation rates are $\|\underline{D}^*_{max}\| = 2\text{E-}23$ 1/min.

Additional numerical calculations with set 2 have been carried with $\Delta p_{max} = 6.0$ MPa and with $\Delta p_{max} = 7.5$ MPa. Figure 6.8 shows the evolution of the maximum induced deviatoric stresses in the clay smear. Deviatoric stresses increase approximately linear within each

Figure 6.7: Induced deviatoric stresses $\|\underline{T}^*\|/\Delta p_{max}$ in layer L3 (seal), results of numerical calculations with set 2 at the end of the calculation steps S1 to S4.

calculation step S1 to S4 with pressure increases $\Delta p_{max} = 4.5$ MPa and $\Delta p_{max} = 6.0$ MPa, and also with $\Delta p_{max} = 7.5$ MPa within the calculation step S1 to S3. It appears that a further pressure increase in step S4 with $\Delta p_{max} = 7.5$ MPa leads to a disproportionally low increase of the maximum deviatoric stresses in the clay smear for deviatoric stresses exceeding $\|\underline{T}^*\| \approx 4.5$ MPa. At the end of step S4 a maximum value $\|\underline{T}^*\| = 4.9$ MPa is reached in the clay smear. The calculated maximum viscoplastic deformation rate is $\|\underline{D}^*_{max}\| =$ 1E-14 1/min. The results indicate that the clay smear gets viscoplastically deformed with the calculated scenario. Nevertheless, the calculated deformation rates are many orders of magnitude lower than the deformation rates for which the tested material is no more ductile in the laboratory tests (Chapter 2). Therefore, the clay smear will probably remain in a ductile regime with deformation rates that are caused by a CO_2 injection with the assumed boundary conditions.

Numerical calculations with set 2 have been carried out with an additional calculation step S5. During step S5 the reservoir pressures Δp_{max} applied at the end of step S4 are kept constant for a time period of five years. Figure 6.9 shows the evolution of the maximum induced deviatoric stresses in the clay smear during the time period of step S5. It appears that deviatoric stresses in the clay smear remain approximately constant with constant pressures $\Delta p_{max} = 4.5$ MPa (a) and 6.0 MPa (b). Nevertheless, the result of a calculation with a constant pressure $\Delta p_{max} = 7.5$ MPa (c) indicates that deviatoric stresses are decreasing at constant reservoir pressure due to viscoplastic deformations in the clay smear. During step S5 the maximum deviatoric stresses (c) decrease to $\|\underline{T}^*\|$

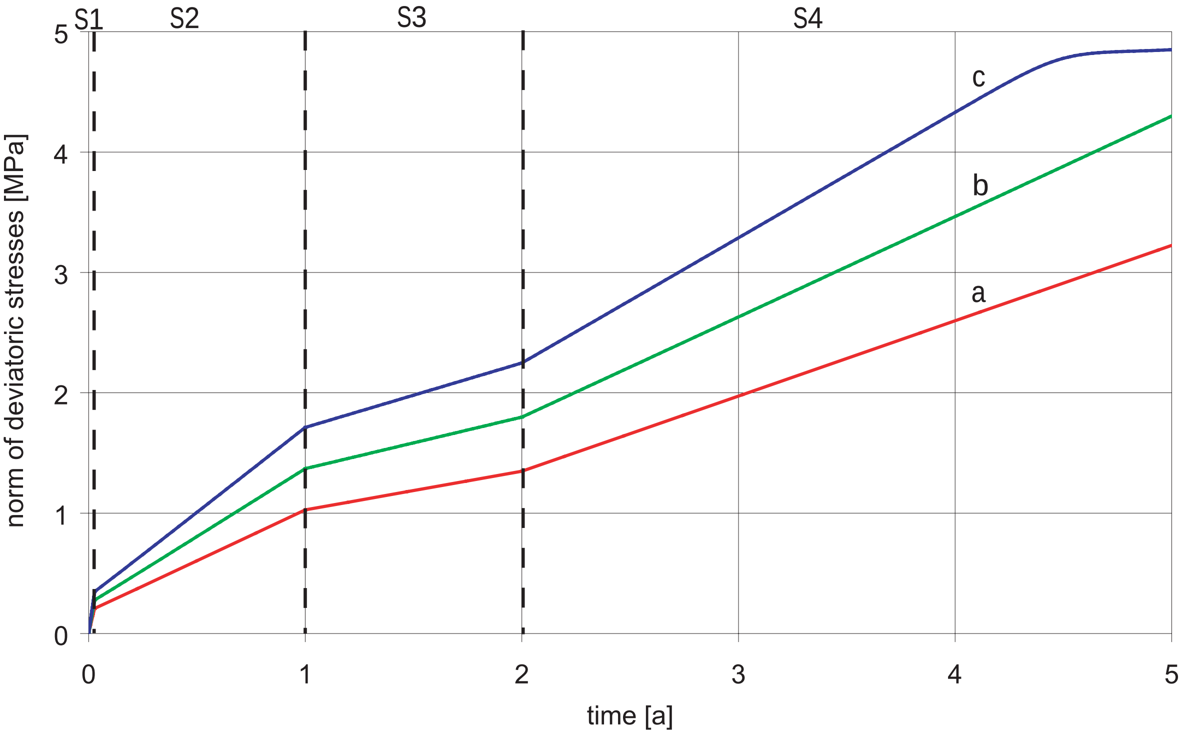

Figure 6.8: Evolution of maximum induced deviatoric stresses $\|\underline{T}^*\|$ in the clay smear, results of numerical calculations (calculation steps S1 to S4) with Δp_{max} = 4.5 MPa (a), Δp_{max} = 6.0 MPa (b) and Δp_{max} = 7.5 MPa (c)

= 4.5 MPa, which is approximately 92% of the value at the end of step S4. Thus, the viscoplastic deformation rates in the clay smear decrease to $\|\underline{D}^*_{max}\|$ = 2E-16 1/min at the end od step S5. The result with Δp_{max} = 7.5 MPa reveals that a reduction of deviatoric stresses of less than 10% can lead to a reduction of viscoplastic deformation rates of approximately two orders of magnitude.

The results of numerical calculations which have been described above reveal that a pressure increase due to CO_2 injection induces deformation rates in the clay smear for which the material can be expected to remain ductile. Thus, with the chosen model and boundary conditions, the integrity of a cap rock will likely not be affected with the applied pressures. However, material parameters and pressure rates have a considerable influence on the deformation rates in a clay smear. According to [13], 20% of the source layer thickness (L3) has been chosen for the thickness of the clay smear in the employed model. A thinner source layer with a corresponding thin clay smear could lead to higher shear stresses which come close to a limit stress state, and the amount of the shortening rate could reach a critial magnitude. Thus, in-situ conditions other than those assumed for our calculations could principally lead to critical deformation rates in a clay smear. Suitable

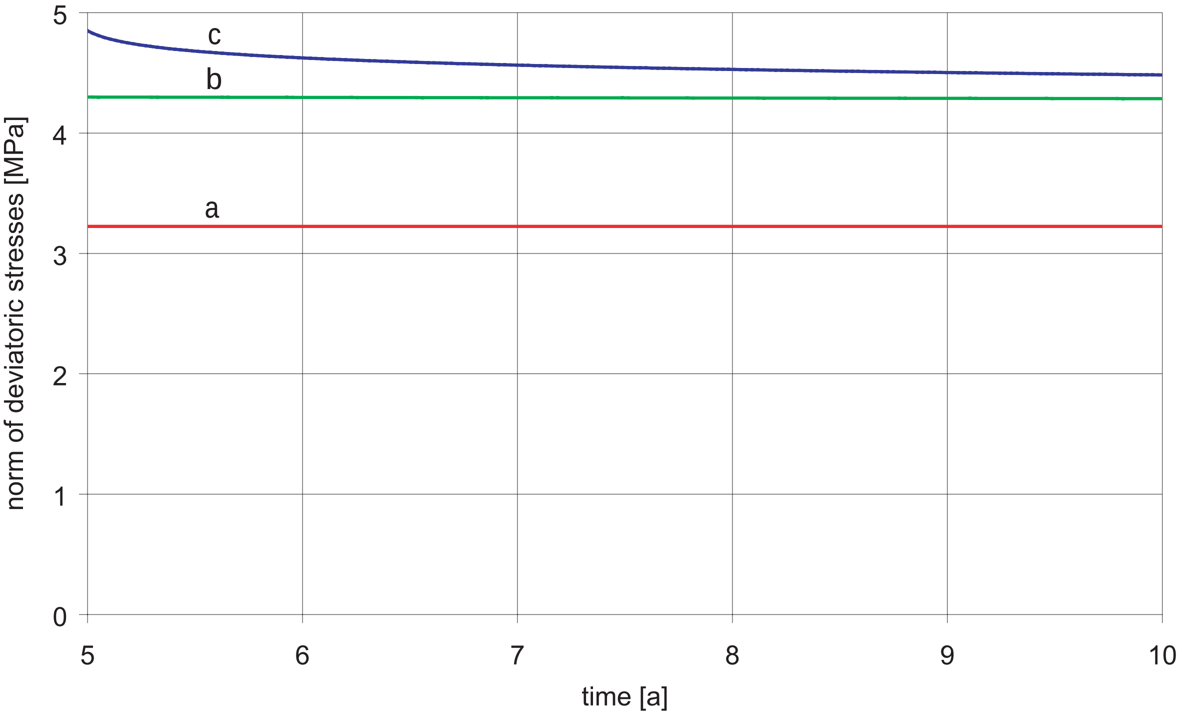

Figure 6.9: Evolution of maximum induced deviatoric stresses $\|\underline{T}^*\|$ in the clay smear, results of numerical calculations (calculation step S5) with constant reservoir pressure for a time period of five years, Δp_{max} = 4.5 MPa (a), Δp_{max} = 6.0 MPa (b) and Δp_{max} = 7.5 MPa (c)

simulations could be principally carried out after some adaptions of the employed model. Critical deformation rates have also to be avoided by a suitable monitoring. Monitoring of CO_2 concentrations near the ground surface appear to be insufficient for this purpose since a critical point would have been already reached when escaped gas is detected. Nevertheless, monitoring of CO_2 concentrations can serve as a warning system in case of a leakage. Deformation rates increase rapidly before a critical point would be reached in a clay smear, and are accompanied by a dramatical increase of seismicity. The proximity of a critical point may be detected with seismic monitoring. Thus, seismic monitoring is indispensable to control that a seal remains in a subcritical state. Suitable actions can thus be started early enough before a critical chain reaction is reached.

The results of the numerical calculations show that deformation rates in a clay smear can be reduced significantly by stopping a CO_2 injection (i.e. no further increase of the reservoir pressure). Deformations could be radically stopped by reducing the reservoir pressure. This would enable a self-healing of the clay smear due to thermally activated stress redistribution.

Deformations of axially symmetric cap rock formations above a diapir may be simulated with improved numerical models. A device as shown in Figure 6.10 could enable axially symmetric testing conditions which resemble those of a halokinetical uplift of a salt pillow (diapir) which induces ring structures in the overlying sand and clay layers. CO_2 could be injected through a vertical pipe into an initially water-saturated sand layer. The evolution of the spatial extent of the injected CO_2-plume could be monitored with suitable sensors. Deformations of the clay layer due to the injection pressure could be monitored and compared with calculation results from the numerical model. Thus validated numerical models could serve as an additional tool for exploration, design and managing of underground storage sites for carbon dioxide.

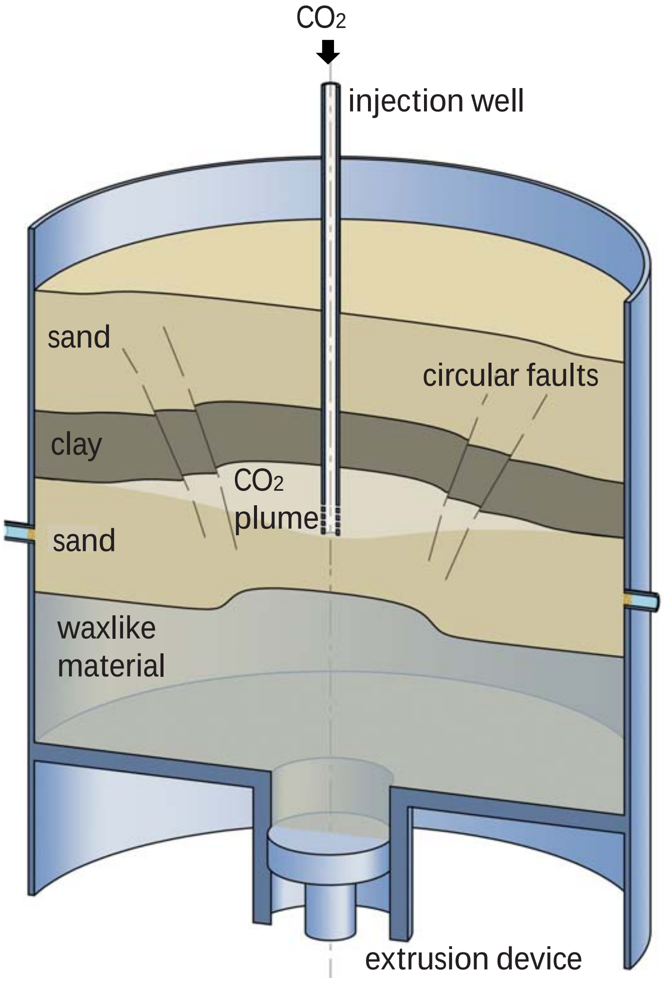

Figure 6.10: Model test with a salt pillow and injection, courtesy by K. Balthasar according to a sketch by the author

6.4 Conclusions

Cap rocks above salt pillows can be modeled with axial symmetry. A potential weak point is the clay smear in a fault, which is sheared anew by injection of fluid below the cap rock. Numerical calculations with realistic parameters and boundary conditions show that deformation rates in a clay smear can be kept very low with moderate pressure changes. Stopping an injection at a constant reservoir pressure can lead to markedly decreasing deformation rates of a clay smear. A moderate pressure reduction could reduce the deformation rates in a clay smear to zero, and thus enable a self-healing of the clay smear due to thermally activated stress redistribution. Thus, the system gets stabilized within a short time. Seismic monitoring could further serve to control that a seal remains in a subcritical state. Thus, suitable actions could be started early enough.

Chapter 7

Summary and outlook

7.1 Summary

The estimation and evaluation of deformation rates are key issues for mechanical considerations with viscoplastic formations.

Viscous effects (i.e. argotropy, creep and relaxation) were first studied with paraffin, which is a suitable material to demonstrate qualitatively the material behavior of a class of geomaterials which behave like wax. Paraffin exhibits a markedly non-linear viscosity, and the observed viscous effects resemble those of geomaterials like ice or rock salt with slow deformations. Soft soils exhibit a similar behavior if they are fully saturated as long as the pore fluid is incompressible and its filtration is excluded or may be neglected. Laboratory tests have been carried out with different geo-materials. Reconstituted samples of a natural clay and of a bentonite, with consolidation pressures of 20 and 150 MPa, respectively, exhibit likewise rate-dependence and an upper bound of stretching rate due to shear localization and fracture. These features have been likewise observed with natural mudstone samples, but for lack of uniformity before and during the experiments the identification of material properties is less precise.

The results of laboratory tests with geomaterials show that the viscoplastic behavior with sufficiently low deformation rates is similar to the behavior of paraffin in the subcritical state. Materials with such viscoplastic behavior in the subcritical regime are named keroids (Greek: wax-like). Assumed are isotropy of material properties, linear elasticity for rapid small deformations, nonlinear viscosity with negligible volumetric viscosity, dominant thermal activation and negligible seismic activation via pores and viscoplastic ductility for sufficiently low deformation rates. Ductility and viscoplasticity come together and hold for a certain range of deformation rates, pressures and temperatures. The material properties of selected samples that have been observed with laboratory tests accord essentially with these assumptions.

Micropores can occur in the ductile regime in a minute fraction, this increases spontaneously at the verge of ductility. Viscoplastic deformation is possible at low shortening rates up to a critical amount which characterizes the boundary of the ductile regime. At this shortening rate more micropores are produced than vanish in the same time. Thus, the micropores can evolve to flat pores and fractures. Shear localization and fractures have been observed with continued shortening with a critical (or even higher) shortening rate. The stress at the critical shortening rate characterizes a critical point of the material with a transition from viscoplastic to clastic behavior. Deformation rates much higher than critical result in axial splitting, which is accompanied by acoustic emission. Thus, an in-situ monitoring of seismic events is advisable for maintaining rock in a subcritical state. (The commonly used term failure is related with a subjectively expected requirement for a material. The term is not suitable for an objective description of material behavior.)

Almost any plasticity is a kind of non-linear viscosity. Viscous effects in solids can be physically explained with thermally activated changes of dislocations. The chosen constitutive equations are based on this kind of rate process theory and provide a description of argotropic behavior, creep and relaxation. They satisfy the requirements of objectivity. Isochoric deformations can be captured by deviatoric relations of stress rate with stress and deformation rate. Invariance with respect to units is achieved by two material constants. Invariance with respect to an arbitrarily chosen reference system is guaranteed by using an isotropic tensor function. Since only deformation rates (and not strain) matters for the material behavior there is no influence of an arbitrarily chosen initial state. Since no internal variables are employed, the fabric of the keroid is assumed to be determined only by the deviatoric stress. This approach is, at least for the time being, restricted to monotonous evolutions. The range of validity is limited by upper bounds of stretching rates due to shear localization and cracking. Numerical simulations of the carried out laboratory tests with the employed constitutive equations provide an acceptable agreement.

One-dimensional boundary value problems with viscoplastic formations have been considered with respect to the evolution of velocity and stress. A one-dimensional analysis of the creep of a slope shows that an arbitrary allowable initial stress and velocity field leads asymptotically to a stationary field of velocity and stress. The asymptotic results of numerical simulations agree with the analytical solution. The analysis of radial convergence of a borehole show that an initially not radially symmetric stress field leads to a radially symmetric field of stress if the far-field and the shape of the hole is kept radially symmetric. Stress and velocity fields of real problems with corresponding conditions can be estimated objectively with the aid of such results.

Borehole convergence tests, which have been carried out with novel testing devices, reveal the influence of deviatoric stress on the evolution of deformation of a vertical hole. The employed numerical model has been validated with simulations of the laboratory test. The influence of the hole bottom has been investigated with an axisymmetric model. The convergence of a vertical hole by creep increases significantly in its major part if the deviatoric part of the far-field stress exceeds a critical value. This has been confirmed by model tests with a hydrogel. The influence of casings and linings on convergence has been studied with a plane strain model of a horizontal cross section. The results of simulations with plane strain or stress models show that such models are not capable to substitute estimations of gradual caving with axisymmetric models.

A fluid seal (cap rock) above a salt pillow has been modeled with axial symmetry. A potential weak point is the clay smear in a fault, which is sheared anew by injection of fluid below the cap rock. Based on exemplary data, evolutions of deformation rates due to a CO_2 injection have been simulated with representative parameters and simplifying symmetry assumptions. The results show that deformation rates in a clay smear can be kept low with moderate pressure changes due to elastic stressing of the formations above and below. It has been shown that stopping of an injection at a constant reservoir pressure leads to markedly decreasing deformation rates a clay smear. Its properties can be determined with reconstituted samples as shearing in faults means remolding. A reduction of the reservoir pressure can enable a self-healing of the clay smear due to a thermally activated stress redistribution. Thus, the system gets safer within a short time. This can be taken into account for a continued injection. Deformation rates in a viscoplastic formation that seals a CO_2 reservoir can only be estimated with the employed model for subcritical states (ductile range). The ductility of a viscoplastic formation during and after an injection can be judged with the proposed simulations.

7.2 Outlook

The results of this thesis show that numerical simulations with the employed constitutive model can lead to useful estimates of evolutions of state and shape of viscoplastic formations. They can help to plan underground operations with viscoplastic formations in a subcritical state (ductile range).

Locally and temporarily changing sedimentation conditions lead to material properties of sedimentary rocks which are highly variable in space. It is hardly practicable to determine detailed spatial distributions of in-situ material properties within an entire geological structure. Therefore, evolutions of state and shape of viscoplastic formations should be estimated by means of numerical simulations with reasonable ranges of material parameters. The upper and lower bounds of validity ranges should be confirmed with additional laboratory tests.

Inclined boreholes allow to access reservoirs within an extended area from a single drilling site. In general, the orientation of a borehole axis does not correspond to a principal axis of the far-field stress. Inclined boreholes do not exhibit radial symmetry if the far-field stress has another symmetry. The convergence cannot be estimated with a disc which is orthogonal to the borehole axis. As with a vertical borehole critical far-field conditions could be specified for accelerated creep which is accompanied by a dramatically increasing ovalisation of the borehole. The criticality depends strongly on the inclination relative to the far-field principal stresses. Numerical simulations can be carried out with and without supporting. Suitable laboratory tests with a model material could serve to validate the numerical model.

Chapter 8

Zusammenfassung und Ausblick

8.1 Zusammenfassung

Die Abschätzung und Bewertung von zu erwartenden Verformungsraten ist eine Schlüsselaufgabe bei mechanischen Betrachtungen von viskoplastischen Formationen.

Viskose Effekte (Argotropie, Kriechen und Relaxation) wurden zunächst an Paraffin untersucht, da es geeignet ist, das Verhalten von Geomaterialien, welche sich wachsähnlich verhalten, qualitativ zu veranschaulichen. Paraffin weist eine ausgeprägt nichtlineare Viskosität auf, und die beobachteten viskosen Effekte gleichen denen von Geomaterialien wie Eis oder Steinsalz bei langsamen Verformungen. Weiche, vollständig gesättigte Böden zeigen ein ähnliches Verhalten, solange das Porenfluid inkompressibel ist und dessen Filtration ausgeschlossen oder vernachlässigt werden kann. Mit verschiedenen Geomaterialien wurden Laborversuche durchgeführt. Rekonstituierte Proben aus einem Bentonit und einem natürlichen Ton, mit Konsolidationsdrücken von 20 - 150 MPa, zeigen ebenso Ratenabhängigkeit und eine obere Grenze der Verformungsrate durch Scherlokalisierung und Bruchbildung. Diese Eigenschaften wurden auch an natürlichen Tonsteinproben beobachtet. Wegen mangelnder Gleichförmigkeit der Proben vor und während den Experimenten ist die Bestimmung von deren Materialeigenschaften jedoch weniger präzise.

Die Ergebnisse von Laborversuchen mit Geomaterialien zeigen, dass deren viskoplastisches Verhalten bei hinreichend kleinen Verformungsraten ähnlich dem Verhalten von Paraffin im subkritischen Zustand ist. Daher werden Materialien, deren Verhalten im subkritischen Bereich die folgenden idealisierenden Annahmen einschliesst, Keroide (griech.: Wachsähnliche) genannt. Diese Annahmen sind: Isotropie der Materialeigenschaften, lineare Elastizität bei rascher kleiner Verformung, nichtlineare Viskosität mit vernachlässigbarer volumetrischer Viskosität, überwiegend thermische Aktivierung und vernachlässigbare seismische Aktivierung durch Poren, und viskoplastische Duktilität bei genügend niedrigen Verformungsraten. Duktilität und Viskoplastizität treten fast immer gemeinsam auf. Dies gilt für eine gewisse Spanne von Verformungsraten, Drücken und Temperaturen. Die Materialeigenschaften der ausgewählten Proben, welche in Laborversuchen beobachtet wurden, stimmen im Wesentlichen mit den Annahmen überein, die für das Materialverhalten von Keroiden getroffen wurden.

Im duktilen Bereich kann ein geringer Anteil an Mikroporen auftreten, der in der Nähe der Duktilitätsgrenze plötzlich ansteigt. Viskoplastische Verformungen sind bei niedrigen Verformungsraten bis zu einer kritischen Verformungsrate möglich, welche die Grenze des duktilen Bereichs kennzeichnet. Bei dieser Verformungsrate entstehen mehr Mikroporen als in der gleichen Zeitspanne wieder verschwinden. Daher können sich bei einer kritischen Verformungsrate die Mikroporen zu Flachporen und Rissen entwickeln. Bei fortgesetzter Stauchung bei einer kritischen (oder höheren) Stauchungsrate wurden Scherlokalisierung und Rissbidung beobachtet. Die maximale Spannung bei der kritischen Stauchungsrate beschreibt einen kritischen Punkt des Materials am Übergang von viskoplastischem zu klastischem Verhalten. Verformungsraten, die wesentlich höher als die kritische Verformungsrate sind, haben eine axiale Spaltung (axial splitting) der Probe zur Folge, welche mit akustischen Emissionen einhergeht. Ein in-situ Monitoring von seismischen Ereignissen ist daher ratsam, um Gestein in einem subkritischen Zustand zu halten. (Der allgemein verwendete Begriff Versagen ist mit einer subjektiven Erwartung an das Materialverhalten verbunden. Daher ist der Begriff Versagen für eine objektive Beschreibung des Materialverhaltens ungeeignet.)

Fast jede Plastizität ist eine Form von nichtlinearer Viskosität und thermisch aktiviert. Viskose Effekte in Feststoffen können physikalisch mit thermisch aktivierten Veränderungen von bereits existierenden Versetzungen erklärt werden. Daher basieren die hier vorgestellten Zustandsgleichungen auf dieser Art Platzwechseltheorie und liefern eine Beschreibung von argotropem (geschwindigkeitsabhängigem) Verhalten, Kriechen und Relaxation. Die verwendete viskoplastische Materialgleichung für Keroide erfüllt die Kriterien der Objektivität. Beliebige isochore Verformungen können mit deviatorischen Beziehungen zwischen Spannungsraten und Verformungsraten erfasst werden. Einheiteninvarianz wird durch zwei Materialkonstanten erreicht. Invarianz bezüglich eines beliebig gewählten Referenzsystems wird durch eine isotrope Tensorfunktion garantiert. Daher ist eine Rotation des Koordinatensystems ohne Belang, und da nur Verformungsraten (und nicht Dehnungen) für das Materialverhalten eine Rolle spielen, gibt es keinen Einfluss einer beliebig gewählten Anfangszeit. Da keine inneren Variablen verwendet werden, wird angenommen, dass das Gefüge von Keroiden allein von deviatorischen Spannungen bestimmt wird. Dieser Ansatz ist einstweilen auf monotone Entwicklungen beschränkt. Der

Gültigkeitsbereich wird aufgrund von Scherlokalisierung und Rissbildung durch eine Obergrenze der Verformungsrate beschränkt. Numerische Berechnungen der durchgeführten Versuche mit den vorgeschlagenen Zustandsgleichungen zeigen eine akzeptable Übereinstimmung mit den Ergebnissen der Laborversuche innerhalb des Gültigkeitsbereichs.

Eindimensionale Randwertprobleme bei viskoplastischen Formationen wurden hinsichtlich der Entwicklung von Geschwindigkeit und Spannung betrachtet. Eine eindimensionale Analyse eines Kriechhanges zeigt, dass ein beliebiges zulässiges Anfangsspannungs- und Anfangsgeschwindigkeitsfeld asymptotisch zu einem stationären Spannungs- und Geschwindigkeitsfeld führt. Die Ergebnisse von numerischen Simulationen stimmen gut mit der analytischen Lösung des Problems überein. Die Analyse eines radial konvergierenden Bohrloches zeigt, dass ein zunächst nicht radial symmetrisches Spannungsfeld zu einem radial symmetrischen Spannungsfeld führt, wenn die Form des Bohrloches radialsymmetrich gehalten wird. Spannungs- und Geschwindigkeitsfelder von realen Problemen mit entsprechenden Bedingungen können mit den vorgestellten Ergebnissen objektiv abgeschätzt werden.

Bohrloch-Konvergenzversuche, welche in neuartigen Versuchsgeräten durchgeführt wurden, zeigen den Einfluss der deviatorischen Spannung auf die Verformungsentwicklung eines Bohrlochs. Das verwendete numerische Modell wurde mit Hilfe von Simulationen der durchgeführten Laborversuche validiert. Der Einfluss des Bohrlochbodens wurde an einem axialsymmetrischen Modell untersucht. Die Konvergenz eines vertikalen Bohrloches infolge Kriechen steigt entlang dem grössten Teil seiner axialen Ausdehnung signifikant an, wenn der deviatorische Anteil der Fernfeldspannung einen kritischen Wert überschreitet. Dies wurde durch Modellversuche mit einem Hydrogel bestätigt. Der Einfluss von Verrohrungen und Futterrohren auf das Konvergenzverhalten wurde an einem Modell mit ebener Verformung (plane strain) eines horizontalen Querschnitts untersucht. Die Ergebnisse von Simulationen mit ebener Verformung oder Spannung zeigen, dass solche Modelle nicht geeignet sind, um Abschätzungen von Konvergenzverformungen mit axialsymmetrischen Modellen zu ersetzen.

Cap Rocks (Hutgesteinsformationen) oberhalb von Salzkissen wurden axialsymmetrisch modelliert. Ein potentieller Schwachpunkt bei einer abdichtenden Formation ist der sog. Clay Smear in einer Verwerfung, welcher durch Injektion eines Fluids unterhalb dieser dichtenden Formation erneut geschert wird. Auf der Grundlage von Beispieldaten wurden Entwicklungen von Verformungsraten mit repräsentativen Parametern und vereinfachten Symmetrieannahmen simuliert. Die Ergebnisse zeigen, dass Verformungsraten in einem Clay Smear bei mässigen Druckänderungsraten durch elastische Verspannung der liegenden und hangenden Formationen niedrig gehalten werden können. Es wurde gezeigt, dass das Stoppen einer Injektion bei konstantem Reservoirdruck zu deutlich abnehmenden

Verformungsraten in einem Clay Smear führt. Seine Eigenschaften können mit rekonstituierten Proben bestimmt werden, da Scherung in Verwerfungen eine Umformungen bedeutet. Eine Reduktion des Reservoirdrucks kann eine Selbstheilung des Clay Smears durch thermisch aktivierte Spannungsumlagerungen ermöglichen. Damit wird das System innerhalb kurzer Zeit sicherer. Das kann bei der Fortsetzung einer Injektion berücksichtigt werden. Verformungsraten in einer viskoplastischen Formation, die einen CO_2-Speicher abdichtet, können mit dem verwendeten Modell für den subkritischen Bereich abgeschätzt werden. Die Duktilität einer viskoplastischen Formation während und nach einer Injektion kann mit den vorgeschlagenen Simulationen bewertet werden.

8.2 Ausblick

Die Ergebnisse der vorliegenden Arbeit zeigen, dass numerische Simulationen mit den verwendeten Modellen und Zustandsgleichungen zu praktisch anwendbaren Ansätzen für die Bewertung von Entwicklungen von Zustand und Form von viskoplastischen Formationen führen. Sie ermöglichen die Planung von untertägigen Massnahmem in viskoplastischen Formationen im subkritischen (duktilen) Bereich.

Lokal und zeitlich wechselnde Sedimentationsbedingungen führen zu räumlich stark variierenden Materialeigenschaften von Sedimentgesteinen. Es ist kaum möglich, für eine gesamte geologische Struktur eine detaillierte räumliche Verteilung der in-situ Materialeigenschaften zu bestimmen. Daher sollten Entwicklungen von Zustand und Form von viskoplastischen Formationen mit Hilfe von numerischen Simulationen mit einer sinnvollen Bandbreite möglicher Materialparameter abgeschätzt werden. Abschätzungen von sinnvollen Bandbreiten setzten eine geeignete Datenbasis repräsentativer viskoplastischer Parameter voraus. Die untere und obere Grenze der Bandbreite sollte durch zusätzliche Laborversuche bestätigt werden.

Geneigte Bohrungen ermöglichen die Erschliessung von Lagerstätten über ein grösseres Gebiet von einem einzigen Bohrplatz aus. Im Allgemeinen stimmt die Orientierung der Bohrlochachse nicht mit einer der Hauptachsen der Fernfeldspannung überein. Geneigte Bohrungen weisen keine radiale Symmetrie auf, wenn die Fernfeldspannung eine andere Symmetrie hat. Die Konvergenz kann nicht mit einer orthogonal zur Bohrlochachse orientierten Scheibe abgeschätzt werden. Wie bei einer vertikalen Bohrung könnten kritische Fernfeldbedingungen für eine Beschleunigung des Kriechens spezifiziert werden, welches mit einer dramatisch ansteigenden Ovalisierung des Bohrloches einher geht. Die Kritikalität hängt stark von der Neigung der Bohrlochachse relativ zum Fernspannungsfeld ab. Numerische Simulationen können mit oder ohne Stützung durch eine Verrohrung durchgeführt werden. Geeignete Laborversuche mit einem Modellmaterial könnten der Validierung numerischer Modelle dienen.

Bibliography

[1] Prandtl, L.: Ein Gedankenmodell zur kinetischen Theorie der festen Körper. In: *Zeitschrift für angewandte Mathematik und Mechanik*, 8 (1928), Nr. 2, S. 85-106.

[2] Norton, F.H.: *The creep of steel at high temperatures.* 1st ed.. London: McGraw-Hill Publishing, 1929.

[3] Leinenkugel, H.-J.: *Deformations- und Festgkeitsverhalten bindiger Erdstoffe. Experimentelle Ergebnisse und ihre physikalische Deutung.* Veröffentlichungen des Institutes für Bodenmechanik und Felsmechanik, Universität Karlsruhe, Heft 66. Karlsruhe: 1976.

[4] Gudehus, G.; Leinenkugel, H.-J.: Fließdruck und Fließbewegung in bindigen Böden: Neue Methoden. In: *Vorträge der Baugrundtagung 1978 in Berlin.* Berlin: 1978.

[5] Glasstone, S.; Laidler, K.; Eyring, H.: *The theory of rate processes.* New York: McGraw-Hill Book Company, 1941.

[6] Eisenmann, J.: *Zeitliches Konvergenzverhalten von Bohrungen in Gesteinen mit viskosen Eigenschaften.* Diploma thesis, Institut für Bodenmechanik und Felsmechanik, Universität Karlsruhe, prepared and supervised by S. Ruebel. Karlsruhe: 2007.

[7] Mitchell, J.; Campanella, R.; Singh, A.: Soil creep as a rate process. In: *Proc. of the ASCE, Soil mechanics and foundation division*, Vol. 94 (1968), No. SM1, S. 231-253.

[8] Persson, B. N. J.: Theory of time-dependent plastic deformation in disordered solids. In: *Physical Review B, The American Physical Society*, Vol. 61 (2000), No. 9, S. 5949-5966.

[9] Persson, B. N. J.: Model study of brittle fracture of polymers. In: *Physical Review Letters, The American Physical Society*, Vol. 81 (1998), No. 16, S. 3439-3442.

[10] Arrhenius, S.: Über die Reaktionsgeschwindigkeit bei der Inversion von Rohrzucker durch Säuren. In: *Zeitschrift für physikalische Chemie*, Band. 4 (1889), Heft 2, S. 226-248.

[11] Lurje, A. I.: *Räumliche Probleme der Elastizitätstheorie.* Berlin: Akademie-Verlag, 1963.

[12] Mandl, G.: *Mechanics of tectonic faulting.* Amsterdam: Elsevier Science Publishers, 1988.

[13] Gudehus, G.: *Physical Soil Mechanics.* Berlin: Springer Verlag, 2011.

[14] Press, F.; Siever, R.: *Allgemeine Geologie.* 1. Auflage. Heidelberg: Spektrum Akad. Verlag, 1995.

[15] Okrusch, M.; Matthes, S.: *Mineralogie. Eine Einführung in die spezielle Mineralogie, Petrologie und Lagerstättenkunde.* 8. Aufl.. Berlin: Springer Verlag, 2009.

[16] Bollrich, G.; Preissler, G.: *Technische Hydromechanik. Band 1, Grundlagen.* 3. Aufl.. Berlin: Verlag für Bauwesen, 1992.

[17] Odqvist, F.; Hult, J.: *Kriechfestigkeit metallischer Werkstoffe.* 1. Aufl.. Berlin: Springer Verlag, 1962.

[18] Aadnoy, B. S.: Introduction to special issue on borehole stability. In: *Journal of Petroleum Science & Engineering*, Vol. 38 (2003), p. 79-82.

[19] Kudella, P.: *Mechanismen der Bodenverdrängung beim Einpressen von Fluiden zur Baugrundverfestigung.* Veröffentlichungen des Institutes für Bodenmechanik und Felsmechanik, Universität Karlsruhe, Heft 132. Karlsruhe: 1994.

[20] Lenz, J.: *Skriptum zur Vorlesung Kontinuumsmechanik I und II.* Institut für Theoretische Mechanik, Universität Karlsruhe, 4. Aufl.. Karlsruhe: 1995.

[21] Simulia: *ABAQUS Analysis Users' Manual.* v6.10.

[22] Simulia: *ABAQUS Theory Manual.* v6.10.

[23] Simulia: *ABAQUS Keywords Reference Manual.* v6.10.

[24] Balthasar, K., Borm, G., Gudehus, G., Kretzschmar, H.-J., Legarth, B. Mutschler, T., Nüesch, R., Rübel, S., Schmitt-Hattenberger, C., Schütt, H. und Spangenberg, E.: CO2-Storage, Monitoring and Safety Technology. In: *Geotechnologien Science Report: Investigation Utilization and Protection*

of the Underground, No. 6 (2005), Potsdam, Koordinierungsbüro Geotechnoligien, 2005.

[25] Balthasar, K., Gudehus, G., Hauser-Fuhlberg, M., Mutschler, T., Rübel, S., Triantafyllidis, T. und Weidler, P.: Joint Project COSMOS, CO2 Storage, Monitoring and Safety Technology, SP 3 Cap Rock Integrity. In: *Geotechnologien Science Report: 1. French-German Symposium on Geological Storage of CO2*, No. 9 (2007), Potsdam, Koordinierungsbüro Geotechnoligien, 2005.

[26] Rübel, S. et al.: *Cap Rock Integrity during and after CO2 injection.* Report at Geotechnologien Status Seminar, Hamburg, 15.-16.11.2007.

[27] Metz, B.; O. Davidson; H. C. de Coninck; M. Loos; L. A. Meyer (eds.): *IPCC Special Report on Carbon Dioxide Capture and Storage. Prepared by Working Group III of the Intergovernmental Panel on Climate Change.* Cambridge, UK: Cambridge University Press, 2005.

[28] Zemke, K. et al. : Petrophysical analysis to investigate the effects of carbon dioxide storage in a subsurface saline aquifer at Ketzin. In: *International Journal of Greenhouse Gas Control*, 4 (1998), 990-999, Elsevier, 2010.

[29] Förster, A. et al. : Baseline characterization of the CO2SINK geological site at Ketzin, Germany. In: *Evoromental Geosciences*, No.3 (September 2006), pp. 145-161.

[30] Förster, A. et al. : The Geology of the CO2SINK Site: From Regional Scale to Laboratory Scale. In: *Energy Procedia*, Elsevier, 2009, Available online at www.sciencedirect.com.

[31] Lempp, C. : private communication.

[32] Fecker, E.; Reik, G.: *Baugeologie.* 1. Aufl.. Stuttgart: Enke Verlag, 1987.

[33] Pimentel, E.: *Quellverhalten von diagenetisch verfestigtem Tonstein.* Veröffentlichungen des Institutes für Bodenmechanik und Felsmechanik, Universität Karlsruhe, Heft 139. Karlsruhe: 1996.

[34] Nüesch, R.: *Das mechanische Verhalten von Opalinuston.* Mitteilungen aus dem Geologischen Institut der Eidgenössischen Technischen Hochschule (ETH) und der Universität Zürich, Neue Folge Nr. 293. Zürich: 1991.

[35] BÜHLER, M. ET AL. : Investigation of the stability of deep wellbores in sedimentary rocks including time and temperature effects. In: *Proceedings of the 9th International Congress on Rock Mechanics*, Vol. 1, 431-434, International Society for Rock Mechanics (ISRM), Paris: 1999.

[36] DGGT: *Empfehlungen des Arbeitsauschusses Ufereinfassungen - EAU.* 8. Aufl. 1990, Verlag Ernst u. Sohn, Berlin.

[37] VAN DEN HAM, G., CZURDA, K.: *Numerical modeling of a slowly deforming slope in the Vorarlbergian Alps, Austria.* Proceedings of the 27th Assembly of the European Geophysical Society, Nice, 21-26 April, 2002, Abstracts, Volume 4.